# Modelling and computational analysis of heat-transfer in multi-geometry and multi-phase flow of Newtonian and non-Newtonian fluids in pipes and channels


BY

Anele Mavi

A thesis submitted for the degree of

***Doctor of Philosophy***

in the Department of Mathematics and Applied Mathematics,
Faculty of Science, University of Cape Town
July 2022

Supervisor: Dr. Tiri CHINYOKA
Department of Mathematics and Applied Mathematics, and
Center for Research in Computational and Applied Mechanics,
University of Cape Town.

**Declaration**

I, the undersigned, Anele Mavi, hereby declare that the work contained in this thesis titled "Modelling and computational analysis of heat-transfer in multi-geometry and multi-phase flow of Newtonian and non-Newtonian fluids in pipes and channels", is my original work, and that any work done by others or by myself previously has been acknowledged and referenced accordingly and that it has not been and will not be used to pursue or attain any other academic degree of any level at any other academic institution, be it foreign or South African.

Signature:

Date : 21 July 2022

I confirm that I have been granted permission by the University of Cape Town's Doctoral Degrees Board to include the following publication(s) in my PhD thesis, and where co-authorships are involved, my co-authors have agreed that I may include the publication(s):

1. A. Mavi, T. Chinyoka, Finite volume computational analysis of the heat transfer characteristic in a double-cylinder counter-flow heat exchanger with viscoelastic fluids, Defects and Diffusion Forum, 2022, In Press.

2. A. Mavi, T. Chinyoka, A. Gill, Modelling and Analysis of Viscoelastic and Nanofluid Effects on the Heat Transfer Characteristics in a Double-Pipe Counter-Flow Heat Exchanger, Applied Sciences, 12(11), 2022, 5475.

3. A. Mavi, T. Chinyoka, Volume-of-fluid based finite-volume computational simulations of three-phase nanoparticle-liquid-gas boiling flow problems in vertical rectangular channels, Energies, 15(15), 2022, 5746.

SIGNATURE: DATE : 16 August 2022
STUDENT NAME: Anele Mavi

# Dedication

Dedicated to my amazing family.

# Acknowledgements

I give you all the Glory and Honour my heavenly father this PhD would not have been possible without you.

I would like to express my deepest gratitude to my supervisor Dr Tiri Chinyoka for the dedicated support and assistance throughout the course of this work. You have been the best supervisor, thank you so much. I would also like to express my sincere gratitude to the Center for High Performance Computing (CHPC) and specifically to Dr Andrew Gill for the support and assistance with the OpenFOAM software. My sincere gratitude also goes to Professor Daya Reddy for providing financial assistance through the South African Chair in Computational Mechanics.

Finally, to my parents and family, thank you very much for your boundless support, encouragement and prayers. May God bless you abundantly.

# Contents

# Abstract

The thesis develops and computationally analyzes mathematical models for multi-geometry heat-exchanger design and for multi-phase flow problems involving boiling and bubble formation. Newtonian fluids, Newtonian-Fluid-Based- Nanofluids, and non-Newtonian fluids are all considered in the thesis. The Newtonian-Fluid-Based-Nanofluids (NFBN) are designed from the homogeneous mixing of a Newtonian base-fluid with solid nano-particles. Water will be used as the Newtonian base-liquid and two types of nano-particles will be considered, aluminium oxide ($Al_2O_3$) and titanium oxide ($TiO_2$) nano-particles. The non-Newtonian fluids in this thesis are modelled via the Giesekus viscoelastic constitutive equations.

For the multi-geometry heat-exchanger problems, the thesis will focus attention on counterflow heat-exchangers in cylindrical geometries, specifically counterflow, double-cylinder heat-exchangers. The problem statement in this direction focuses on the non-isothermal dynamics and heat-transfer characteristics for a counterflow, double-cylinder heat-exchanger design with a viscoelastic fluid flowing in the core (inner) cylinder and a Newtonian fluid flowing (in the opposite direction) in the shell (outer annulus) region. Investigations are extended to investigate the effects of using Newtonian-Fluid-Based-Nanofluids (NFBN) instead of ordinary newtonian fluids in the outer annulus. The Giesekus viscoelastic constitutive model is used to model and describe the rheological behaviour of the viscoelastic core-fluid. The numerical algorithms for these problems are based on the Finite Volume Methods (FVM) implemented on the OpenFOAM software. The numerical instabilities due to the High Weissenburg Number Problem (HWNP) are resolved by employing either the Discrete Elastic Viscous Stress Splitting (DEVSS) or the Log Conformation Reformulation (LCR) techniques. The pressure-velocity coupling is resolved via the Pressure Implicit with Splitting of Operator (PISO) approach. The results illustrate

that the use of NFBN as the coolant fluid leads to enhanced cooling of the hot core-fluid as compared to using an ordinary (nano-particle free) Newtonian coolant. Specifically, the results illustrate that an increase in the nano-particle volume-fraction, in the coolant shell fluid, leads to enhanced heat-exchange characteristics from the hot core-fluid to the coolant shell-fluid.

The multi-phase flow investigations focus on the simulation of three-phase (solid-liquid-gas) boiling flow and bubble formation problems in rectangular channels. The numerical algorithms are also based on the Finite Volume Methods (FVM) implemented on the OpenFOAM software. The numerical algorithms additionally implement both the volume-of-fluid (VOF) methods for liquid-gas interface tracking as well as the volume-fraction methods to account for the concentration of embedded solid nano-particles in the liquid phase. Water is used as the base-liquid and the solid phase is modelled via metallic nano-particles, both aluminium oxide ($Al_2O_3$) and titanium oxide ($TiO_2$) nano-particles are considered. The (aluminium oxide or titanium oxide) nano-particles are homogeneously mixed within the water base-liquid. The gas phase is considered as a vapour arising from the boiling processes of the liquid-phase. In addition to the FVM and VOF numerical methodologies for the discretization of the governing equations, the pressure-velocity coupling is resolved via the PIMPLE algorithm, a combination of the Pressure Implicit with Splitting of Operator (PISO) and the Semi-Implicit Method for Pressure-Linked Equations (SIMPLE) algorithms. The simulations and results accurately capture the formation of vapour bubbles in the two-phase (particle-free) liquid-gas flow and additionally the computational algorithms are similarly demonstrated to accurately illustrate and capture simulated boiling processes. The presence of the nano-particles is again demonstrated to enhance the heat-transfer, boiling, and bubble formation processes.

## Keywords:

Viscoelastic fluid, Giesekus Model, Finite Volume Methods, OpenFOAM, Heat exchanger, Multi-geometry flow, Multi-phase flow, nanofluids.

# List of Tables

# List of Figures

# Chapter 1

# Introduction

## 1.1 Summary

Studies into multi-domain heat-exchange processes and/or into solid-liquid-gas phase change processes are of significant contemporary industrial importance and hence have been a focus of many research investigations. Examples of industrial applications include air-conditioning, refrigeration, power generation, pharmaceutical product development, food processing, and polymer processing, etc.

The incorporation of viscoelastic fluids in heat-exchange and/or phase-change investigations is fundamental in capturing the complex rheology and intrinsic characteristics of the underlying fluids, specifically with due regard to contemporary applications. The incorporation of viscoelastic fluids in heat-exchange and/or phase-change investigations has however received scant attention in the existing literature. The main reason behind the lack of inclusion of viscoelastic fluids in phase-change investigations can be attributed to the fact that such processes involve heat-transfer while the non-isothermal viscoelastic fluid models have only been recently developed.

The complex rheology and dynamics of viscoelastic fluids makes them challenging to study theoretically while experimental investigations are usually costly. In general theoretical investigations of non-isothermal fluid flow (with either Newtonian or non-Newtonian fluids) are quite challenging. The mathematical model equations governing fluid flow, even in non-complex geometries, consists of coupled systems of nonlinear Partial Differential Equations (PDEs) which are intractable to analytical treatment. Such investigations have therefore increasingly focused on numerical and computational solution techniques. The field of Computational Fluid Dynamics (CFD) has unsurprisingly, therefore, become probably one of the fastest growing areas of scientific computing. Modern CFD techniques can provide an in-depth understanding of the behaviour of Newtonian and non-Newtonian fluids under various and indeed complex physical and geometric conditions.

The investigations in this thesis will focus on computational analysis of the non-isothermal dynamics of Newtonian and viscoelastic fluids (and nanofluids) in single or multiply-connected geometries. The main underlying applications of the investigations are to heat-exchanger dynamics and to boiling and bubble formation processes. The numerical algorithms deployed in this thesis are derived from the Finite Volume Methods (FVM). The computational solutions are obtained by implementing the FVM algorithms on the OpenFOAM software platform.

## 1.2 Viscoelastic fluids

Viscoelastic fluids are a class of non-Newtonian fluids which exhibit a combination of viscous and elastic behaviour. Viscoelastic fluids are also known as polymeric fluids due to the fact that they comprise of long-chain polymer molecules. For a detailed survey of the rheology of viscoelastic fluids, we refer the reader to, say, [1, 2, 3]. The

computational solution processes for viscoelastic fluid flows are prone to numerical instabilities at high Weissenberg (We) or Deborah (De) numbers - leading to the so-called High Weissenberg Number Problem (HWNP). The dimensionless parameters (We and De) represent the ratio between the characteristic relaxation time of the fluid and a characteristic time of the flow process. At a high We or De number the elastic effects are more pronounced, leading to the dominance of solid like (elastic) behaviour and hence also giving rise to the HWNP for the primarily fluid dynamics focused CFD techniques, [4, 5].

The work in [6], investigated the non-isothermal viscoelastic fluid flow in 4:1 axi-symmetric contractions. The viscoelastic fluid was modeled by the Oldroyd-B constitutive equation. The temperature dependence of viscosity and relaxation time were modeled via the Williams-Landel-Ferry (WLF) empirical relation. To mitigate against numerical instabilities at high Deborah numbers, the Discrete Elastic Viscous Stress Splitting (DEVSS) technique was employed. In the investigations of [7, 8], the non-isothermal behavior of an Oldroyd-B fluid was also investigated. Instead of the WLF model, they employed an Arrhenius approach to describe the temperature dependence of viscosity and relaxation time. The Log Conformation Reformulation (LCR) technique was utilized to address the numerical instabilities arising out of the HWNP. In the works of [9, 10, 11] the non-isothermal viscoelastic effects are not only implemented on the viscosities and relaxation times, but additionally incorporated into the viscoelastic stress constitutive models. These investigations used appropriate energy equations, see for example [9, 12], that were developed to thermodynamically account for polymeric effects.

Heating and cooling applications are commonplace in many industrial processes. The effects of non-Newtonian fluids in heating and cooling applications has subsequently also found a lot of traction among many researchers. For example, [9, 10] explore the

conductive-convective heat transfer between viscoelastic and Newtonian fluids in heat-exchanger processes. The significant roles played by the viscoelastic fluids are explored with a view to specific applications. The work in [13] investigated a forced convection heat transfer of a viscoelastic fluid in pipes and channels under fully developed thermal and hydrodynamic flow conditions. The effect of Weissenberg number, Brinkman number, Nusselt number, and the Giesekus mobility parameter on the temperature were investigated. In [14], the convective heat transfer of a viscoelastic fluid flowing in a straight pipe or in a space between two parallel plates was investigated. The Elastic Viscous Stress Splitting (EVSS) technique was used to resolve the numerical instabilities arising from the HWNP. The work in [15] modelled conjugate heat transfer of a simplified Phan–Thien–Tanner (PTT) viscoelastic fluid flowing past an unbounded sphere under assumptions of constant viscosity and relaxation time.

## 1.3 Nanofluids

Heat Transfer Fluids (HTF) are of significant importance in industrial applications such as in food production and electronics cooling. The development of efficient HTF, specifically nanofluids, has captured the attention of many researchers leading to a huge volume of numerous experimental, theoretical, and computational investigations. Nanofluids are fluids containing solid, nanometer-sized particles – so called nano-particles, and can provide impressive improvements in the thermal conductivity and heat transfer properties of the corresponding base fluids. The term nanofluids was first coined by [16] to describe the new class of HTF that display thermal properties superior to those of their corresponding base fluids or of conventional particle fluid suspensions.

In work [17], the behaviour and heat transfer enhancement of $Al_2O_3$/water nanofluid flowing inside a closed system designed for cooling of microprocessors was investigated. It was observed that the addition of nano-particles enhanced the convective heat transfer coefficient of the nanofluid with 6.8% particle volume concentration to as much as 40% as compared to that of base fluid. The work in [18], examined the enhancement of thermal conductivity of ethylene glycol in the presence copper oxide ($CuO$). The nano-particle volume fractions dispersed in the base fluid were below 5% and as expected, the nanofluids with low concentrations of $CuO$ nano-particles produced higher thermal conductivities than that of the corresponding base fluids. A further investigation was conducted by increasing particle volume fractions to exactly 5% and thermal conductivity enhancement of up to 22% was observed. The investigations in [19] reported an increase in thermal conductivity of up to 30% when using different nanofluids, i.e., $Al_2O_3$/water, $SiO_2$/water and $TiO_2$/water. The work in [20], studied the heat transfer enhancement of nanofluids composed of $\gamma - Fe_2O_3$ and a mixture of deionized water and ethylene glycol as a base fluid. Results obtained illustrated higher thermal conductivity for the nanofluids than that of the corresponding base fluids with thermal conductivity enhancement increasing with increasing nano-particle volume fraction.

The numerical investigations of [21] simulated a laminar forced convection flow of copper-water nanofluids inside isothermally heated micro-channels. An Eulerian two-fluid nanofluid model was used and the governing equations for both phases were solved using Finite Volume Methods (FVM). The set of discretized equations were solved by employing the line by line method and the velocity-pressure coupling was resolved by the SIMPLE algorithm. In research work [22], a developing laminar forced convection flow of an $Al_2O_3$/water nanofluid in a circular tube subject to constant and uniform heat flux at the wall was studied. Both single-phase and two-phase models were employed with either constant or temperature dependent properties.

The governing equations were solved using the control volume approach. The work in [23], numerically investigated nanofluid flow and heat transfer characteristics between horizontal parallel plates in a rotating system. The viscosity and effective thermal conductivity of the nanofluid were evaluated using the Koo-Kleinstreuer-Li (KKL) correlation. The governing Partial Differential Equations (PDEs) were numerically solved using fourth-order Runge-Kutta methods. In the numerical modelling of nanofluid suspensions in a geothermal heat exchanger, [24] employed FVM for the discretization of the governing equations and implemented the PIMPLE algorithm to dealing with the incompressibility condition. To ensure numerical accuracy and stability, the value of the time step was chosen such that the maximum Courant number was always less than 0.1. In [25], the effect of non-uniform heating on the heat transfer characteristics for the fluid flow of $Al_2O_3$/water nanofluids through a duct having a finite wall thickness subject to sinusoidal heat flux was simulated. The nanofluid was modelled as a single-phase via an Eulerian-Lagrangian method. The SIMPLE algorithm was used to resolve the pressure-velocity coupling. The convective terms and diffusive terms were discretized using the upwind scheme and second order difference scheme respectively.

## 1.4 Heat exchangers

A heat exchanger is a device that facilitates the heat exchange between two fluids which are at different temperatures and which are separated by a solid wall, see for example [9, 10]. Various types of heat exchangers have been developed for industrial applications such as in refrigeration, food processing, heating and air conditioning systems, power generation, and chemical processes. In power generation; evaporators, super-heaters, condensers, and cooling towers are examples of heat exchangers used in industrial power plants.

An overview on the different types of heat exchangers in common use is given in Figure 1.1.

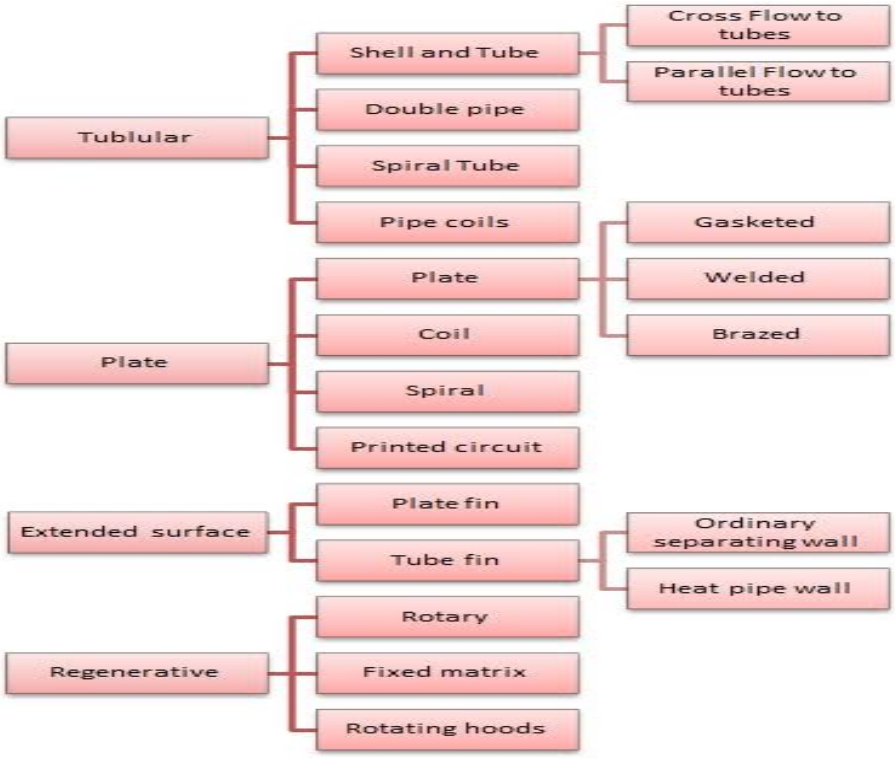


**Figure 1.1:** Classification of Heat Exchangers, [194]

In [26], the heat transfer and pressure drop properties using 2D and 3D models of louvered fin-and-flat tube heat exchangers were simulated. It was observed that at high Reynolds numbers there was an increase in heat transfer rates where thermal boundary layers developed. In [27], simulations of stirred yoghurt processing in a plate heat exchanger were performed. The shear-rate dependence of viscosity was modelled according to the Herschel–Bulkley constitutive model and the Arrhenius model was employed for the temperature dependence of the viscosity. To describe the heat transfer between the heated yoghurt and the coolant (water) two boundary conditions were applied, i.e., variable and constant heat flux. The work in [28] numerically modelled pressure loss in tubes of a heat-exchanger used in closed-wet cooling towers.

Pressure drop was found to depend on the tube arrangement and on the water-to-air ratio. Furthermore, pressure loss was seen to rise by 17% with the interference of upstream air.

The work in [29] analysed the thermal behaviour of fluid media in a helical pipe followed by a shell and tube heat exchanger with helically coiled tubes. Thermal properties were presented in form of Deborah (De) and Nusselt (Nu) numbers. Results obtained showed an increase in overall heat transfer coefficients for increasing De and temperature dependent properties were in agreement with experimental results. In investigations in [9, 10] modelled and numerically solved the conductive-convective heat transfer between a heated core fluid (either viscoelastic or Newtonian) and a coolant Newtonian shell fluid in double-pipe and cross-flow heat exchangers respectively. Simulations results showed that a core viscoelastic fluid attained lower temperature as compared to a core Newtonian fluid. The present investigation extends this work from channel flow to pipe flow and to also include nanofluids.

Utilizing double pipe and shell and tube heat exchangers, [30] numerically and experimentally investigated the heat transfer of $Al_2O_3$/Water nanofluids. The effects of parameters such as hot and cold volume flow rates, nano-particle concentration, and nanofluid temperature on heat transfer characteristics were analysed. Results showed that heat transfer in both heat exchangers increased with increasing hot and cold volume flow rates, nano-particle concentration, and nanofluid inlet temperature. The work in [31], investigated heat transfer enhancement using a non-Newtonian nanofluids in a shell and helical coil heat exchanger. Nanofluids and water (Newtonian) were used on the shell side and tube side respectively. Results illustrated that the Nusselt number increased with an increase in nanofluid concentration, shell side fluid temperature, stirrer speeds, and Deans number.

## 1.5 Phase change

Phase change is a process in which matter changes from one state (i.e. solid, liquid, gas) to another. These changes occur when adequate energy is supplied to (or lost from) the system. There are six different types of phase change phenomena namely, freezing (liquid to solid), melting (solid to liquid), condensation (gas to liquid), evaporation (liquid to gas), sublimation (solid to gas), and de-sublimation (gas to solid). For a broader overview of phase change literature, we refer the reader, say, to [32, 33, 34, 35, 36, 37, 38, 39, 40]. The current work focuses attention to liquid-vapour phase change due specifically to boiling. Even though we ultimately focus on three-phase (solid-liquid-gas) problems, the solid phase (nano-particles) will not change phase and hence will always remain in the solid phase.

The boiling phenomena is encountered in a wide range of industrial applications such as boilers, power generation, and distillation columns. Its widespread use is due to the fact that in comparison to traditional heat transfer methods, a phase-change process is a highly efficient heat transfer mechanism which can accommodate large heat fluxes with relatively smaller temperature variations. Boiling is defined as a phase-change process in which a heated surface causes an adjacent liquid to develop vapour and vapour bubbles. The transition from liquid phase to gaseous phase occurs when the vapour pressure of the liquid is equal to the atmospheric pressure exerted on the liquid. Boiling can be divided into two classes, namely flow-boiling and pool-boiling. In flow-boiling the fluid motion is influenced by natural and force convection, whereas in pool-boiling fluid motion is induced only by natural-convection. The boiling and phase change investigations in this thesis will be limited to pool-boiling.

There are four types of boiling regimes i.e. natural convection, nucleate boiling, transition boiling (in flow-boiling, this would translate to forced convective boiling), and film boiling. One of the earliest research on the boiling phenomena was conducted

by [32] who developed a boiling curve in which different stages of the boiling process can be obtained, see Figure 1.2 for pool-boiling and Figure 1.3 for flow boiling, [33]. For a comprehensive overview with a detailed description of each boiling regime we refer the reader, say, to [32, 33, 34, 35, 36].

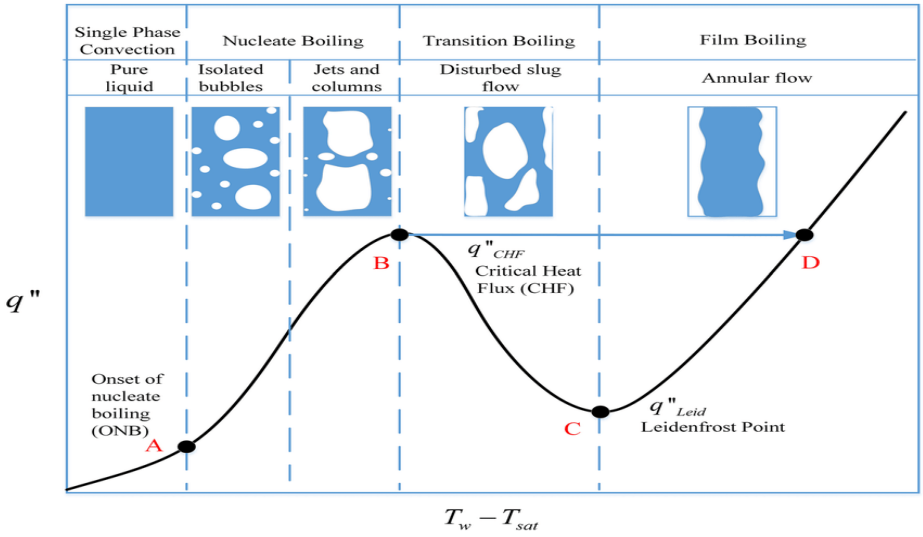


**Figure 1.2:** Pool boiling curve, [33]

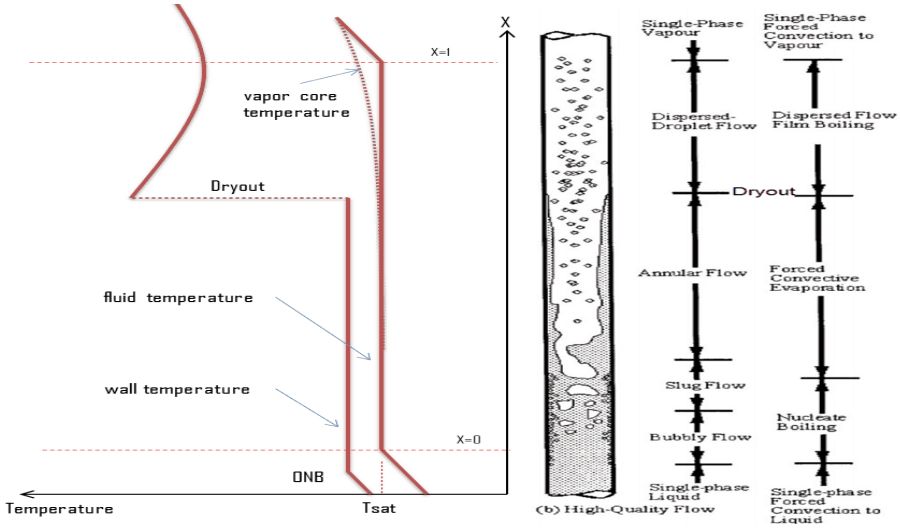


**Figure 1.3:** Flow boiling curve, [33]

Two-phase (liquid-gas) flows are a complicated phenomena which can take on various geometrical arrangements according to the spatial distribution of the liquid and gas

phases in a channel. These geometrical arrangements are known as flow patterns of which there are six distinct flow patterns namely; stratified, wavy, plug, slug, annular (or spray), and bubbly. The most cited flow regime maps reported in literature are by [37, 38, 39] and for a detailed description for each flow pattern we refer to the reader to good treaties of [40, 36]. Flow patterns and a corresponding flow-pattern map are shown in Figure 1.4 [38] and Figure 1.5 [37] respectively.

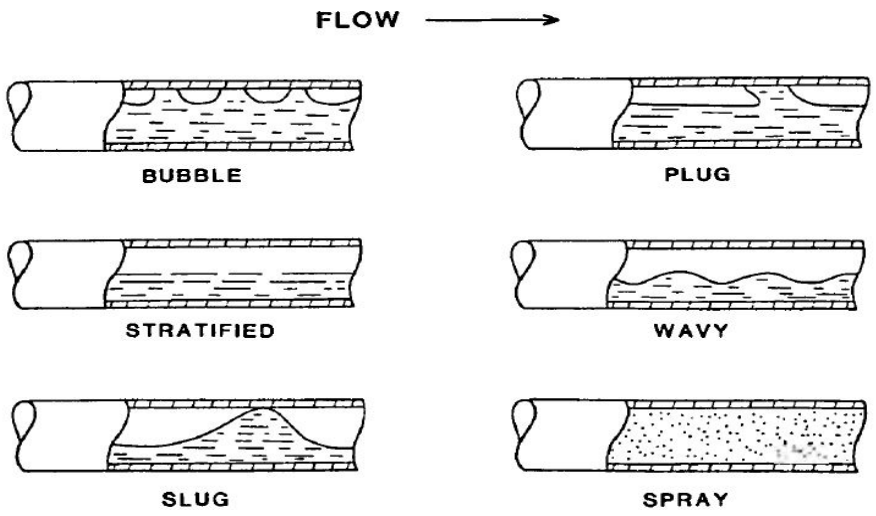


**Figure 1.4:** Two-phase flow patterns, [38]

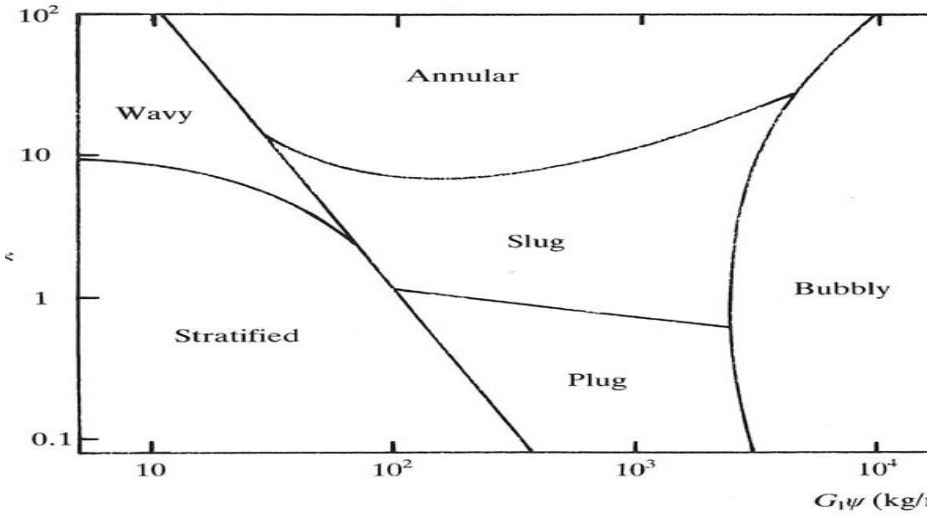


**Figure 1.5:** Flow pattern map, [37]

The use of CFD for the computational analysis of liquid-gas phase change has been conducted, for example in [41] who employed an Eulerian-Eulerian method integrated with phase change models to simulate boiling flows. The simulations were carried out using an axi-symmetric geometry and the Pressure-Implicit-with-Splitting-of-Operators (PISO) algorithm was used to resolve the pressure-velocity coupling. Furthermore, Gauss upwind, Gauss linear, and Gauss limited linear schemes were used for discretization of spatial derivatives. For the turbulence modelling, the k-$\epsilon$ turbulence model was adopted with bubble induced turbulence source terms. The work in [42] used the Eulerian-Eulerian two-phase flow model to simulate boiling heat transfer in pipe flow. The heated wall surface was modelled according to Kurul and Podowski (RPI) model. In [43], boiling flows of refrigerants R-134a and R-22 in a circular duct were simulated to examine flow boiling patterns. The Volume-of-Fluid (VOF) method was utilized for interface capturing and the work also incorporated the geometric reconstruction interpolation scheme. The PISO algorithm was employed to resolve the pressure-velocity coupling. In modelling and numerical analysis of flow boiling, [44] simulated liquid-vapour flow regimes in connection with conjugate heat and mass transfer problem for specimen quenching. The VOF method and PISO algorithm were employed as part of the solution process.

## 1.6 Finite Volume Methods (FVM)

The Finite Volume Methods (FVM)) are used to numerically solve Partial Differential Equations (PDEs). FVM are well suited for all types of PDEs; elliptical, parabolic, and hyperbolic. The discretization procedure involves changing volume integrals into surface integrals using the divergence theorem. These surface integrals are then evaluated as fluxes at each finite volume surface.

FVM can be grouped based on the location where the solution values are stored, [45, 46]; namely cell-centered methods and vertex-centered methods. In vertex-centered methods, the solution values are stored at the vertices of the grid and cells are created around each vertex. In cell-centered methods, the solution is stored at the centre of the cells. In the case of vertex-centered methods, investigations have been conducted using different types of meshes; for example [47, 48, 49] – quadrilateral meshes, [50] – rectangular meshes, and [51, 52, 53] – unstructured meshes. In cell-centered methods, [54, 55] carried out investigations in rectangular meshes and [56, 57] used triangular meshes.

The advantages of FVM are that they enforce conservation of quantities at a discretized level, [58], and they seamlessly adapt to collocated arrangements thus making them well suited for handling fluid flow problems in complex geometries. The FVM gained a significantly important role in numerical simulations as a result of work of [58, 59, 60]. FVM are the most flexible discretization methods used in CFD owing to their ability to carry out discretizations into the physical space without any transformation between the physical and the computational coordinate system. The FVM are therefore probably the most efficient numerical methodologies for CFD problems.

The work in [61] used FVM integrated with the Lattice Boltzmann method to simulate viscoelastic fluid flows. The integrated scheme was validated using the Oldroyd-B model and the linear PPT model with a Poiseuille flow, Taylor-Green vortex flow, and a 4:1 abrupt contraction flow. In [62], viscoelastic fluid flow past a cylinder using FVM in a non-orthogonal block-structured mesh was investigated. The high resolution schemes MINMOD and SMART were used to represent convective terms in the viscoelastic constitutive equations represented by either the Oldroyd-B or the Upper Convected Maxwell (UCM) models. In the numerical investigation of the

strength and pattern of secondary flows of viscoelastic fluid in a straight pipe, [63] used the implicit FVM together with the SIMPLE algorithms. In [64], FVM with a staggered grid were used in the numerical modelling of viscoelastic liquid flow. A third order difference scheme was employed for the discretization of constitutive equations. In simulating an unsteady three dimensional viscoelastic fluid flow through a porous medium, [65] in agreement with [64], used FVM with a staggered grid.

In simulations of heat transfer using FVM, [15] numerically addressed the conjugate heat transfer of a simplified PTT fluid flowing past an unbounded sphere. In the computational analysis of the extrusion process in extrusion based additive manufacturing, [66] developed a numerical model that incorporates a temperature dependent non-Newtonian viscosity. In the case of phase-change problems, [67] numerically investigated the thermal and fluid dynamic behaviour of two-phase flow in double pipe evaporators and condensers. In the simulation of gas-liquid boiling flows, [41] also implemented FVM successfully. In the computational analysis of nanofluid based flows, [68] investigated a natural convective heat transfer of water/$Al_2O_3$ nanofluid in an inclined square geometry. FVM based on the SIMPLE algorithm were used in solving the governing equations. When simulating natural convection heat transfer of a copper-water nanofluids in a vertical cylindrical annulus with heat sources, [69] employed FVM with SIMPLER algorithms.

The FVM are well-established numerical techniques in CFD research. Consequently, FVM are built into many current commercial CFD software such as CFX/ANSYS, FLUENT, PHOENICS, STAR-CD, and OpenFOAM. In this present work the FVM are implemented on the OpenFOAM software.

## 1.7 OpenFOAM

OpenFOAM (Open Source Field Operation and Manipulation) is an open-source CFD software package that implements the Finite Volume Methods as the underlying numerical methodology, [70]. OpenFOAM is a freely distributable software package written in C++ programming language, [71] and has a CFD toolbox for over sixty customized numerical solvers that can perform simulations of fundamental CFD, combustion, heat transfer, turbulence modeling, electromagnetics, multiphase flow, stress analysis, and even financial mathematics models. OpenFOAM is easily extensible by design, making it convenient for users to incorporate their own models since existing solvers can be modified.

In [72], an open-source toolbox, *RheoTool*, based on OpenFOAM was developed for the simulation of viscoelastic fluid flows and Generalized Newtonian Fluids (GNF). The work in [15] uses RheoTool to simulate conjugate heat transfer of a simplified Phan-Thien-Tanner (PTT) fluid flowing past an unbounded sphere. The work in [73] developed and integrated a *viscoelasticFluidFoam* solver into OpenFOAM to address the numerical analysis of viscoelastic fluids. Vigorous testing was conducted using different viscoelastic constitutive models; namely, Oldroyd-B, UCM, Giesekus, PTT, Finite Extensible Nonlinear Elastic (FENE-P), and Pom-Pom. Stable and efficient results were achieved. Investigations in [8] employed the *viscoelasticFluidFoam* solver to simulate the non-isothermal behaviour of an Oldroyd-B fluid in a 4:1 axi-symmetric contractions. [4] also utilized *viscoelasticFluidFoam* solver in the numerical analysis of complex fluids governed by Rolie-Poly viscoelastic constitutive equations. In research work [74], a simulation of viscoelastic fluid flow in a three dimensional lid-driven cavity was conducted by employing the Log-Conformation Reformulation (LCR) stabilization method in OpenFOAM. In the simulation of free surface viscoelastic fluid flow, [75] modified the OpenFOAM solver *viscoelasticFluidFoam* by incorporating the

Volume-Of-Fluid methodology. In addition to the already cited work, we refer the reader to [5, 8, 6, 76] for more examples of viscoelastic fluid dynamics problems implemented in OpenFOAM.

The OpenFOAM software is also well suited to handling nanofluid based flows which are considered in this study. For example, [77] conducted a CFD analysis of a laminar forced convective heat transfer of $Al_2O_3$/water nanofluid in a converging micro channel heat sink with an imposed pressure difference. In [78], the thermal and entropy generation in L-shaped porous cavity filled with nanofluids which obey Buogiorno's two-phase model was investigated. The governing equations were discretized using FVM via OpenFOAM and a C++ code was added to an OpenFOAM solver so as to be able to simulate the Buogiorno's two-phase model and entropy. In [79], a three dimensional analysis of forced convection of Newtonian and non-Newtonian nanofluids in a horizontal pipe utilizing single-phase and two-phase flow mathematical models was conducted. When numerically investigating the relationship between nanofluid natural convection and nano-particles sedimentation, [80] developed three new OpenFOAM solvers based on different approaches in both single-phase and multi-phase directions. The work in [81] also successfully used OpenFOAM in examining anisotropic heat transfer of ferro-nanofluids in partially heated rectangular enclosures.

In the case of multi-phase fluid flows, [41] developed an Eulerian-Eulerian approach coupled with a phase change code in OpenFOAM to simulate gas-liquid boiling flows. In the simulation of nucleate boiling, [82] employed the volume-of-fluid solver of OpenFOAM. In [83], an OpenFOAM two-phase solver designed by [84] was further developed and validated for the numerical investigations of sub-cooled nucleate boiling. In [85], a single condensing bubble behavior in a sub-cooled flow

was investigated using a coupled Level Set and volume-of-fluid method model with phase change properties in OpenFOAM.

## 1.8 Objective and organization of the thesis

We are in the process of developing a volume-of-fluid (VOF) method based OpenFOAM solver for boiling and conjugate heat transfer in multi-region geometries, specifically double-pipe heat-exchangers. It is important to mention that the solver development process is laborious, requiring the merging of at least three solvers. The work in this thesis marks the developmental stages of developing and testing the individual solvers. The merging of the solvers into an integrated solver capable of performing the general purpose simulations remains a work in progress. The chapters presented in this thesis, in particular, therefore represent the foundational building blocks. This notwithstanding, the work presented in the 3 main chapters in this thesis demonstrate detailed computational studies on some specific non-isothermal viscoelastic and nanofluid flows of practical interest to the envisaged general purpose solver.

The organization of this thesis is as follows: In Chapter 2 we present the finite volume computational analysis of the heat transfer characteristics in double-pipe heat-exchangers with heated viscoelastic fluids and Newtonian coolants. In Chapter 3, we extend this work by incorporating nanofluids into the coolant fluids. In Chapter 4, three-phase (nanoparticle-liquid-vapour) boiling and bubble formation problems are investigated with phase-change in the liquid-vapour phases due to boiling and condensation and an otherwise non-phase-changing solid (nano-particle) phase. Concluding remarks are collated in Chapter 5.

# Chapter 2

# Finite volume computational analysis of the heat transfer characteristic in a double-cylinder counter-flow heat exchanger with viscoelastic fluids*

## 2.1 Abstract

This work presents a computational analysis of the heat-exchange characteristics in a double-cylinder (also known as a double-pipe) geometrical arrangement. The heat-exchange is from a hotter viscoelastic fluid flowing in the core (inner) cylinder to

*The contents of this chapter are from [86]

a cooler Newtonian fluid flowing in the shell (outer) annulus. For optimal heat-exchange characteristics, the core and shell fluid flow in opposite directions, the so-called counter-flow arrangement. The mathematical modelling of the given problem reduces to a system of nonlinear coupled Partial Differential Equations (PDEs). Specifically, the rheological behaviour of the core fluid is governed by the Giesekus viscoelastic constitutive model. The governing system of coupled nonlinear PDEs is intractable to analytic treatment and hence is solved numerically using Finite Volume Methods (FVM). The FVM numerical methodology is implemented via the open-source software package OpenFOAM. The numerical methods are stabilized, specifically to address numerical instabilities arising from the High Weissenberg Number Problem (HWNP), via a combination of the Discrete Elastic Viscous Stress Splitting (DEVSS) technique and the Log-Conformation Reformulation (LCR) methodology. The DEVSS and LCR stabilization techniques are integrated into the relevant viscoelastic fluid solvers. The novelties of the study center around the simulation and analysis of the optimal heat-exchange characteristics between the heated Giesekus fluid and the coolant Newtonian fluid within a double-pipe counter-flow arrangement. Existing studies in the literature have either focused exclusively on Newtonian fluids and/or on rectangular geometries. The existing OpenFOAM solvers have also largely focused on non-isothermal viscoelastic flows. The relevant OpenFOAM solvers are modified for the present purposes by incorporating the energy equation for viscoelastic fluid flow. The flow characteristics are presented qualitatively (graphically) via the fluid pressure, temperature, velocity, and the polymer-stress components as well as the related normal stress differences. The results illustrate the expected decrease in the core fluid temperature in the longitudinal direction due to the cooling effects of the shell fluid, whose temperature predictably increases in the counter-flow direction.

# Nomenclature

### Notation

| | |
|---|---|
| $()^*$ | Dimensional quantity |
| $()_c$ | Core-fluid quantity |
| $()_{sf}$ | Shell-fluid quantity |
| $()_w$ | Connecting-wall quantity |
| $()_p$ | Polymer contribution |
| $()_{sol}$ | Solvent contribution |

### Variables

| | |
|---|---|
| $\eta$ | Viscosity |
| $\boldsymbol{F}$ | Body forces |
| $\lambda$ | Relaxation time |
| $\rho$ | Density |
| $C$ | Specific heat capacity |
| $K$ | Thermal-conductivity |
| $p$ | Pressure field |
| $\boldsymbol{S}$ | Rate of deformation tensor |
| $\boldsymbol{\sigma}$ | Total stress tensor |
| $t$ | Time |
| $T$ | Temperature field |
| $\boldsymbol{\tau}$ | Polymer stress tensor |
| $\boldsymbol{U} = (u, 0, v)$ | Velocity field |
| $\boldsymbol{x} = (r, \theta, z)$ | Cylindrical coordinates |

**Parameters**

| | |
|---|---|
| $\alpha$ | Giesekus non-linear parameter |
| $\beta$ | Polymer to total-viscosity ratio |
| De | Deborah-number |
| Pr | Prandtl-number |
| Re | Reynolds-number |

**Abbreviations**

| | |
|---|---|
| FVM | Finite Volume Methods |
| HWNP | High Weissenberg Number Problem |
| DEVSS | Discrete Elastic Viscous Stress Splitting |
| LCR | Log-Conformation Reformulation |

## 2.2 Introduction

The understanding of the intricate dynamics (both the fluid-dynamics and thermodynamics) of viscoelastic fluids has fundamental relevance to a vast array of industrial, pharmacological, and biological applications. Indeed, non-isothermal viscoelastic fluid dynamics finds wide application, say, to heating and cooling, power generation, pharmaceutical product development, food processing, and polymer processing etc. [1, 2, 3, 87]

The complex dynamics of viscoelastic fluid flow has also spawned the rapid development of scientific computing techniques and related software, leading to a rapid expansion of the traditional scope of the field of computational fluid dynamics (CFD). The time dependent flow of viscoelastic fluids in complex geometries and

under various conditions such as non-constant temperature, pressure, etc. (i.e. the complex flow-dynamics of complex-fluids) is intractable to analytical treatment. Indeed, the governing equations for complex-fluid (viscoelastic fluid) flow essentially represent the superposition of highly nonlinear PDEs to the Navier-Stokes equations, which themselves (in their full form) are intractable to analytical treatment. It is therefore not difficult or surprising to see why the solution processes for the complex flow-dynamics of complex-fluids must in practice reduce to numerical and computational methodologies.

Viscoelastic fluid flow problems under non-isothermal conditions, as are considered in this work, are governed by a highly nonlinear system of coupled PDEs describing mass, momentum, and energy conservation, in addition to the stress constitutive PDEs describing the rheological and polymeric behaviour of the specific viscoelastic stresses. For a detailed overview of viscoelastic stress constitutive models we refer the reader, say, to [1, 2, 3]. The incorporation of the non-isothermal effects to the polymer-stress constitutive models is now a well developed field, see for example [12, 88, 89, 6, 7, 8, 9, 10, 90, 15].

The investigations in [6, 7] employed the Oldroyd-B viscoelastic constitutive model to simulate the non-isothermal flow behaviour in 4:1 axi-symmetric contractions under various conditions. Both investigations employed the finite volume numerical methodologies. In their analyses, they opted for an Arrhenius approach in the thermodynamical modelling of temperature dependent fluid properties. The issues related to the non-isothermal viscoelastic flows at high Weissenberg numbers are explored in [8] also via Oldroyd-B viscoelastic constitutive models.

The work in [9] numerically investigated, via finite difference methods, the heat exchange between a core viscoelastic fluid and a Newtonian shell fluid in a double-pipe

heat exchanger. Similar investigations, using the finite difference methods, for cross-flow heat exchangers were conducted in [10]. Both of these investigations employed non-isothermal Giesekus viscoelastic constitutive models to describe the rheological behaviour of the polymer stresses. The work in [15] investigated the conjugate heat transfer of a simplified Phan–Thien–Tanner (PTT) fluid [91] flowing past an unbounded sphere. The simulations carried out in their work assumed constant physical properties and the set of governing equations were solved via the finite volume methods in OpenFOAM via the *rheoTool* solver [72].

Viscoelastic fluid flows are prone to numerical instabilities at high Weissenberg (We) or Deborah (De) numbers, leading to the so-called High Weissenberg Number Problem (HWNP). At a high We (or De) numbers the elastic effects are more pronounced and the fluids largely exhibit solid-like behaviour. This solid-like behaviour is thus the primary source of the numerical instabilities which use fluid-based computational algorithms. The Discrete Elastic Viscous Stress Splitting (DEVSS) technique [6, 76, 75] and the Log Conformation Reformulation (LCR) methodology [92, 93] have been developed to address the HWNP. Other methods have also been developed for these purposes, these include a variant of the DEVSS method called the Elastic Viscous Stress Splitting (EVSS) technique [94], special interpolation schemes [95, 96], and techniques coupling momentum and viscoelastic stress constitutive equations [97, 98, 99, 100, 101].

The present investigation is motivated by the counter-flow heat-exchanger investigations in [9, 102, 103, 104]. Given the need to develop (or account) for industrial heat-exchanger designs of complex geometries, say in bubble column reactors, distillation columns, helical heat exchangers, etc. the current investigates also takes motivation from the finite volume computations, which allow for arbitrary shaped geometries. The cylindrical geometry has been explored in many fluid dynamical applications,

see for example [87, 105, 106] and serves as the motivation for the present work. The OpenFOAM software package implements the finite volume numerical methodologies and a number of FVM solvers for viscoelastic fluids have been built into OpenFOAM, [72, 75].

The robustness of finite volume computations in complex geometries via OpenFOAM is well documented, [72, 75]. In addition to the already cited examples such as [6, 7, 15, 72, 75], the investigations in [4, 5, 107] illustrate the versatility of the OpenFOAM platform in resolving complex fluid dynamical problems. The purpose of the present study is primarily, therefore, to extend the counter-flow heat-exchanger investigations of [9, 108] to the OpenFOAM framework so as to lay the groundwork for heat-exchanger investigations in more complex geometries. As in [9, 108], the counter-flow arrangement is chosen for its demonstrated optimality as compared to either parallel-flow or cross-flow arrangements.

For more comprehensive overview of the design, performance, and analysis of heat exchangers in various geometries and configurations, we refer the reader to the following recent works [109, 110, 111, 112, 113, 114, 115].

The remainder of the chapter is organized as follows. Section 2.3 gives the details of the physical model problem and corresponding governing equations. Section 2.4 focuses on the development and implementation of the numerical methodologies including the numerical stabilization techniques, i.e. the DEVSS and LCR methods. Section 2.5 gives the graphical illustrations and discussion of the model results. Concluding remarks follow in section 2.6.

## 2.3 Mathematical Modelling

### 2.3.1 Physical model

Fig. 2.1 gives an illustration of the physical model under investigation.

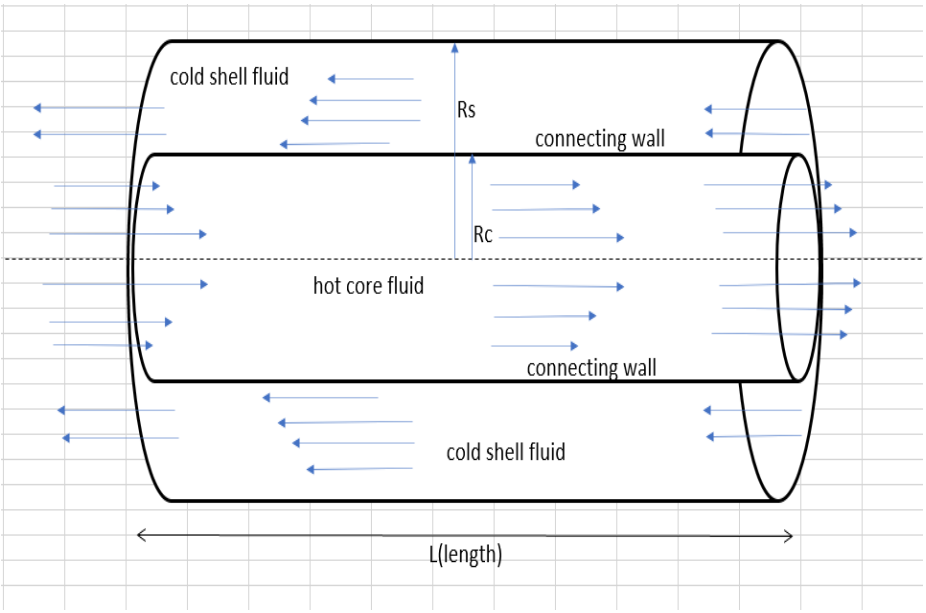


**Figure 2.1:** Schematics of the model problem.

Two cylindrical pipes with one located concentrically inside the other are arranged to form a double-cylinder (double-pipe) arrangement. Both cylinders are considered to of length $L$ in the longitudinal, $z$-direction. The inner cylinder (referred to as the core) has a radius $R_c$. The inner cylinder is symmetrically surrounded by an outer one (referred to as the shell) with a radius $R_s$ where clearly $R_s > R_c$. The model admits the cylindrical coordinate system $(r, \theta, z)$.

Axi-symmetric conditions are assumed and hence all flow quantities will be considered independent of the angle $\theta$. Specifically, the velocity vector $\boldsymbol{v} = (u, v, w)$ reduces to $\boldsymbol{v} = (u(r, z), 0, w(r, z))$. The fluid flow in the respective annuli will otherwise be

considered as laminar, incompressible, time-dependent, and non-isothermal driven by appropriate pressure gradients.

A heated viscoelastic fluid is confined to core region and hence will be referred to as the core fluid. A colder (coolant) Newtonian fluid fills the shell region (and is hence also referred to as the shell fluid) and flows in the opposite direction to the core fluid, leading to the counter-flow arrangement.

### 2.3.2 Dimensional governing equations for core-fluid

The core fluid is described by an incompressible, non-isothermal, viscoelastic fluid. The (2D) governing equations for the core fluid include [9, 10] the mass conservation,

$$\nabla^* \cdot \boldsymbol{U}_c^* = 0, \tag{2.1}$$

the momentum conservation,

$$\rho_c^* \left( \frac{\partial \boldsymbol{U}_c^*}{\partial t^*} + \boldsymbol{U}_c^* \cdot \nabla^* \boldsymbol{U}_c^* \right) = -\nabla^* p_c^* + \nabla^* \cdot \boldsymbol{\sigma}_c^* + \boldsymbol{F}_c^*, \tag{2.2}$$

and the energy conservation,

$$\rho_c^* C_{p_c}^* \left( \frac{\partial T_c^*}{\partial t^*} + T_c^* \cdot \nabla^* T_c^* \right) = Q_{D_c}^* - \nabla^* \cdot \boldsymbol{\Phi}_q^* + h_c^* (T_w^* - T_c^*). \tag{2.3}$$

In Eqs. (2.1) - (2.3), the asterisks ($^*$) represent dimensional variables, the underscore $()_c$ relates to the core fluid, $\nabla$ is the gradient operator, $\boldsymbol{U}_c$ the velocity field, $\rho_c$ the density, $t$ the time, $p_c$ the pressure field, $\boldsymbol{\sigma}_c$ the total stress tensor, $\boldsymbol{F}_c$ represents body forces, $C_{p_c}$ the specific heat at constant pressure, $T_c$ the fluid temperature,

$Q_{D_c}$ the internal heat production, $\Phi_{q_c}$ the heat flux vector, $T_w$ the connecting wall temperature, and $h_c$ and $h_s$ are a convective heat transfer parameters.

The total stress tensor is defined as,

$$\boldsymbol{\sigma}^* = -p_c^* \boldsymbol{I}^* + \boldsymbol{\tau_c}^* + \eta_c^* \boldsymbol{S}_c^*,$$

where $\boldsymbol{I}^*$ is the identity tensor, $\eta_c^*$ is the core fluid viscosity, $\boldsymbol{\tau}_c^*$ is the polymer-stress tensor, and

$$\boldsymbol{S}^* = \left[\nabla^* \boldsymbol{U}_c^* + (\nabla^* \boldsymbol{U}_c^*)^T\right],$$

is the rate of deformation tensor. The internal heat production is defined as,

$$Q_{D_c}^* = \gamma \boldsymbol{\tau}^* : \boldsymbol{S}_c^* + (1-\gamma)\eta_{\text{sol}}^* \boldsymbol{S}_c^* : \boldsymbol{S}_c^*,$$

where $\eta_{\text{sol}}^*$ is the solvent viscosity and $\gamma$ is a viscoelastic non-isothermal parameter, for more details, we refer the reader to [9, 10, 6, 116]. The heat flux will be described via Fourier's law

$$\boldsymbol{\Phi}_q^* = -\kappa_c^* \nabla^* T_c^*,$$

where $\kappa_c^*$ is the thermal conductivity. The polymer-stress tensor is governed by the Giesekus viscoelastic constitutive model,

$$\boldsymbol{\tau}^* + \alpha^* \boldsymbol{\tau}^{*2} + \lambda^* \overset{\nabla}{\boldsymbol{\tau}}^* = \eta_p^* \boldsymbol{S}_c^*, \tag{2.4}$$

where $\alpha^*$ is the Giesekus nonlinear parameter, $\lambda^*$ is the relaxation time, $\eta_p^*$ is the polymer viscosity, and $\overset{\nabla}{\boldsymbol{\tau}}^*$ is the upper convected time derivative;

$$\overset{\nabla}{\boldsymbol{\tau}}^* = \frac{\partial \boldsymbol{\tau}^*}{\partial t^*} + (\boldsymbol{U}_c^* \cdot \nabla^*)\boldsymbol{\tau}^* - (\nabla^* \boldsymbol{U}_c^*)\boldsymbol{\tau}^* - \boldsymbol{\tau}^*(\nabla^* U_c^*)^T.$$

The viscosity and relaxation time are assumed constant. The total viscosity is expressed as

$$\eta_c^* = \eta_{\text{sol}}^* + \eta_p^*.$$

### 2.3.3 Non-dimensional governing equations for core-fluid

The introduction of non-dimensional variables and dimensionless parameters can helpfully reduce the number of variables in the governing equations. The dimensionless parameters of interest are the Reynolds number ($Re_c$), the Prandtl number ($Pr_c$), the Deborah number ($De$), and the ratio of the polymer to total viscosity ($\beta$). Using scaling variables such as the maximum centerline velocity ($U_{c_0}^*$), the pipe length ($L^*$), etc. leads to the following dimensionless parameters and non-dimensional variables,

$$t = \frac{U_{c_0}^*}{L^*} t^*, \qquad \boldsymbol{\tau} = \frac{L^*}{\eta_c^* U_{c_0}^*} \boldsymbol{\tau}^*, \qquad p_c = \rho^* {U_{c_0}^*}^2 p_c^*, \qquad U_c = \frac{U_c^*}{U_{c_0}^*}$$

$$z = \frac{z^*}{L^*}, \qquad \nabla = L^* \nabla^*, \qquad \boldsymbol{S}_c = \frac{L^*}{U_{c_0}^*} \boldsymbol{S}_c^*, \qquad \mu_c = \frac{\eta_c^*}{\eta_{c_0}^*}$$

$$Re_c = \frac{\rho_c^* U_{c_0}^* d^*}{\eta_{c_0}^*}, \qquad Pr_c = \frac{C_{p_c}^* \eta_{c_0}^*}{K_c^*}, \qquad De = \frac{\lambda_0^* U_{c_0}^*}{d^*}, \qquad \beta = \frac{\eta_{p_0}^*}{\eta_{c_0}^*}$$

$$h_c = \frac{{L^*}^2}{K_c^*} h_c^*, \qquad \alpha = \frac{L^*}{\eta_{c_0}^* \mu_c^* U_{c_0}^*} \alpha^*.$$

The resultant non-dimensional governing equations read,

$$\nabla \cdot \boldsymbol{U}_c = 0, \tag{2.5}$$

$$\Big(\frac{\partial \boldsymbol{U}_c}{\partial t} + \boldsymbol{U}_c \cdot \nabla \boldsymbol{U}_c\Big) = -\nabla p_c + \frac{1}{Re_c}\nabla \cdot [\boldsymbol{\tau} + \boldsymbol{S}_c], \tag{2.6}$$

$$Re_c\, Pr_c\Big(\frac{\partial T_c}{\partial t} + \boldsymbol{U}_c \cdot \nabla T_c\Big) = \nabla^2 T_c + [\gamma(\tau : \boldsymbol{S}_c) + (1-\gamma)(1-\beta)\boldsymbol{S}_c : \boldsymbol{S}_c] + h(T_w - T_c), \tag{2.7}$$

$$\boldsymbol{\tau} + \alpha\boldsymbol{\tau}^2 + De_c \overset{\nabla}{\boldsymbol{\tau}} = \beta\, \boldsymbol{S}_c. \tag{2.8}$$

### 2.3.4 Governing equations for shell-fluid

The shell-fluid is assumed to be Newtonian and, given the thin annulus region that forms the shell, the shell-fluid is assumed to flow unidirectionally with velocity field $\boldsymbol{U}_s = (0, 0, w_s)$. The governing equations for the shell-fluid flow are otherwise similar to those for the core-fluid system but without the polymer-stress contributions and the 2D aspects. The equations, in non-dimensional format, for the mass, momentum,

and energy conservation for the shell fluid are respectively,

$$\frac{\partial w_s}{\partial z} = 0, \tag{2.9}$$

$$\frac{\partial w_s}{\partial t} + w_s \frac{\partial w_s}{\partial z} = \frac{1}{Re_s}\Big(\mu_s \frac{\partial^2 w_s}{\partial r^2} + \frac{\mu_s}{r}\frac{\partial w_s}{\partial r} + 2\mu_s \frac{\partial^2 w_s}{\partial z^2}\Big) + \frac{1}{Re_s}\Big(2\frac{\partial \mu_s}{\partial z}\frac{\partial w_s}{\partial z} + \frac{\partial \mu_s}{\partial r}\frac{\partial w_s}{\partial r}\Big), \tag{2.10}$$

$$Re_s Pr_s\Big(\frac{\partial T_s}{\partial t} + w_s \frac{\partial T_s}{\partial z}\Big) = \Big(\frac{\partial^2 T_s}{\partial r^2} + \frac{1}{r}\frac{\partial T_s}{\partial r} + \frac{\partial^2 T_s}{\partial z^2}\Big) + 2\mu_s\Big[2\Big(\frac{\partial w_s}{\partial z}\Big)^2 + \Big(\frac{\partial w_s}{\partial r}\Big)^2\Big] + h_s(T_w - T_s). \tag{2.11}$$

### 2.3.5 Governing equation for connecting wall

The shell-fluid and core-fluid are separated by a connecting wall across which convective heat transfer occurs. The governing equation for the temperature in the solid connecting wall is the one-dimensional heat conduction equation, which in non-dimensional form reads,

$$\frac{\partial T_w}{\partial t} = \frac{\partial^2 T_w}{\partial z^2} + h_c\,(T_c - T_w) + h_s\,(T_s - T_w)\,. \tag{2.12}$$

## 2.4 Numerical and Computational Methodologies

The finite volume methods are implemented on the OpenFOAM software platform to obtain the computational solutions to the model equations, Eqs. (2.5) - (2.12). We adapt the *viscoelasticFluidFoam* and *rheoMultiRegionFoam* which have been developed on the OpenFOAM platform, see for example [75], and which are suitable

for the simulation of the viscoelastic fluid flow. The solvers are modified for the present purposes by incorporating the energy equation for viscoelastic fluid flow, i.e. Eq. (2.7).

The computational mesh for the double-pipe geometry, Figure 2.2, is created via the OpenFOAM mesh generation functionality, *blockMesh*. In OpenFOAM language, this mesh is implemented over a *blockMeshDict* file, in which the geometry is conveniently defined and results are viewed using the *Paraview* software.

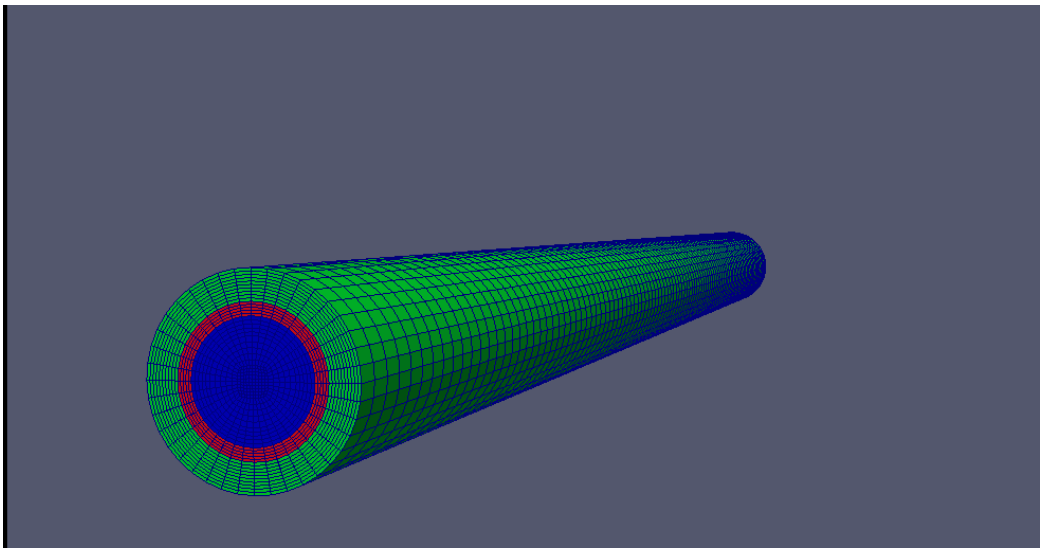

**Figure 2.2:** Computational mesh for the double-pipe geometry.

### 2.4.1 Pressure correction

The computational solution of incompressible pressure linked fluid flow equations is complicated by the reality that there is no explicit pressure equation to solve. Compressible flows on the other hand would, for example, have the ideal gas equation or some similar empirical law linking the pressure to the density and temperature. The incompressibility conditions, Eqs. (2.5) and (2.9), do not add any such useful information on the pressure. Various techniques have been developed

to overcome this challenge around pressure linked fluid flow equations. The current investigation employs one such technique, the Pressure-Implicit-with-Splitting-of-Operators (PISO) algorithm, see for example [117]. The PISO algorithm can be summarized as follows:

1. Initialize the flow fields; i.e. velocity $\boldsymbol{U}$, pressure $P$, stress $\boldsymbol{\tau}$, and temperature $T$.

2. For the LCR approach, replace and solve the stress equations using conformation tensor $\boldsymbol{D}$ (see later) or alternatively,

3. for the DEVSS approach, solve the polymer-stress equations for $\boldsymbol{\tau}$.

4. Solve the momentum equations to compute the intermediate velocity field $\boldsymbol{U}^{**}$.

5. Using the intermediate velocity field, $\boldsymbol{U}^{**}$, estimate a pressure field, $P^{**}$. Subsequently perform a correction of the intermediate velocity field and obtain the new velocity, $\boldsymbol{U}^{***}$, which must satisfying mass conservation.

6. The updated velocity, $\boldsymbol{U}^{***}$, is then used to compute the stresses, $\boldsymbol{\tau}^{**}$, and temperature, $T^{**}$, via the respective stress and energy equations.

7. Update $U$, $p$, $\boldsymbol{\tau}$, $T$ with $\boldsymbol{U}^{***}$, $P^{**}$, $\boldsymbol{\tau}^{**}$ and $T^{**}$ respectively and repeat the above steps until the required accuracies are achieved or until the required number of iterations is reached.

### 2.4.2 Simulations of the non-isothermal viscoelastic core-fluid flow

#### Initial and boundary conditions

The initial conditions are assumed to be zero for all fluid variables inside the core region, except for temperature which is initially set to 300 K. At the inlet section of the core region, the velocity is maintained at 2 m/s while pressure is assigned a zero-gradient boundary condition. We maintain zero initial conditions for the polymer-stresses throughout the core region. At the outlet, pressure is set to zero and a zero-gradient is used for all other fluid variables. The usual no slip boundary conditions are imposed for velocity at the pipe walls. Zero-gradient boundary conditions are implemented for pressure at the walls within the core region. The wall boundary condition for polymer-stresses are obtained via linear extrapolation, [9].

#### Discretization schemes for core region

As already indicated, the *viscoelasticFluidFoam* solver is employed to obtain the computational (FVM) solutions to the governing equations for the viscoelastic fluid flow. Given the transient nature of the model problem, the time derivatives are approximated in the solver via the implicit Euler scheme. The linear scheme with Gaussian integration is applied on space-gradient terms. For the convective terms, a Gauss first order upwind scheme is implemented. The Laplacian terms are treated via Gauss linear corrected (second order and bounded) schemes.

The systems of linear equations generated by the above time-and-space discretizations are handled as follows. A Bi-Conjugate Gradient Stabilized (BiCGStab) solver is used for the velocity, temperature, and polymer-stress constitutive equations. For the velocity and polymer-stress constitutive equations, the BiCGStab solver is used

in conjunction with the Incomplete LU with zero fill-in (ILUO) pre-conditioners. On the other hand, for the temperature equation, the BiCGStab solver is applied in conjunction with the Diagonal Incomplete LU (DILU) pre-conditioners. The pressure equation is solved using a Conjugate Gradient (CG) method using a Cholesky pre-conditioner.

### 2.4.3 Coupled simulations for the core, shell, and connecting-wall

#### Initial and boundary conditions

**Core-fluid:**

As already indicated for the core fluid system, the initial condition for velocity and temperature, at the pipe inlet, are prescribed (say to 2 m/s and 300 K respectively) while the polymer-stresses are initialized as zero. A zero gradient boundary condition is used for pressure. At the outlet, all fluid variables are assigned a zero-gradient boundary condition with an exception of pressure with a value of zero. At the walls of the pipe, no-slip boundary conditions are implemented for the velocity, linear extrapolation boundary conditions are employed for the polymer-stresses, and a zero-gradient boundary condition is imposed for the pressure. A coupled temperature-boundary condition is applied at the interface of the core-fluid and the connecting-wall. In the OpenFOAM framework, such a boundary condition is built into the *RheoTool* and *rheoMultiRegionFoam* solvers to ensure continuity of the heat flux across domain interfaces, see [72].

**Shell-fluid:**

The initial and inlet boundary conditions for the shell region, velocity, temperature, and pressure, are similar to those for the core fluid. At the outlet, the velocity and temperature are assigned zero-gradient boundary conditions while pressure is set to zero. At the walls, no-slip boundary conditions are assumed for the velocity while a zero-gradient boundary condition is used for pressure. As with the core-fluid/wall interface, a coupled temperature-boundary condition is applied at the interface of the shell-fluid and the connecting-wall.

**Connecting wall:**

Coupled temperature-boundary condition are applied at the interfaces on either side of the connecting wall, i.e. to both the wall/core-fluid interface and the wall/shell-fluid interface.

**Discretization schemes for the coupled simulations**

**Core-fluid region:**

The time derivatives are discretized via the implicit Euler scheme. A second order bounded Gauss linear scheme is used for the discretization of Laplacian terms. The least squares scheme is employed for the discretization of the gradient terms. The convective terms are discretized via a Universally Bounded Interpolation scheme (Cubista).

The solutions of the systems of linear equations for temperature, velocity, and polymer-stresses utilize a Preconditioned Bi-Conjugate Gradient (PBiCG) solver in

conjunction with a simplified Diagonal Incomplete LU (DILU) pre-conditioner. The pressure equation is solved with a Preconditioned Conjugate Gradient (PCG) solver using Diagonal Incomplete-Cholesky (DIC) pre-conditioners.

**Shell-fluid region:**

As with the core-fluid region, time derivatives are discretized with the implicit Euler scheme and a second order bounded Gauss linear scheme is employed for gradient terms. The Laplacian terms use a Gauss linear orthogonal scheme while Cubista and Gauss linear schemes are used in the discretization of convective terms.

The solver for the temperature and velocity equations is the PBiCGStab solver with a DILU pre-conditioner. A Geometric-Algebra Multi-Grid (GAMG) solver is used in conjunction with a DIC pre-conditioners for the solution of the pressure equation.

**Connecting wall:**

The gradient terms are discretized using the Gauss linear scheme, the Laplacian terms employ the second order bounded linear scheme, and the time derivatives utilize the implicit Euler scheme. In solving the temperature equation a PCG solver with DIC pre-conditioners is used.

**Numerical stability via the DEVSS technique**

Numerical stability is of fundamental importance in any computational and numerical methodologies. the *viscoelasticFluidFoam* solver employs the Discrete Elastic Viscous Stress Splitting (DEVSS) numerical stabilization technique in order to address numerical instabilities that may be attributed to the High Weissenberg Number Problem (HWNP).

In the DEVSS method an additional elliptic operator [99, 118] or diffusion term is added to each side of the momentum equations. In the subsequent time-discretizations, this elliptic term is evaluated implicitly on the left-hand side and explicitly on the right-hand side. The elliptic terms may be enhanced via scaling them with the polymeric viscosity, $\eta_p$, a process which further stimulates the stabilization of numerical iterative methods [76, 119]. Following the DEVSS technique, the momentum equations therefore take the form,

$$\rho\Big(\frac{\partial \boldsymbol{U}}{\partial t} + \boldsymbol{U}\cdot\nabla\boldsymbol{U}\Big) - \nabla\cdot(\eta_s+\eta_p)\nabla\boldsymbol{U} = -\nabla p - \nabla\cdot(\eta_p\nabla\boldsymbol{U}) + \nabla\cdot\boldsymbol{\tau} + \rho\boldsymbol{F}. \quad (2.13)$$

**Numerical stability via the LCR technique**

The Log-Conformation Reformulation (LCR) approach is implemented for numerical stabilization in the *RheoMultiRegionFoam* solver. In the LCR approach, the polymeric-stress tensor $\boldsymbol{\tau}$ is replaced with the logarithm of the conformation tensor, $\boldsymbol{D}$, where,

$$\boldsymbol{\tau} = \frac{\eta_p}{\lambda}(\boldsymbol{D} - \boldsymbol{I}). \quad (2.14)$$

The process to recast the stress constitutive equation in terms of the logarithm of conformation tensor (log-conformation) starts from replacing $\boldsymbol{\tau}$, from Eq. (2.14), in the stress constitutive equation. This initial process leads to the equation for the conformation tensor,

$$\frac{\partial \boldsymbol{D}}{\partial t} + (\boldsymbol{U}\cdot\nabla)\boldsymbol{D} - (\boldsymbol{D}\cdot\nabla\boldsymbol{U}^T + \nabla\boldsymbol{U}\cdot\boldsymbol{D}) = -\frac{1}{\lambda}f_R(\boldsymbol{D}), \quad (2.15)$$

where $f_R(\boldsymbol{D})$ is a polynomial function of the conformation tensor, [92]. The conformation tensor, $\boldsymbol{D}$, is positive definite and hence can be diagonalized,

$$\boldsymbol{D} = \boldsymbol{R} \cdot \boldsymbol{\Lambda} \cdot \boldsymbol{R}^T, \tag{2.16}$$

where $\boldsymbol{R}$ is an orthogonal tensor containing as its columns the eigenvectors of $\boldsymbol{D}$ and $\boldsymbol{\Lambda}$ is a diagonal matrix, the diagonal elements of which are the corresponding eigenvalues of $\boldsymbol{D}$.

The next step in the LCR technique then involves obtaining the natural logarithm of the conformation tensor, $\boldsymbol{D}$, i.e. $\boldsymbol{\Theta} = \log \boldsymbol{D}$. In particular,

$$\boldsymbol{\Theta} = \log \boldsymbol{D} = \boldsymbol{R} \cdot \log \boldsymbol{D} \cdot \boldsymbol{R}^T. \tag{2.17}$$

Following [92, 93], the velocity gradient, $\nabla \boldsymbol{U}$, can be decomposed as,

$$\nabla \boldsymbol{U} = \boldsymbol{\Omega} + \boldsymbol{B} + \boldsymbol{N} \cdot \boldsymbol{D}^{-1}, \tag{2.18}$$

where $\boldsymbol{\Omega}$ and $\boldsymbol{N}$ are anti-symmetric tensors and $\boldsymbol{B}$ is a symmetric, traceless tensor which commutes with $\boldsymbol{D}$. Eq. (2.15) therefore reduces to,

$$\frac{\partial \boldsymbol{\Theta}}{\partial t} + (\boldsymbol{U} \cdot \nabla)\boldsymbol{\Theta} - (\boldsymbol{\Omega}\boldsymbol{\Theta} - \boldsymbol{\Theta}\boldsymbol{\Omega}) - 2\boldsymbol{B} = \boldsymbol{R}\Big[\frac{1}{\lambda}(\Lambda^{-1} - 1)\Big]\boldsymbol{R}^T, \tag{2.19}$$

In a two-dimensional flow, the eigen-decomposition of $\boldsymbol{D}$ can be expressed as,

$$\boldsymbol{D} = \boldsymbol{R} \begin{bmatrix} \lambda_1 & 0 \\ 0 & \lambda_2 \end{bmatrix} \boldsymbol{R}^T, \tag{2.20}$$

where $\lambda_1$ and $\lambda_2$ are eigenvalues of $\boldsymbol{D}$ and also,

$$\boldsymbol{R}^T(\nabla \boldsymbol{U})\boldsymbol{R} = \begin{bmatrix} m_{11} & 0 \\ 0 & m_{22} \end{bmatrix}, \qquad \boldsymbol{B} = \boldsymbol{R}\begin{bmatrix} m_{11} & 0 \\ 0 & m_{22} \end{bmatrix}\boldsymbol{R}^T, \qquad \boldsymbol{\Omega} = \boldsymbol{R}\begin{bmatrix} \delta & 0 \\ 0 & -\delta \end{bmatrix}\boldsymbol{R}^T \tag{2.21}$$

where

$$\delta = \frac{(m_{12} + m_{21})}{(\lambda_2 - \lambda_1)}.$$

## 2.5 Numerical Results and discussion

### 2.5.1 Mesh Convergence

The mesh independence (or alternatively mesh convergence) in the present simulations is illustrated in Figure 2.3. The mesh sizes in Figure 2.3 correspond to the number of computational cells in Table 2.1.

**Table 2.1:** Mesh sizes corresponding to Figure 2.3.

| | |
|---|---|
| mesh 1 | 120,000 cells |
| mesh 2 | 203,125 cells |
| mesh 3 | 315,000 cells |

The numerical simulations incur quite high computational costs, especially noting the huge number of computational cells involved. It is imperative to carefully balance the mesh convergence requirements, on the one hand, against the computational costs on the other hand. Figure 2.3 illustrates mesh independence for the three mesh sizes given in Table 2.1. Noting the mesh independence as illustrated, the

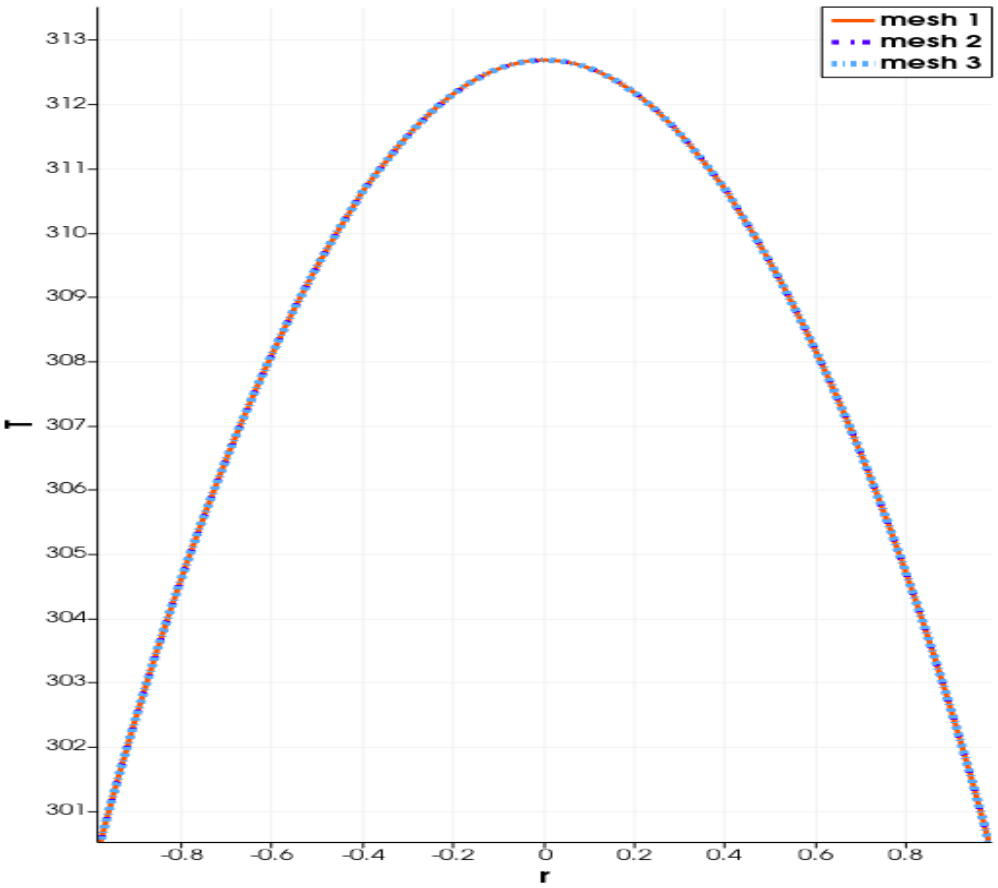


**Figure 2.3:** Illustration of mesh independence.

subsequent simulations in this work are all conducted via mesh size 1, i.e., with 120,000 computational cells.

### 2.5.2 Parameter values

Unless indicated otherwise, the following parameter values are used in the ensuing computations, $Re_c = 0.6$, $Re_s = 90$, $De = 0.4$, $Pr_c = 0.8$, $Pr_s = 3$, $\alpha = 0.2$, $\lambda = 0.5$, $\beta = 0.5$, $\eta_{sol} = 0.1$, $\eta_p = 0.1$, $K = 1$.

### 2.5.3 Flow characteristics in the core region

Fig. 2.4 illustrates the velocity profiles in the core region at a fixed $z$ values and across the pipe diameter. Specifically, the graphical results in Fig. 2.4(a)-(c) illustrate the view that one would observe if we were to slice the core cylinder at some point $z$ and then measure the fluid velocity across the (sliced) pipe cross-section. Fig. 2.4(a) shows the 3D parabolic profile that one would observe if the fluid were to gush at them from across the sliced cross-section. Similarly, Fig. 2.4(b) gives a contour illustration of the 3D profile and Fig. 2.4(c) is a 2D rendering of the parabolic profile. Fig. 2.4(d) gives an illustration of the fluid velocity in the $z$-direction, and shows as expected that the maximum velocities are located at the center of the channel and diminish towards the walls.

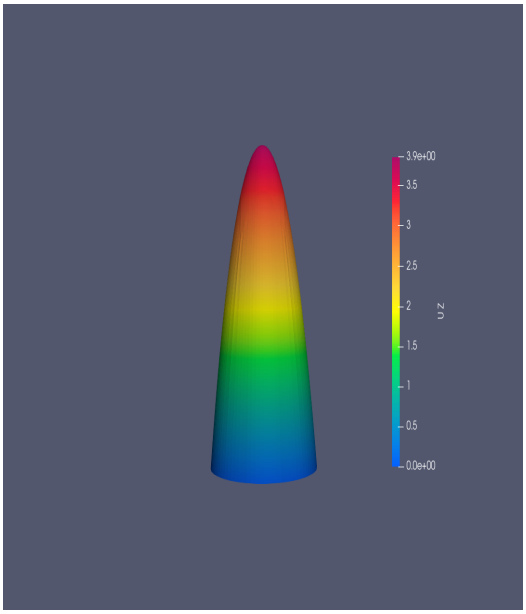


(a) 3D Surface plot

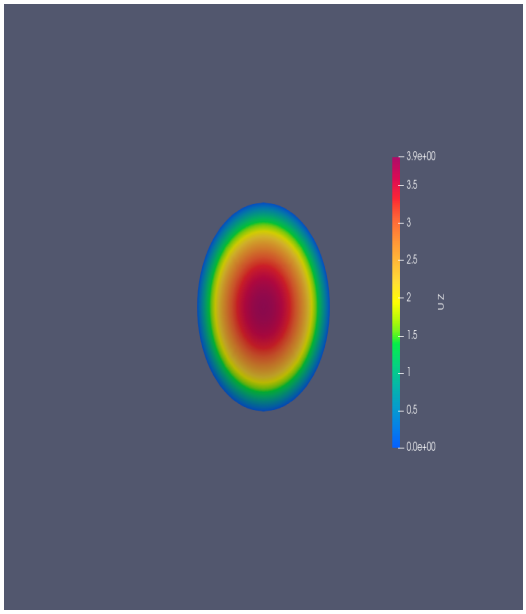


(b) Contour plot

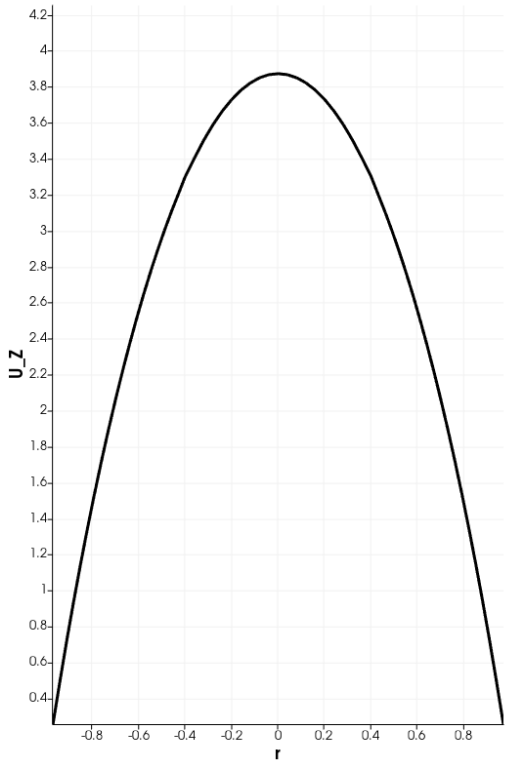


(c) 2D Cross-section

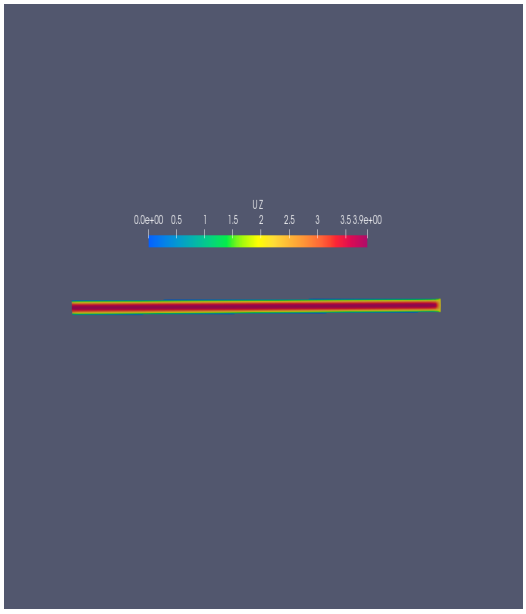


(d) View along pipe length

**Figure 2.4:** Velocity profiles

Figs. 2.5 and 2.6 are, respectively, the illustrations for the temperature and pressure profiles. Each of these illustrations is analogous to the velocity profiles as given in Fig. 2.4 and explained above.

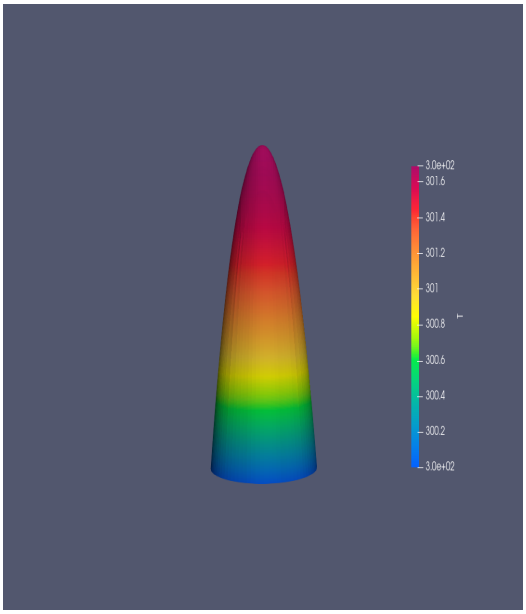


(a) 3D Surface plot

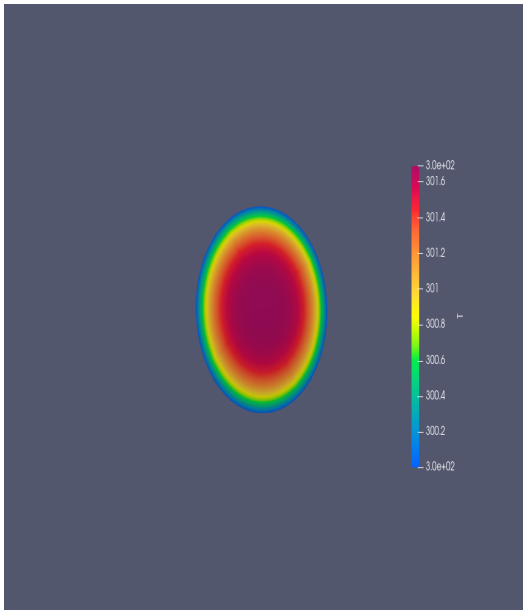


(b) Contour plot

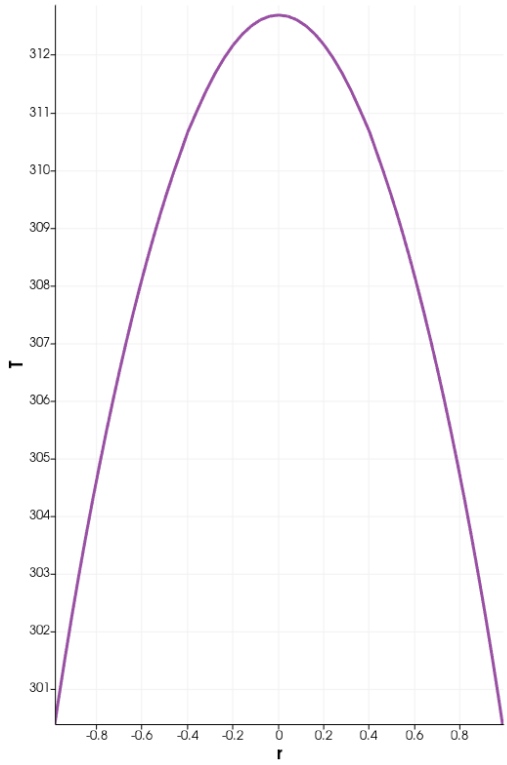


(c) 2D Cross-section

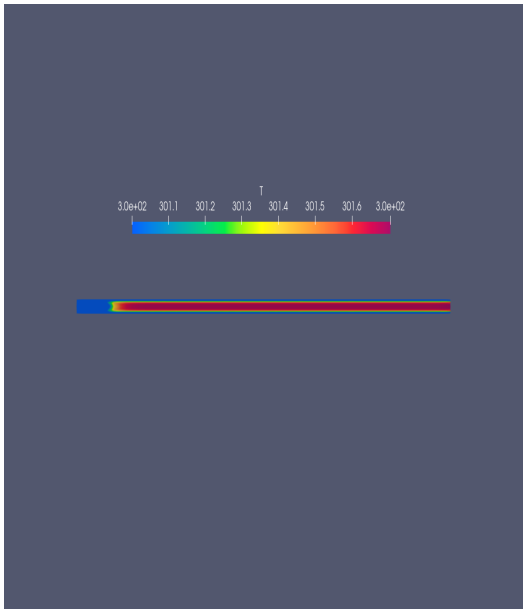


(d) View along pipe length

**Figure 2.5:** Temperature profiles

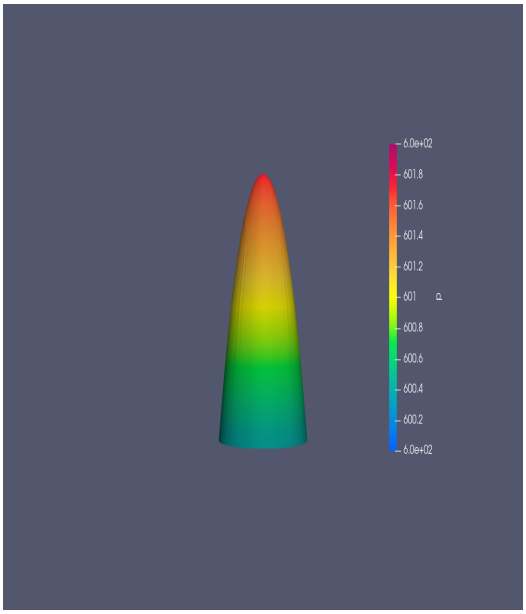


(a) 3D Surface plot

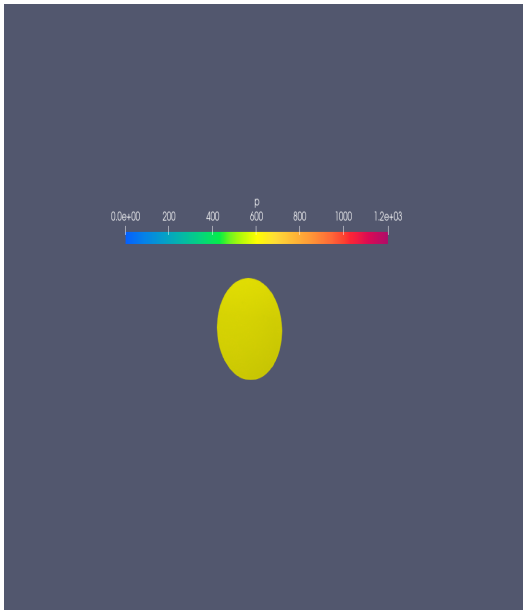


(b) Contour plot

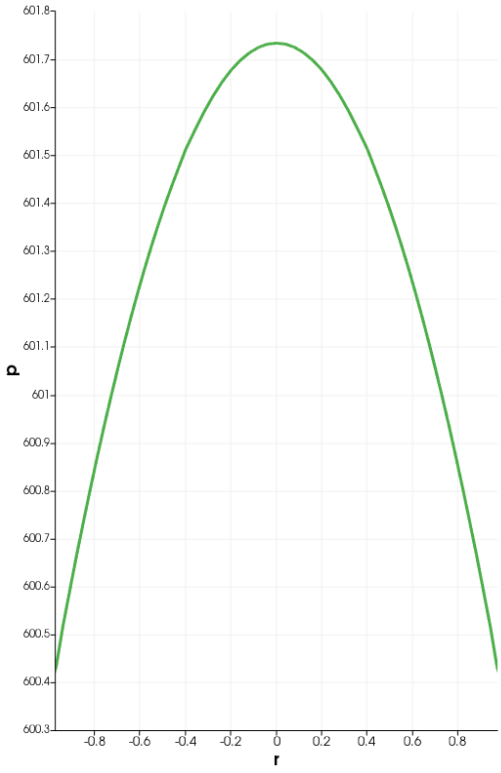


(c) 2D Cross-section

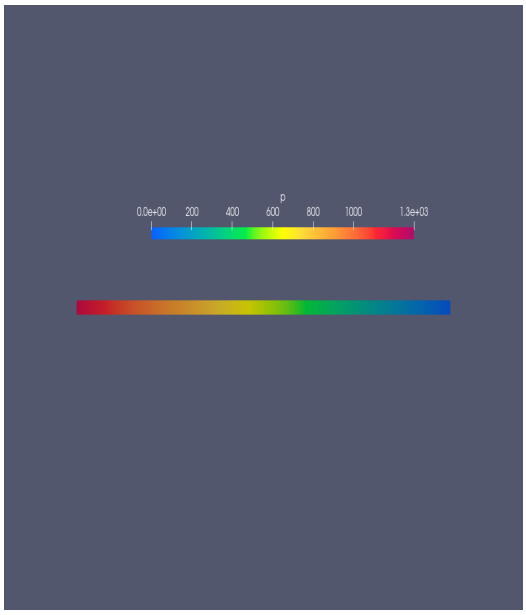


(d) View along pipe length

**Figure 2.6:** Pressure profiles

The first and second normal-stress differences, $N_1$ and $N_2$ are respectively defined as,

$$N_1 = \tau_{zz} - \tau_{rr} \quad \text{and} \quad N_2 = \tau_{rr} - \tau_{\theta\theta} = \tau_{rr},$$

where the final equality in the second normal-stress difference, $N_2$, equation results from the fact that $\tau_{\theta\theta} = 0$ for the axi-symmetric flow under consideration.

Figs. 2.7, 2.8, 2.9, and 2.10 are, respectively, the illustrations for $N_1$, $N_2$, $\tau_{rr}$, and $\tau_{zz}$. As required, the first normal-stress difference is non-negative, $N_1 \geq 0$.

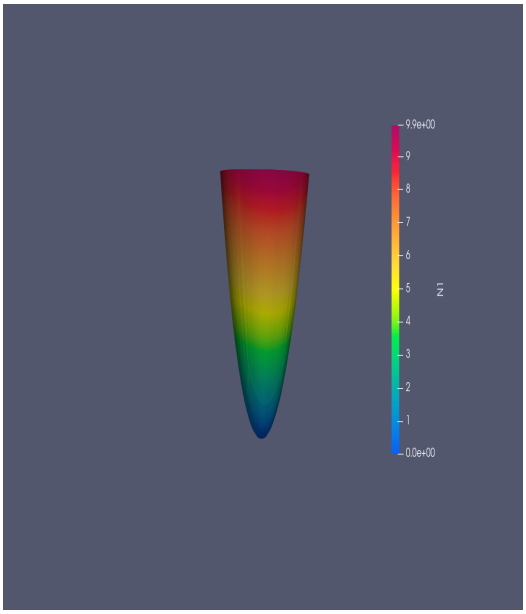


(a) 3D Surface plot

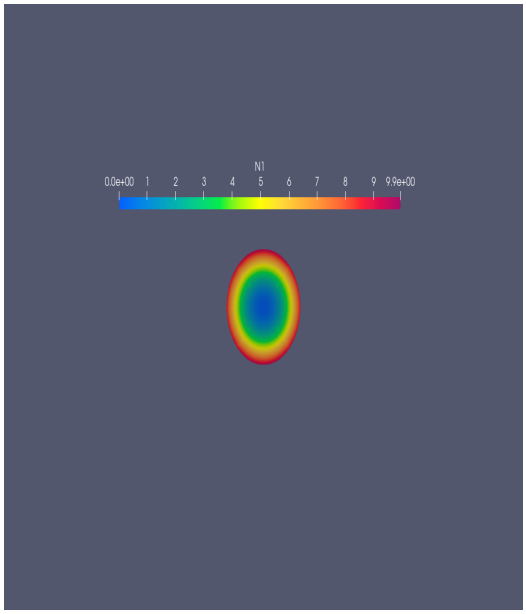


(b) Contour plot

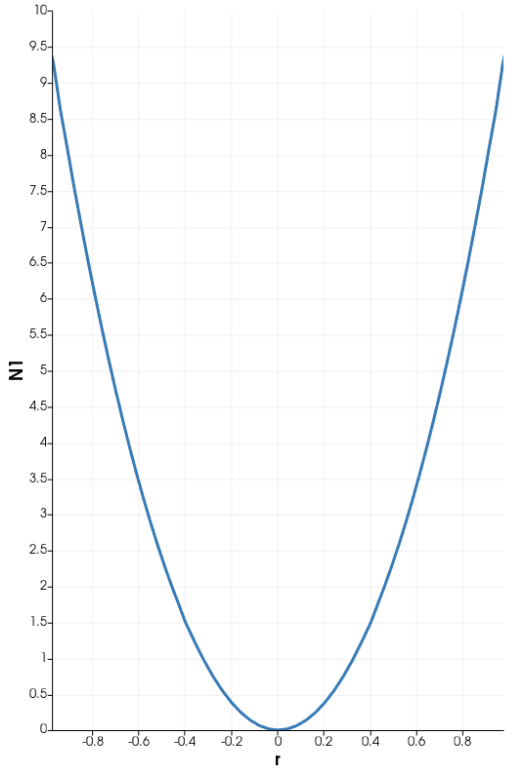


(c) 2D Cross-section

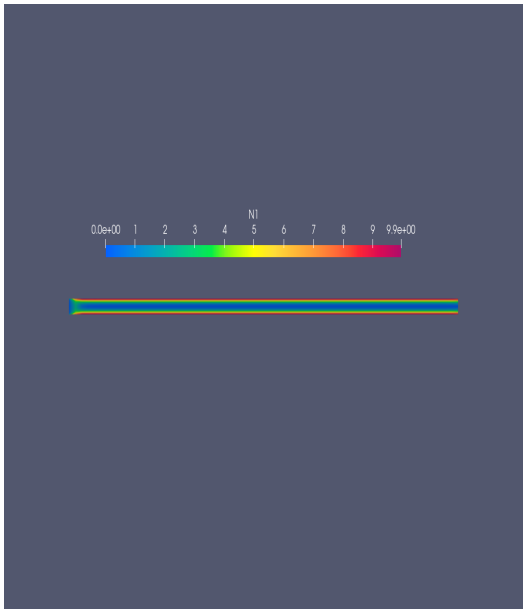


(d) View along pipe length

**Figure 2.7:** First normal stress difference ($N_1$) profiles

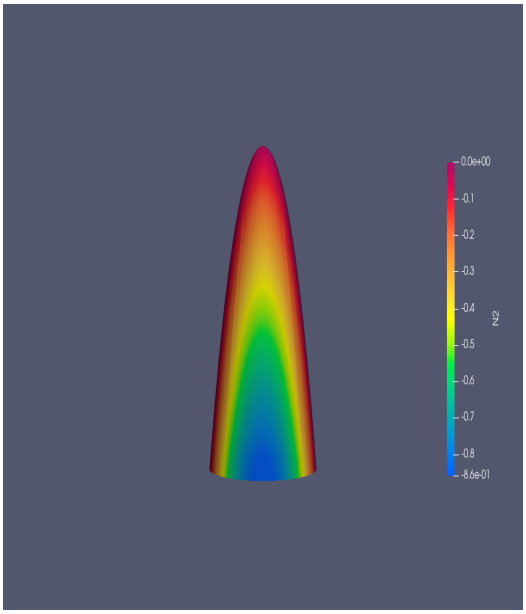


(a) 3D Surface plot

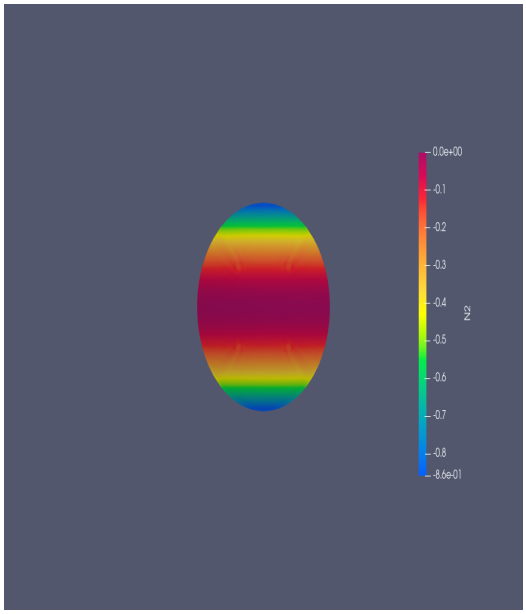


(b) Contour plot

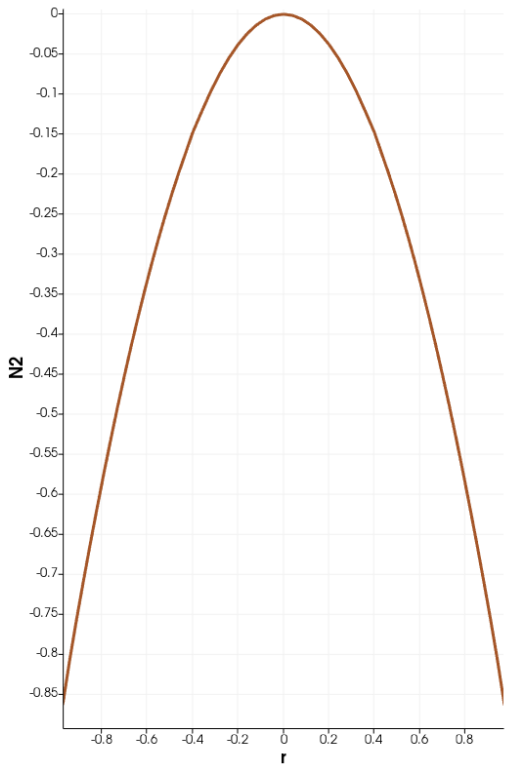


(c) 2D Cross-section

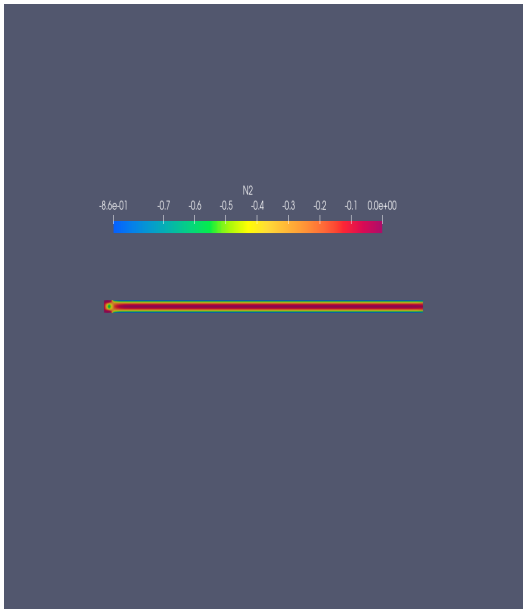


(d) View along pipe length

**Figure 2.8:** Second normal stress difference ($N_2$) profiles

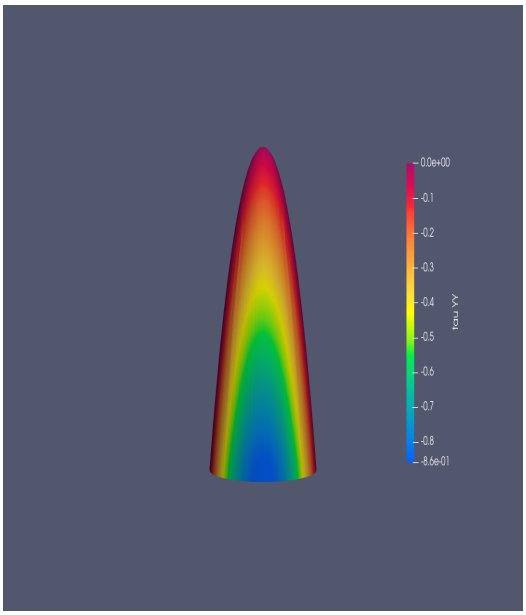


(a) 3D Surface plot

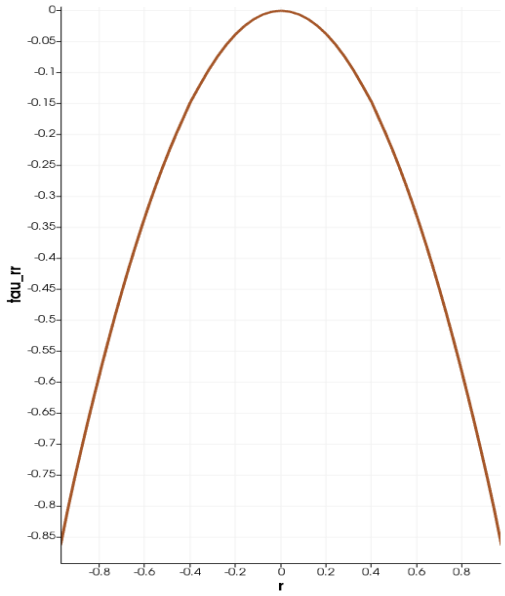


(b) 2D Cross-section

**Figure 2.9:** Diagonal stress profiles, $\tau_{11} = \tau_{rr}$

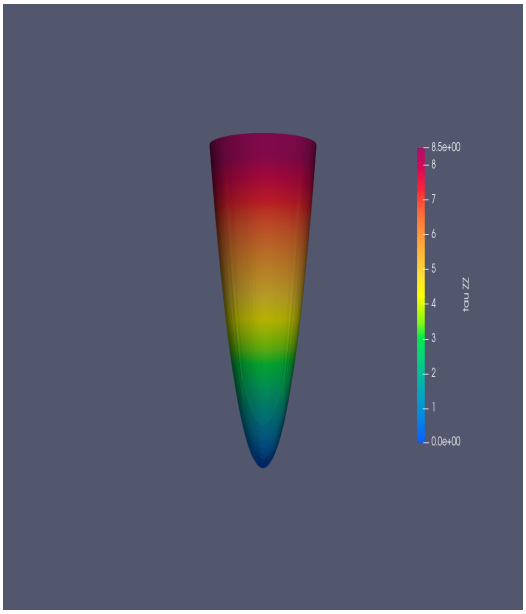


(a) 3D Surface plot

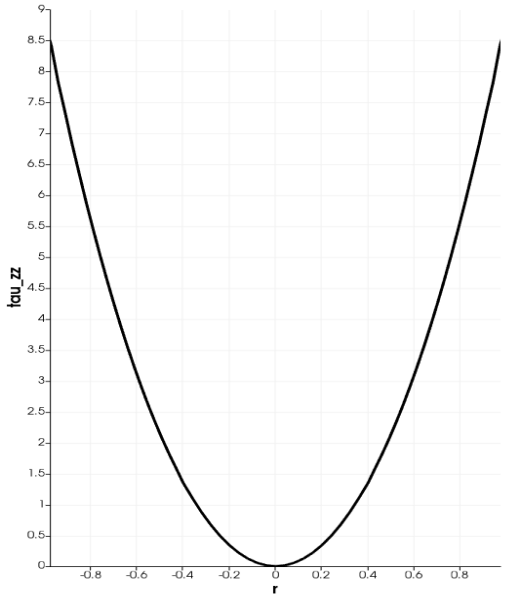


(b) 2D Cross-section

**Figure 2.10:** Diagonal stress profiles, $\tau_{33} = \tau_{zz}$

### 2.5.4 Heat-exchange characteristics

Fig. 2.11 shows the variation of the maximum core-fluid temperature (i.e. the temperature along the centerline, $r = 0$, of the core region) as we move from the inlet at $\mathbf{z} = 0$ to the outlet at $\mathbf{z} = 4$. In Fig. 2.11, the core region is therefore oriented from left (at $z = 0$) to right (at $z = 4$).

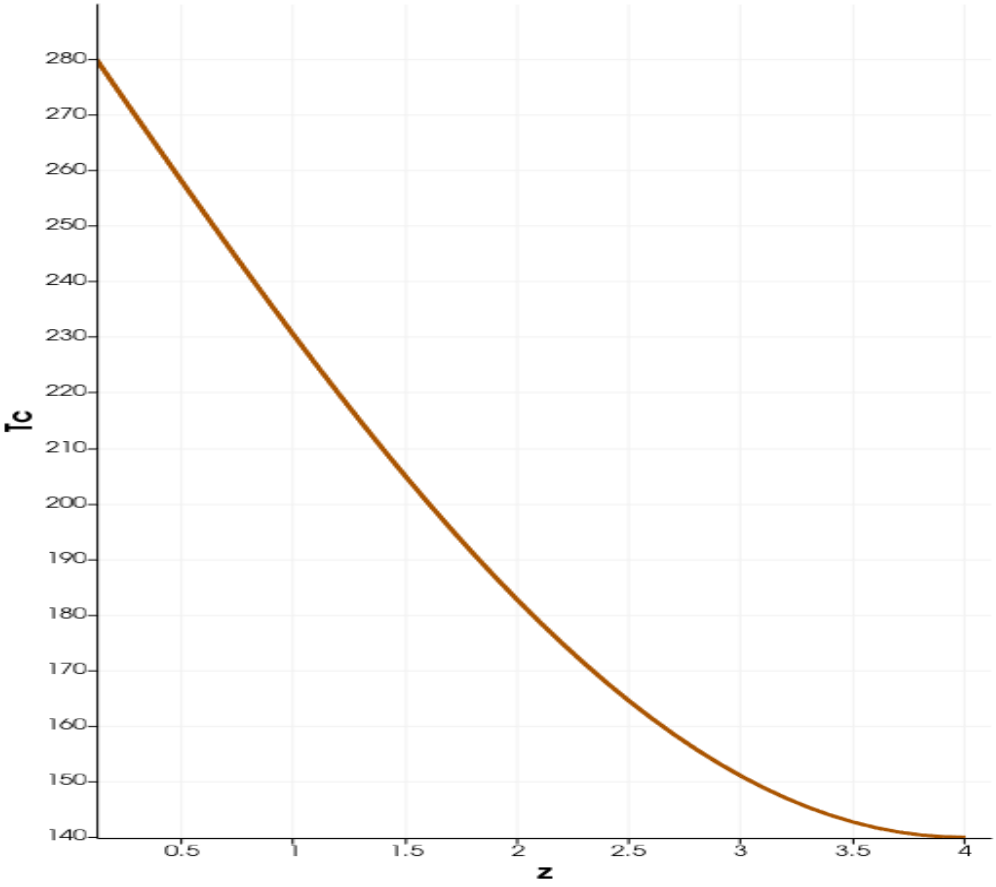


**Figure 2.11:** Core-fluid temperature profile from the inlet at $\mathbf{z} = 0$ to the outlet at $\mathbf{z} = 4$. Moving from left to right

The core-fluid temperature expectedly decreases along the longitudinal direction, from the high values at the inlet, $z = 0$, to the outlet at $z = 4$ where the lowest core-fluid temperatures are recorded. The observed reduction of the core-fluid temperature in the longitudinal ($z$) direction demonstrates the utility of the heat-exchanger,

specifically the hotter core-fluid is cooled by the colder shell-fluid via heat-exchange processes across the connecting wall.

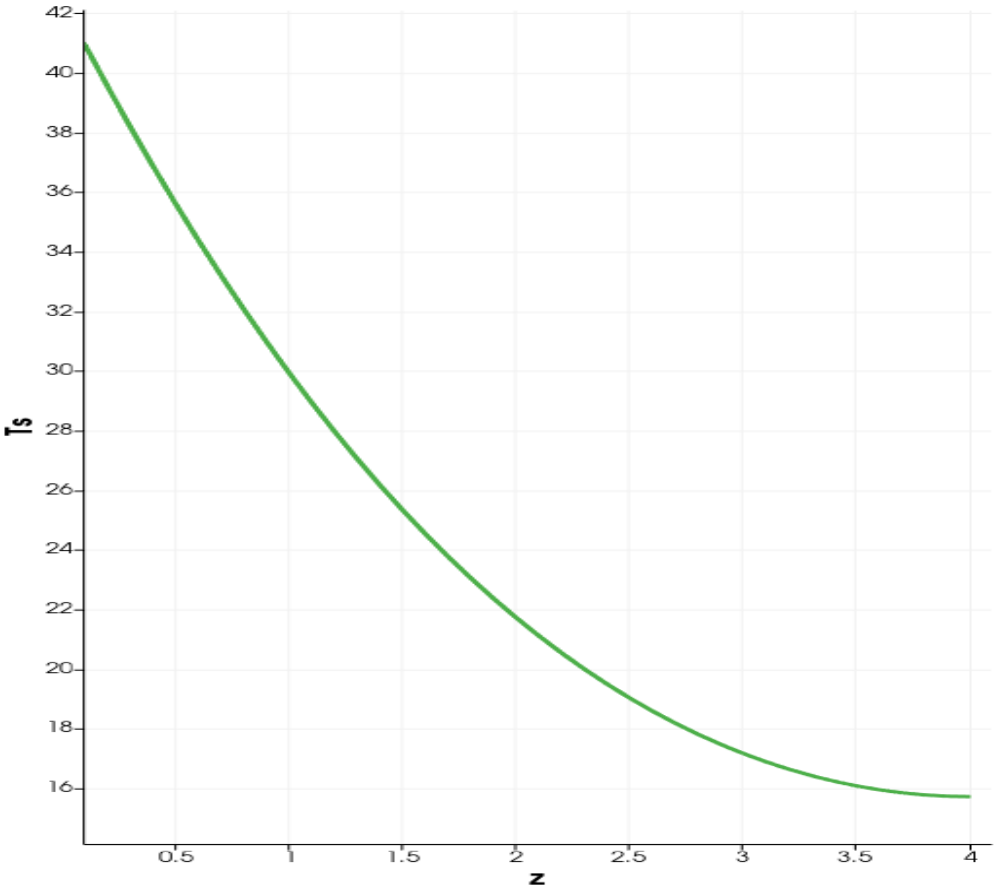


**Figure 2.12:** Shell-fluid temperature profile from the inlet at $\mathbf{z} = 4$ to the outlet at $\mathbf{z} = 0$. Moving from right to left

The shell-fluid temperature therefore expectedly behaves in the opposite manner to the core-fluid temperature, see Fig. 2.12. In the double-cylinder counter-flow arrangement, the shell fluid enters from the opposite end and moves in the opposite direction to the core-fluid.

In particular, the shell-fluid temperature expectedly increases along the longitudinal direction, from the high values at its inlet, $z = 4$, (which is located at the outlet

for the core-region) to the shell-outlet at $z = 0$ (which is located at the inlet for the core-region) where the highest shell-fluid temperatures are recorded.

The observed increase in the shell-fluid temperature in the counter-flow direction to the core-fluid similarly demonstrates the utility of the heat-exchanger, specifically the shell-fluid at the shell-exit ($z = 0$) would have absorbed the heat from across the entire length (from $z = 4 \searrow z = 0$) and hence would be expectedly hotter than the shell-fluid still close to the entry stages to the shell region.

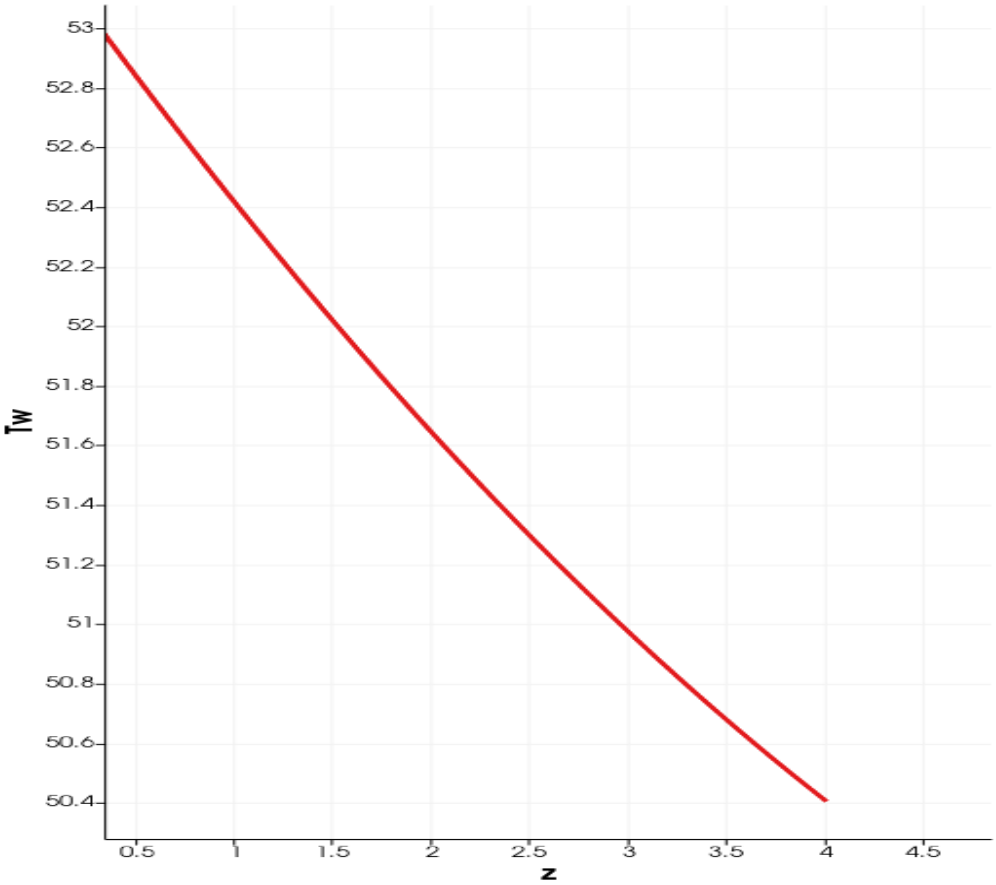


**Figure 2.13:** Connecting wall temperature profile

Fig. 2.13 illustrates the required behaviour of the wall temperature. The wall temperature would naturally be higher in the vicinity of the regions where the highest core-fluid temperatures are observed and vice versa. The magnitudes of the wall

temperature would be correspondingly lower than those of the core-fluid due to the convective heat-exchange taking place across the connecting-wall, from the hotter core-fluid to the colder shell-fluid. Similarly, the magnitudes of the wall temperature would still be higher than those of the shell-fluid due to the constant contact of the connecting-wall with the core-fluid whose temperature still remains higher than that of the shell fluid.

For these reasons, our future work will be focused on employing shell-fluids of various material and rheological compositions in order to enhance the heat-exchange characteristics and hence improve the efficiency of the heat-exchanger design.

## 2.6 Concluding Remarks

The results obtained in this Chapter set the groundwork for important applications, say to food processing, in which viscoelastic behaviour would be a significant factor. Indeed, the results obtained in this study, and the view to potential applications, lay the groundwork for follow-up work that would involve optimization investigation regarding the optimal design of the coolant composition and rheology. For example, contemporary research has demonstrated the heat transfer enhancement of nanofluids as compared to the corresponding base fluids. This is the context and framework of the next chapter in which investigations will focus on coolant fluids that are composed of nano-particles of varying volume fractions. Such fluids, i.e. base fluids containing nano-particles, are the so-called nanofluids.

# Chapter 3

# Modelling and Analysis of Viscoelastic and Nanofluid Effects on the Heat Transfer Characteristics in a Double-Pipe Counter-Flow Heat Exchanger*

## 3.1 Abstract

This study computationally investigates the heat transfer characteristics in a double-pipe counter-flow heat-exchanger. A heated viscoelastic fluid occupies the inner core region, and the outer annulus is filled with a colder Newtonian-Fluid-Based Nanofluid (NFBN). A mathematical model is developed to study the conjugate heat transfer characteristics and heat exchange properties from the hot viscoelastic fluid to the

*The contents of this chapter are from [120]

colder NFBN. The mathematical modelling and formulation of the given problem comprises of a system of coupled nonlinear partial differential Equations (PDEs) governing the flow, heat transfer, and stress characteristics. The viscoelastic stress behaviour of the core fluid is modelled via the Giesekus constitutive equations. The mathematical complexity arising from the coupled system of transient and nonlinear PDEs makes them analytically intractable, and hence, a recourse to numerical and computational methodologies is unavoidable. A numerical methodology based on the finite volume methods (FVM) is employed. The FVM algorithms are computationally implemented on the OpenFOAM software platform. The dependence of the field variables, namely the velocity, temperature, pressure, and polymeric stresses on the embedded flow parameters, are explored in detail. In particular, the results illustrate that an increase in the nano-particle volume-fraction, in the NFBN, leads to enhanced heat-exchange characteristics from the hot core fluid to the colder shell NFBN. Specifically, the results illustrate that the use of NFBN as the coolant fluid leads to enhanced cooling of the hot core-fluid as compared to using an ordinary (nano-particle free) Newtonian coolant.

## 3.2 Introduction

The development of efficient heat-transfer-fluids (HTF) continues to attract the attention of scientists and engineers given the widespread applications. The development and enhancement of efficient HTF has been widely investigated experimentally, theoretically, and computationally, see for example [121, 122, 123, 124, 125, 126, 127, 128, 129, 130, 131, 132, 133, 134]. Such widespread investigations have been conducted with a view to the important industrial applications of HTF, say, to polymer processing, food and beverage processing, chemical processing, pharmaceutical manufacture, etc.

The concept and development of nanofluids has largely arisen as a route to heat-transfer-rate (HTR) enhancement and efficient performance of HTF. Nanofluids are a dispersion of solid (metallic) nanometer-sized particles (nano-particles) in a base-fluid. The available literature, see for example [129, 135, 136, 137, 138], has shown that nanofluids exhibit higher thermal conductivities as compared to the conventional (and corresponding) base-fluids. The literature specifically demonstrates that such higher thermal conductivities of nanofluids lead to increases in heat-transfer-rates (HTR) as compared to the corresponding base-fluids. Additionally, ongoing research has demonstrated that the attractive heat-transfer characteristics of nanofluids can be further improved via various methods including increasing the Brownian motion of the embedded nano-particles suspended in the base-fluids [139, 140, 141], increasing volume-fraction of the embedded nano-particles [142, 143, 144], increasing the fluid layers around the embedded nano-particles [139, 140], etc. The present research specifically explores the effects, on HTR enhancement, of nano-particle volume-fraction (i.e., concentration of nano-particles) in the nanofluid.

In comparative investigations on the thermal conductivities of nanofluids versus the corresponding base-fluids, [145] reported that up to 30% increase in the thermal conductivity can be observed in nanofluids generated from various nano-particle/base-fluid combinations, e.g., $Al_2O_3$-water, $SiO_2$-water, and $TiO_2$-water. Similar results were also reported in [121] using $CuO$-water, $Al_2O_3$-water, and $Co$-oil nanofluids. The authors in [146] claimed a 100% increase in thermal conductivity for a range of volume-fractions 0.5–10% of aluminium particles in a water base. The results of [147] showed that a $Cu$-ethylene glycol nanofluid with a volume fraction of 0.3% produced a 40% increase in thermal conductivity. The investigation in [128] reported up to 78% rise in thermal conductivity for $Cu$-water nanofluids at a 7.5% volume fraction of nano-particles.

Akin to thermal conductivity enhancements investigations, studies have also been conducted on the effect of nanofluids on convective heat-transfer. The authors in [148], for example, investigated the performance of a nanofluid containing carbon nanotubes and observed that the convective heat-transfer rate can be as much as 3.5 times higher than that of the corresponding water base. Similarly, the authors in [149], using an $Al_2O_3$-water nanofluid, reported a convective heat-transfer rate rise of 40%. The investigations in [150] and [151], on the convective heat-transfer coefficient of deionised water with a dispersion of $Cu$ nano-particles for both laminar and turbulent flows in a tube, demonstrated higher convective heat-transfer coefficients for the nanofluids than for the deionised water base.

Even though nanofluids may physically never be truly homogeneous mixtures, the mathematical modelling of nanofluids is nonetheless generally divided into the two classes, namely single-phase (homogeneous) and two-phase (heterogeneous), see for example [152, 153, 154]. In the single-phase model, which is adopted in the present work, the nanofluid is treated as a homogeneous fluid mixture and the conventional fluid dynamical governing equations are modified to incorporate the volume-fractions of the embedded nano-particles, see for example [152, 153]. In the two-phase model, the base-fluid phase has its own fluid-dynamical governing equations, and a concentration equation is required to account for the effects of the suspended nano-particles, see for example [154]. Empirical investigations for the two-phase models have demonstrated that for nanofluids with low nano-particle volume fractions, the Lagrangian–Eulerian formulation is preferred, see for example [155], in which this approach was employed in analysing the HTR effects of $Cu$ and $Al_2O_3$ nano-particles under turbulent flow conditions. For the reverse scenario of nanofluids with high nano-particle volume fractions, the more suitable approach would be the Eulerian–Eulerian formulation, see for example [156], who conducted numerical simulations for

laminar forced convection heat-transfer of $Cu$-water nanofluids in isothermally heated microchannels.

In addition to the above motivations and literature on HTF, with regards to industrial heating and cooling applications, the present study is additionally spurred on by the investigations in [152, 153]. The investigations in [152, 153] specifically explored the non-isothermal effects of various viscoelastic-fluid-based nanofluids. Additional motivation arises from the works in [9, 86], which investigated the heat exchanger dynamics using particle-free viscoelastic and Newtonian fluids. The present investigation is aimed at the need to add to the literature on the development, design, and performance of industrial heat exchangers with a focus on the use and effects of nanofluids. The current work may also be extended to heat-exchange problems involving phase change and boiling, in which case the important surface-tension effects would need to be accounted for, including the effects to the energy conservation, see [157].

The present work employs finite volume computational methodologies implemented on the open-source OpenFOAM software platform [86, 101, 72, 73]. The OpenFOAM software platform offers the flexibility and convenience to incorporate new computational fluid dynamics (CFD) models via modifications of already-existing solvers, see for example [4, 5, 107, 8, 6]. The additional purpose of this work is therefore the development of a solver, under the OpenFOAM framework, for heat exchange investigations involving viscoelastic fluids and Newtonian-Fluid-Based Nanofluids (NFBN).

The chapter is structured as follows. In Section 3.3, the mathematical model formulation is presented. The development of numerical algorithms is given in Section 3.4. In Section 3.5, graphical computational results and discussion of results are presented. Finally, the concluding remarks are given in Section 3.6.

## 3.3 Mathematical Model

Two hollow concentric cylindrical pipes are arranged in a double-pipe geometry with an inner cylinder (the core) located inside an outer cylinder (the shell), see Figure 3.1. Both cylinders are of equal length, $L$, in the longitudinal direction, i.e., the $z$-direction.

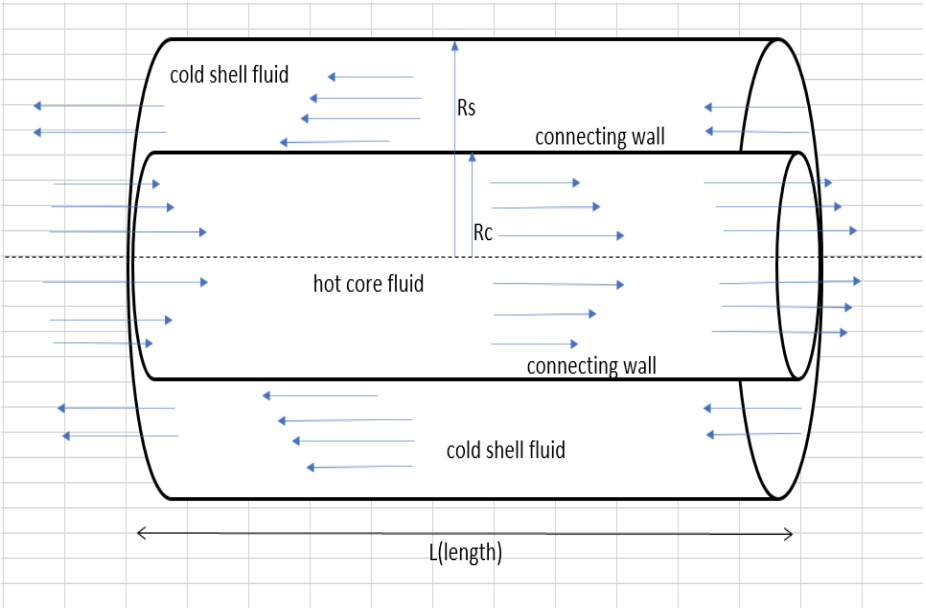


**Figure 3.1:** Schematics of the model problem.

The inner (core) cylinder has a radius $R_c$ in the radial direction, i.e., the $r$-direction, and is symmetrically surrounded by an outer cylinder (the shell) of radius $R_s$, with $0 < R_c < R_s$. The cylindrical coordinate system $(r, \theta, z)$ is adopted, with $r$ in the radial direction, $\theta$ in the angular direction, and $z$ in the longitudinal direction.

Axi-symmetric conditions are assumed, and hence, all flow field variables will be considered independent of $\theta$. For example, the velocity field would therefore be of the form $\boldsymbol{V} = (u(r, z), 0, w(r, z))$, where $u$ is the velocity component in the radial $(r)$ direction and $w$ is the velocity component in the longitudinal $(z)$ direction.

Laminar, incompressible, time-dependent, and non-isothermal conditions are additionally assumed. A heated/hot viscoelastic fluid occupies the inner core region and flows, say in the positive $z$-direction. A colder NFBN fills the outer annulus and flows in the opposite direction to the core fluid leading to the counter-flow arrangement.

### 3.3.1 Governing Equations for Core-Fluid

In dimensional terms, the governing mathematical equations for the viscoelastic core-fluid are derived from the conservation of mass, momentum, and energy, respectively, detailed in Equations (3.1)–(3.3):

$$\nabla^* \cdot \boldsymbol{U}_c^* = 0, \tag{3.1}$$

$$\rho_c^* \left( \frac{\partial \boldsymbol{U}_c^*}{\partial t^*} + \boldsymbol{U}_c^* \cdot \nabla^* \boldsymbol{U}_c^* \right) = -\nabla^* p_c^* + \nabla^* \cdot \boldsymbol{\sigma}_c^* + \boldsymbol{F}_c^*, \tag{3.2}$$

$$\rho_c^* C_{p_c}^* \left( \frac{\partial T_c^*}{\partial t^*} + T_c^* \cdot \nabla^* T_c^* \right) = Q_{D_c}^* - \nabla^* \cdot \boldsymbol{\Phi}_{q_c}^* + h_c^*(T_w^* - T_c^*). \tag{3.3}$$

The asterisks $*$ in Equations (3.1)–(3.3) represent dimensional variables, the subscript $()_c$ denotes core-fluid, $\nabla^*$ is the gradient operator, $\boldsymbol{U}_c^*$ is the velocity field, $\rho_c^*$ the density, $t^*$ the time, $p_c^*$ the pressure field, $\boldsymbol{\sigma}_c^*$ the total stress tensor, $\boldsymbol{F}_c^*$ represents body forces, $C_{p_c}^*$ is the specific heat at constant pressure, $T_c^*$ is the temperature field of the core fluid, $Q_{D_c}^*$ the internal heat production, $\boldsymbol{\Phi}_{q_c}^*$ the heat flux vector, $T_w^*$ is the connecting wall temperature, and $h_c^*$ and $h_s^*$ are a convective heat-transfer parameters.

The total stress tensor is given by:

$$\boldsymbol{\sigma}_c^* = -{p_c}^* \boldsymbol{I}^* + \boldsymbol{\tau}_c^* + \eta_c^* \boldsymbol{S}_c^*,$$

where $\boldsymbol{I}$ is the identity tensor, $\boldsymbol{\tau}_c^*$ represents the polymer-stress tensor, and

$$\boldsymbol{S}_c^* = \left[\nabla^* \boldsymbol{U}_c^* + (\nabla^* \boldsymbol{U}_c^*)^T\right],$$

is the rate of deformation tensor. The internal heat production is expressed as:

$$Q_{D_c}^* = \gamma \boldsymbol{\tau}^* : \boldsymbol{S}_c^* + (1-\gamma)\eta_{sol}^* \boldsymbol{S}_c^* : \boldsymbol{S}_c^*,$$

where $\eta_{sol}^*$ is the solvent viscosity and $\gamma$ is a viscoelastic non-isothermal parameter; for the full details, we refer the reader to [6, 9]. The heat flux is mathematically expressed by Fourier's law:

$$\Phi_{q_c}^* = -K_c^* \nabla^* T_c^*,$$

where $K_c^*$ is the thermal conductivity. The Giesekus viscoelastic constitutive equations are employed to model the polymeric stresses:

$$\boldsymbol{\tau}^* + \varepsilon^* \boldsymbol{\tau}^{*2} + \lambda^* \overset{\nabla}{\boldsymbol{\tau}}^* = \eta_p^* \boldsymbol{S}_c^*,$$

where $\varepsilon^*$ is the Giesekus nonlinear parameter, $\lambda^*$ is the relaxation time, $\eta_p^*$ is the polymer viscosity, and $\overset{\nabla}{\boldsymbol{\tau}}^*$ is the upper convected time derivative defined as:

$$\overset{\nabla}{\boldsymbol{\tau}}^* = \frac{\partial \boldsymbol{\tau}^*}{\partial t^*} + (\boldsymbol{U}_c^* \cdot \nabla^*)\boldsymbol{\tau}^* - (\nabla^* \boldsymbol{U}_c^*)\boldsymbol{\tau}^* - \boldsymbol{\tau}^*(\nabla^* \boldsymbol{U}_c^*)^T.$$

The relaxation time and viscosity are assumed constant with the total viscosity given by:

$$\eta_c^* = \eta_{sol}^* + \eta_p^*.$$

### 3.3.2 Governing Equations for Shell-Fluid

A Newtonian-Fluid-Based Nanofluid (NFBN) is assumed for the shell-fluid flowing in the outer annulus. The subscript $()_{sf}$, in the flow variables, is used to denote shell-fluid and the subscript $()_{nf}$ represents nanofluid. The governing equations for the shell-fluid flow are otherwise similar to those for the core-fluid system, but without the polymer-stress contributions. The equations, in a dimensional form, read:

$$\nabla^* \cdot \boldsymbol{U}^*_{sf} = 0, \tag{3.4}$$

$$(\rho_{sf})^*_{nf} \left( \frac{\partial \boldsymbol{U}^*_{sf}}{\partial t^*} + \boldsymbol{U}^*_{sf} \cdot \nabla^* \boldsymbol{U}^*_{sf} \right) = -\nabla^* p^*_{sf} + \nabla^* \cdot \boldsymbol{\sigma}^*_{sf}, \tag{3.5}$$

$$(\rho_{sf} C_{p_{sf}})^*_{nf} \left( \frac{\partial T^*_s}{\partial t^*} + T^*_{sf} \cdot \nabla^* T^*_{sf} \right) = Q^*_{D_{sf}} - \nabla^* \cdot \boldsymbol{\Phi}^*_{q_{sf}}. \tag{3.6}$$

where $(\rho_{sf})^*_{nf}$ is the NFBN density, $\sigma^*_{sf}$ the total stress tensor, $(\rho_{sf} C^*_{p_{sf}})^*_{nf}$ the NFBN specific heat capacity, $Q^*_{D_{sf}}$ the internal heat production, and $\boldsymbol{\Phi}^*_{q_{sf}}$ the heat-flux vector. The total stress tensor for the shell-fluid is defined as:

$$\boldsymbol{\sigma}^*_{sf} = \frac{\eta^*_{sol}}{\sqrt{(1-\varphi)^5}} \boldsymbol{S}^*_{sf},$$

where $\varphi$ is the nano-particle volume-fraction. The internal heat production is defined as:

$$Q^*_{D_{sf}} = \frac{\eta^*_{sol}}{\sqrt{(1-\varphi)^5}} \boldsymbol{S}^*_{sf} : \nabla^* \boldsymbol{U}^*_{sf}.$$

The heat-flux vector follows Fourier's law:

$$\boldsymbol{\Phi}^*_{q_{sf}} = -K^*_{nf} \nabla^* T^*_{sf},$$

where $K^*_{nf}$ is the nanofluid thermal conductivity, which is defined as:

$$K^*_{nf} = \frac{K^*_s + (1-\aleph)K^*_f + (1-\aleph)\varphi(K^*_f - K^*_s)}{K^*_s + (1-\aleph)K^*_f + \varphi(K^*_f - K^*_s)}(1 + \alpha A_2 T^*_s),$$

where $A_2$ is a thermal-conductivity parameter and $\aleph$ is an empirical shape-factor. For spherical-shaped nano-particles, which are assumed in the present work, $\aleph = 3$, [158].

The nanofluid quantities, $()_{nf}$, are obtained from linear combinations of the volume-fractions, $\varphi$, of the base-fluid contribution, $()_f$, and the nano-particle contribution, $()_s$. For example:

$$\rho^*_{nf} = \varphi(\rho_{sf})^*_s + (1-\varphi)(\rho_{sf})^*_f,$$

$$(\rho_{sf}C_{p_{sf}})^*_{nf} = \varphi(\rho_{sf}C_{p_{sf}})^*_s + (1-\varphi)((\rho_{sf}C_{p_{sf}})^*_f.$$

### 3.3.3 Governing Equation for the Connecting Wall

The shell-fluid and core-fluid are separated by a connecting wall through which heat-exchange occurs. The governing equation for the connecting wall temperature, $T^*_w$, follows the one-dimensional heat conduction equation:

$$\frac{\partial T^*_w}{\partial t^*} = \frac{\partial^2 T^*_w}{\partial z^{*2}} + h^*_c(T^*_c - T^*_w) + h^*_{sf}(T^*_{sf} - T^*_w). \tag{3.7}$$

## 3.4 Numerical Algorithms and Computational Methodologies

Equations (3.1)–(3.7) are solved numerically using Finite Volume Methods (FVM). The FVM numerical algorithms are implemented on the OpenFOAM software platform. The OpenFOAM computational solvers that are developed in the present work are adapted and modified from both the *viscoelasticFluidFoam* and the *rheoMultiRegionFoam* solvers, which pre-exist on OpenFOAM, see for example [72, 73]. These two pre-existing solvers are well adapted to viscoelastic flow simulations, and hence, they are well suited as starting points for the development of the viscoelastic computations required in the present work.

The computational mesh for the double-pipe geometry, Figure 3.2, is created using the OpenFOAM mesh generation functionality called *blockMesh*. In OpenFOAM language, this mesh is implemented over a *blockMeshDict* file, in which the geometry is conveniently defined and results are viewed using the *Paraview* software.

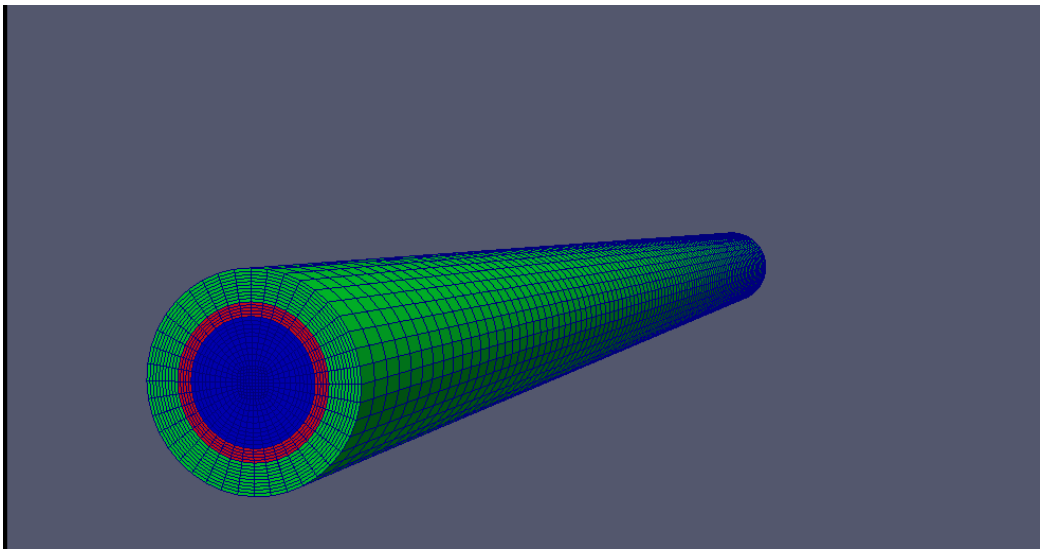

**Figure 3.2:** Computational mesh for the double-pipe geometry.

Viscoelastic flow computations are prone to numerical difficulties which arise at high Weissenberg, $We$, or alternatively at high Deborah, $De$, numbers, leading to the so-called High-Weissenberg-Number-Problem (HWNP). The higher the Weissenberg (or Deborah) number, the more pronounced would be the elastic effects, in which case the viscoelastic fluid largely exhibits solid-like behaviour leading to the numerical instabilities for the fluid-based computations. Both the Discrete-Elastic-Viscous-Stress-Splitting (DEVSS) [73, 76] and the Log-Conformation-Reformulation (LCR) techniques [92, 93] are employed to mitigate against numerical instabilities arising from the HWNP.

### 3.4.1 DEVSS Technique

In the Discrete-Elastic-Viscous-Stress-Splitting (DEVSS) method, employed in the *viscoelasticFluidFoam* solver, an additional elliptic operator [99] is added on each side of the momentum equations. The stabilising effects of the elliptic terms may be enhanced by scaling them with the polymeric viscosity, $\eta_p$, [76, 119]. Under the DEVSS technique, the momentum equations take the form:

$$\rho\left(\frac{\partial \boldsymbol{U}}{\partial t} + \boldsymbol{U}\cdot\nabla\boldsymbol{U}\right) - \nabla\cdot(\eta_s+\eta_p)\nabla\boldsymbol{U} = -\nabla p - \nabla\cdot(\eta_p\nabla\boldsymbol{U}) + \nabla\cdot\boldsymbol{\tau} + \rho\boldsymbol{F}. \quad (3.8)$$

### 3.4.2 LCR Technique

The Log-Conformation-Reformulation (LCR) approach is implemented for numerical stabilisation in the *RheoMultiRegionFoam* solver. In the LCR approach, the polymeric-stress tensor, $\boldsymbol{\tau}$, is replaced with the logarithm of the conformation tensor, $\boldsymbol{D}$, where:

$$\boldsymbol{\tau} = \frac{\eta_p}{\lambda}(\boldsymbol{D} - \boldsymbol{I}). \quad (3.9)$$

The process to recast the viscoelastic-stress constitutive-equations in terms of the logarithm of conformation tensor (log-conformation) requires that the stress tensor, $\boldsymbol{\tau}$, be initially replaced (in the viscoelastic-stress constitutive-equations) by the conformation tensor, $\boldsymbol{D}$, via Equation (3.9). This initial process leads to the alternative constitutive equations for the conformation tensor:

$$\frac{\partial \boldsymbol{D}}{\partial t} + (\boldsymbol{U} \cdot \nabla)\boldsymbol{D} - (\boldsymbol{D} \cdot \nabla \boldsymbol{U}^T + \nabla \boldsymbol{U} \cdot \boldsymbol{D}) = -\frac{1}{\lambda} f_R(\boldsymbol{D}), \tag{3.10}$$

where $f_R(\boldsymbol{D})$ is a polynomial function in the conformation tensor [141]. Since $\boldsymbol{D}$ is positive definite, it can be diagonalised that:

$$\boldsymbol{D} = \boldsymbol{R} \cdot \boldsymbol{\Lambda} \cdot \boldsymbol{R}^T, \tag{3.11}$$

where $\boldsymbol{R}$ is an orthogonal matrix containing, as its columns, the eigenvectors of $\boldsymbol{D}$, and $\boldsymbol{\Lambda}$ is a diagonal matrix with corresponding eigenvalues of $\boldsymbol{D}$. The second step in the LCR technique is based on the realisation that it would be more efficient to solve constitutive equation in terms of the logarithm of $\boldsymbol{D}$ (i.e., introduce and solve for, $\boldsymbol{\Theta} = \log \boldsymbol{D}$, in the constitutive equations) rather than solving directly for $\boldsymbol{D}$. In particular:

$$\boldsymbol{\Theta} = \log \boldsymbol{D} = \boldsymbol{R} \cdot \log \boldsymbol{\Lambda} \cdot \boldsymbol{R}^T. \tag{3.12}$$

Following [92, 93], the velocity gradient, $\nabla \boldsymbol{U}$ can be decomposed as:

$$\nabla \boldsymbol{U} = \boldsymbol{\Omega} + \boldsymbol{B} + \boldsymbol{N} \cdot \boldsymbol{D}^{-1}, \tag{3.13}$$

where both $\boldsymbol{\Omega}$ and $\boldsymbol{N}$ are anti-symmetric and $\boldsymbol{B}$ is a symmetric traceless tensor which commutes with $\boldsymbol{D}$. Equation (3.10), therefore, reduces to:

$$\frac{\partial \boldsymbol{\Theta}}{\partial t} + (\boldsymbol{U} \cdot \nabla)\boldsymbol{\Theta} - (\boldsymbol{\Omega}\boldsymbol{\Theta} - \boldsymbol{\Theta}\boldsymbol{\Omega}) - 2\boldsymbol{B} = \boldsymbol{R}\left[\frac{1}{\lambda}(\boldsymbol{\Lambda}^{-1} - 1)\right]\boldsymbol{R}^T. \tag{3.14}$$

In a two-dimensional flow, the eigen-decomposition of $\boldsymbol{D}$ can be expressed as:

$$\boldsymbol{D} = \boldsymbol{R}\begin{bmatrix}\lambda_1 & 0\\ 0 & \lambda_2\end{bmatrix}\boldsymbol{R}^T, \tag{3.15}$$

where $\lambda_1$ and $\lambda_2$ are eigenvalues of $\boldsymbol{D}$, and also:

$$\boldsymbol{R}^T(\nabla \boldsymbol{U})\boldsymbol{R} = \begin{bmatrix}m_{11} & 0\\ 0 & m_{22}\end{bmatrix}, \quad \boldsymbol{B} = \boldsymbol{R}\begin{bmatrix}m_{11} & 0\\ 0 & m_{22}\end{bmatrix}\boldsymbol{R}^T, \quad \Omega = \boldsymbol{R}\begin{bmatrix}\delta & 0\\ 0 & -\delta\end{bmatrix}\boldsymbol{R}^T, \tag{3.16}$$

with:

$$\delta = \frac{(m_{12} + m_{21})}{(\lambda_2 - \lambda_1)}.$$

### 3.4.3 Pressure Correction

Unlike for compressible flow, where empirical relations such as the ideal gas law allow for a direct/explicit pressure-linked equation, the solution processes for pressure-linked equations for incompressible fluid flow on the other hand are complicated by the reality that there is no explicit pressure equation to solve. Numerical solutions for pressure-linked equations of incompressible fluid flow have led to the development of various techniques to overcome this difficulty. The current investigation employs the Pressure-Implicit-with-Splitting-of-Operators (PISO) algorithm, see for example [117], to deal with this challenge. The PISO algorithm can be summarised as follows.

1. Initialise the field variables: velocity $\boldsymbol{U}$, pressure $p$, polymeric stresses $\boldsymbol{\tau}$, and temperature $T$.

2. For the LCR approach, solve for the conformation tensor $\boldsymbol{D}$ and $\boldsymbol{\Theta} = \log \boldsymbol{D}$.

3. For the DEVSS approach, solve directly for the polymer stresses, $\boldsymbol{\tau}$.

4. Solve the momentum equations for the intermediate velocity field, $\boldsymbol{U}^{**}$.

5. Using the intermediate velocity, $U^{**}$, estimate a new pressure field $p^{**}$. Subsequently, perform a correction of the intermediate velocity field and obtain the new velocity $\boldsymbol{U}^{***}$, which must satisfy mass conservation.

6. The updated velocity $\boldsymbol{U}^{***}$ is then used to compute the polymer-stresses $\boldsymbol{\tau}^{**}$ and temperature $T^{**}$ via the stress constitutive equations and energy equations, respectively.

7. Go to step 1 with the field variables $\boldsymbol{U}$, $p$, $\boldsymbol{\tau}$, $T$, respectively, replaced with $U^{***}$, $p^{**}$, $\tau^{**}$, and $T^{**}$ and repeat the steps until the required accuracies are achieved or until the required number of iterations is reached.

### 3.4.4 Core-Fluid Simulations

#### Initial and Boundary Conditions in Core Region

The initial conditions are assumed to be zero for all fluid variables except for core temperature, which is initially set to 300 K. At the inlet regions of the pipe sections, the velocities are kept at 2 m/s while pressure is assigned a zero gradient boundary condition. The polymer-stresses are initially fixed at zero throughout the core region. At the outlet, a zero gradient condition is assigned for all fluid variables except for pressure, which is set to zero. The usual no-slip boundary conditions are imposed for

velocity at the pipe walls. A zero gradient condition is imposed for polymer-stresses at the pipe walls.

### Discretisation Schemes for Core Region

Since the model problem is transient in nature, time discretisation is crucial and must be implemented in a way that enhances numerical stability and convergence. The time derivatives are, therefore, approximated via an implicit Euler scheme. A linear scheme with Gaussian integration is applied on space derivative terms, i.e., the gradient terms. A Gaussian first order upwind scheme is used for the discretisation of the convective terms. The Laplacian terms are discretised via bounded, second-order Gaussian linear corrected schemes.

The systems of linear equations generated by the above space-time discretisations are solved via efficient and robust linear algebraic techniques. Specifically, a Bi-Conjugate Gradient Stabilised (BiCGStab) solver is used for the discretised velocity, temperature, and polymer-stress constitutive equations. For the discretised velocity and polymer-stress constitutive equations, the BiCGStab solver is applied in conjunction with the Incomplete LU with zero fill-in (ILUO) pre-conditioners. For the discretised temperature equation, the BiCGStab solver is used in conjunction with the Diagonal Incomplete LU (DILU) pre-conditioners. The pressure equation is solved with a Conjugate Gradient (CG) method using a Cholesky pre-conditioner.

### 3.4.5 Coupled Simulations for Core-Fluid, Shell-Fluid, and Connecting Wall

#### Initial and Boundary Conditions for Coupled Simulations—Core-Fluid

As already mentioned for the core fluid system, the initial conditions for temperature and velocity, at the core inlet, are 2 m/s and 300 K, respectively, while the polymer-stresses are initialised as zero. Pressure is assigned a zero-gradient boundary condition. At the core outlet, all fluid variables are assigned a zero-gradient boundary condition with an exception of pressure, which is set to a value of zero. At the pipe walls, no-slip boundary conditions are imposed on the velocity, linear extrapolation boundary conditions are applied to the polymer-stresses, and a zero-gradient boundary condition is employed for the pressure. A coupled temperature-boundary condition is applied at the interface of the core-fluid and the connecting wall. In the OpenFOAM framework, such a boundary condition is built into the *rheoMultiRegionFoam* solver to ensure continuity of the heat flux across domain interfaces, see [72].

#### Initial and Boundary Conditions for Coupled Simulations—Shell-Fluid

The initial and inlet boundary conditions for the shell region, velocity, temperature, and pressure, are similar to those for the core fluid. At the outlet, the velocity and temperature are assigned zero-gradient boundary conditions while pressure is set to zero. At the walls, no-slip boundary conditions are used for the velocity, while a zero-gradient boundary condition is applied for the pressure. As with the core-fluid and the connecting wall interface, a coupled temperature-boundary condition is employed at the interface of the shell-fluid and the connecting wall.

### Initial and Boundary Conditions for Coupled Simulations—Connecting Wall

The coupled temperature-boundary condition is applied at the interfaces on either side of the connecting wall, i.e., to both the connecting wall/core-fluid interface and the connecting wall/shell-fluid interface.

### Discretisation Schemes for Coupled Simulations—Core-Fluid

The time derivatives are discretised using the implicit Euler scheme. A second-order bounded Gauss linear scheme is used in the discretisation of Laplacian terms. The least squares scheme is applied on the space-gradient terms. The convective terms are discretised via a Universally Bounded Interpolation scheme (Cubista). The solutions of the systems of linear equations for temperature, velocity, and polymer-stresses employ a Preconditioned Bi-Conjugate Gradient (PBiCG) solver in conjunction with a simplified Diagonal Incomplete LU (DILU) pre-conditioner. The pressure equation is solved with a Preconditioned Conjugate Gradient (PCG) solver using Diagonal Incomplete-Cholesky (DIC) pre-conditioners.

### Discretisation Schemes for Coupled Simulations—Shell-Fluid

The implicit Euler scheme is used to discretise time derivatives and a second-order bounded Gauss linear scheme is utilised for space-gradient terms. The Laplacian terms are treated via Gauss linear orthogonal schemes. For convective terms the Cubista and Gauss linear schemes are employed. The solver for the discretised temperature and velocity equations is the PBiCGStab solver with a DILU pre-conditioner. A Geometric-Algebra Multi-Grid (GAMG) solver is used in conjunction with a DIC pre-conditioner for the solution of the pressure equation.

**Discretisation Schemes for Coupled Simulations—Connecting Wall**

The space-gradient terms are discretised using the Gauss linear scheme, while Laplacian terms employ the second-order bounded linear scheme. The time derivatives are treated via the implicit Euler scheme. The temperature equation for the connecting wall is solved using a PCG solver in conjunction with a DIC preconditioner.

## 3.5 Numerical Results and Discussion

### 3.5.1 Mesh Convergence

The mesh independence (or alternatively mesh convergence) in the present simulations is illustrated in Figure 3.3. The mesh sizes in Figure 3.3 correspond to the number of computational cells in Table 3.1.

**Table 3.1:** Mesh sizes corresponding to Figure 3.3.

| | |
|---|---|
| mesh 1 | 120,000 cells |
| mesh 2 | 640,000 cells |
| mesh 3 | 800,000 cells |

Given the huge computational costs incurred in running the simulations with such high numbers of computational cells, it is prudent to balance the requirements of mesh convergence, on the one hand, and computational costs, on the other. Figure 3.3 illustrates mesh independence for the three vastly different mesh sizes. For these reasons, all subsequent simulations in this work are conducted via mesh size

1, i.e., with 120,000 computational cells. It should be remarked that similar mesh independence was observed with much fewer than 120,000 computational cells.

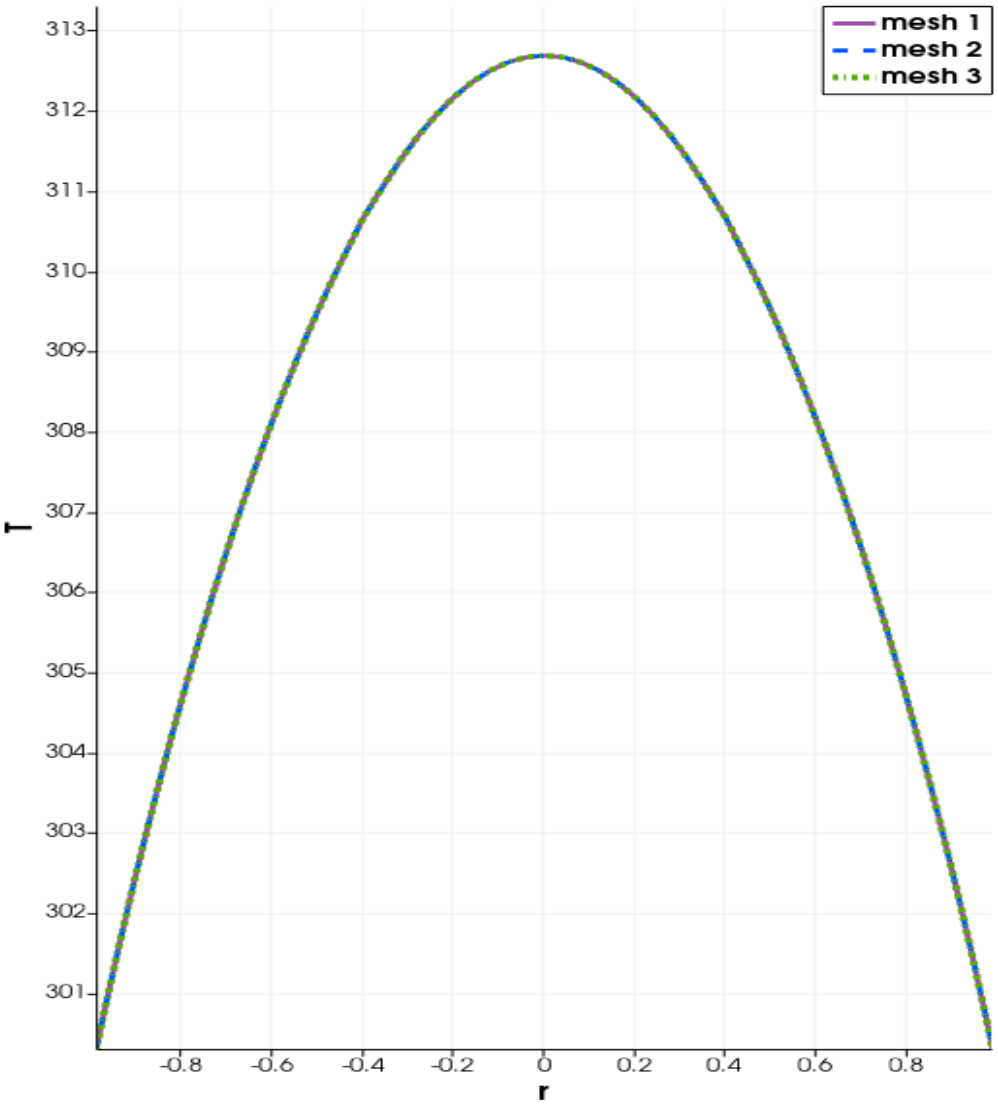


**Figure 3.3:** Illustration of mesh independence.

### 3.5.2 Dimensionless Parameters

As detailed in [86], it is desirable to report the results with respect to dimensionless parameters. This allows the results to be translated more generally to pipes/geometries

of arbitrary size and also to general flow conditions. Results that are based on specific geometric dimensions and specific flow conditions would otherwise be case-specific and not easily generalisable. The relevant dimensionless parameters for the core region are, respectively, the Reynolds number ($Re_c$), the Prandtl number ($Pr_c$), the Deborah number ($De$), the ratio of polymer to total viscosity ($\beta$), and the Giesekus nonlinear parameter ($\varepsilon$):

$$Re_c = \frac{\rho_c^* U_{c_0}^* L^*}{\eta_c^*},\ Pr_c = \frac{C_{p_c}^* \eta_c^*}{K_c^*},\ De = \frac{\lambda^* U_{c_0}^*}{L^*},\ \beta = \frac{\eta_p^*}{\eta_c^*},\ \varepsilon = \frac{L^*}{\eta_c^* \mu_c^* U_{c_0}^*}\alpha^*,$$

where $U_{c_0}^*$ is a reference flow velocity in the core region, say, the constant core-fluid velocity at the inlet. The relevant dimensionless parameters for the shell region are, respectively, the Reynolds and Prandtl numbers, as well as the ratio of nano-particle to base-fluid thermal conductivities:

$$Re_s = \frac{\rho_s^* U_{s_0}^* L^*}{\eta_s^*},\ Pr_s = \frac{C_{p_s}^* \eta_s^*}{K_f^*},\ \kappa = \frac{K_s^*}{K_f^*},$$

where $U_{s_0}^*$ is a reference flow velocity in the shell region, say, the constant shell-fluid velocity at the inlet.

Unless otherwise indicated, the subsequent simulations are carried using the following parameter values:

| | |
|---|---|
| core-fluid: | $Re_c = 0.6,\ Pr_c = 0.8,\ De = 0.4,\ \varepsilon = 0.2,\ \beta = 0.5,$ |
| shell-fluid: | $Re_s = 90,\ Pr_s = 3,$ |
| thermal-conductivity: | $\kappa = 654.16,\ \aleph = 3,\ \alpha = 0.2,\ A_2 = 0.5,\ \varphi = 0.2.$ |

The thermal conductivity ratio, $\kappa$, is calculated from the values, $K_s = 401$ $\mathrm{Wm^{-1}K^{-1}}$ and $K_f = 0.613$ W/(m·K). In the subsequent graphical results, if any of the above

parameters are varied, it is understood that the other parameters will be kept at the given values.

### 3.5.3 Numerical Validation

The absence of nano-particles ($\kappa = \aleph = A_2 = \varphi = 0$) reduces the present investigation to that in [86]. Simulations with $\kappa = \aleph = A_2 = \varphi = 0$ give the same results as in [86].

### 3.5.4 Response of Flow Variables to Variations in Nano-particle Volume-Fraction

Figures 3.4–3.10 demonstrate the effects of varying the nano-particle volume-fraction, $\varphi$, on the flow variables, respectively, the velocity, temperature, pressure, diagonal polymer stress components, and the normal stress differences. The first and second normal-stress differences, $N_1$ and $N_2$, are, respectively, defined as:

$$N_1 = \tau_{zz} - \tau_{rr} \quad \text{and} \quad N_2 = \tau_{rr} - \tau_{\theta\theta} = \tau_{rr},$$

where the final equality in the second normal stress difference, $N_2$, results from axi-symmetry assumptions, $\tau_{\theta\theta} = 0$. The first normal-stress difference remains non-negative, $N_1 \geq 0$, as required.

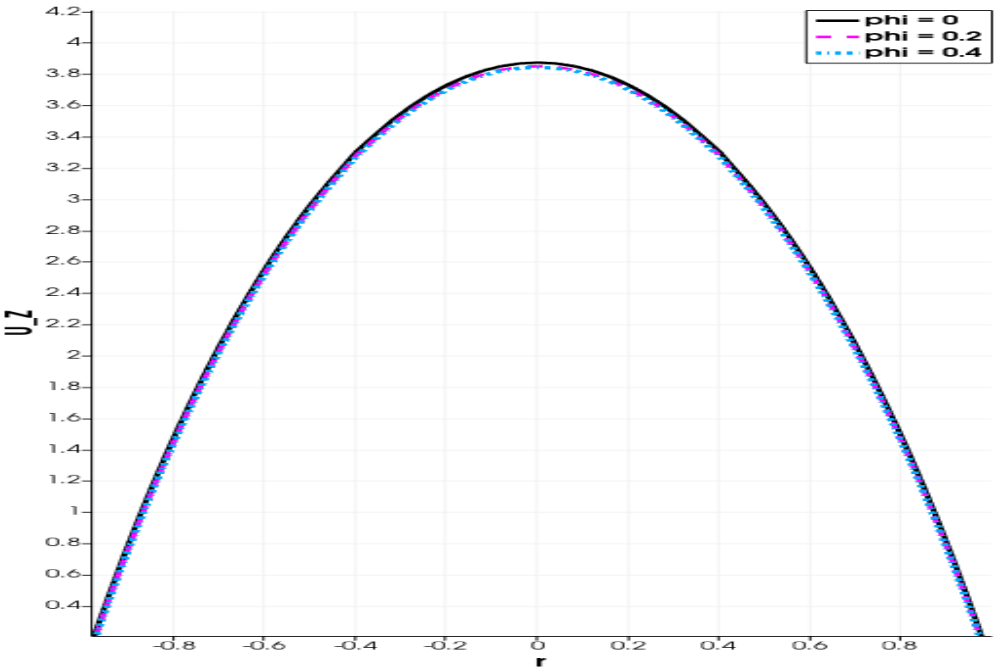


**Figure 3.4:** Effects of nano-particle volume-fraction, $\varphi$, on the core-fluid velocity.

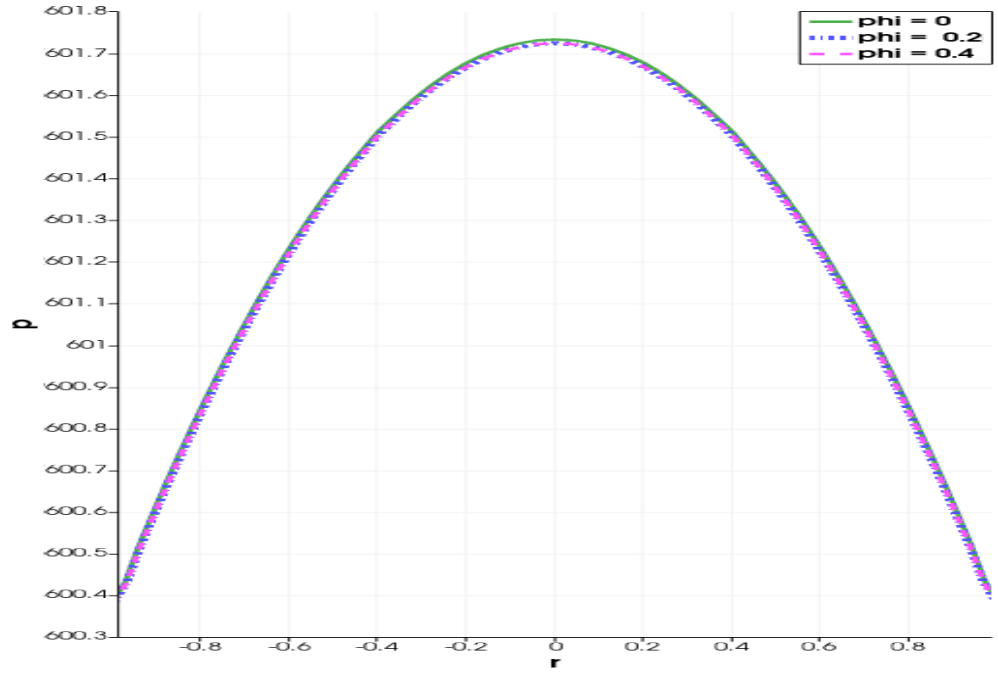


**Figure 3.5:** Effects of nano-particle volume-fraction, $\varphi$, on the core-fluid pressure.

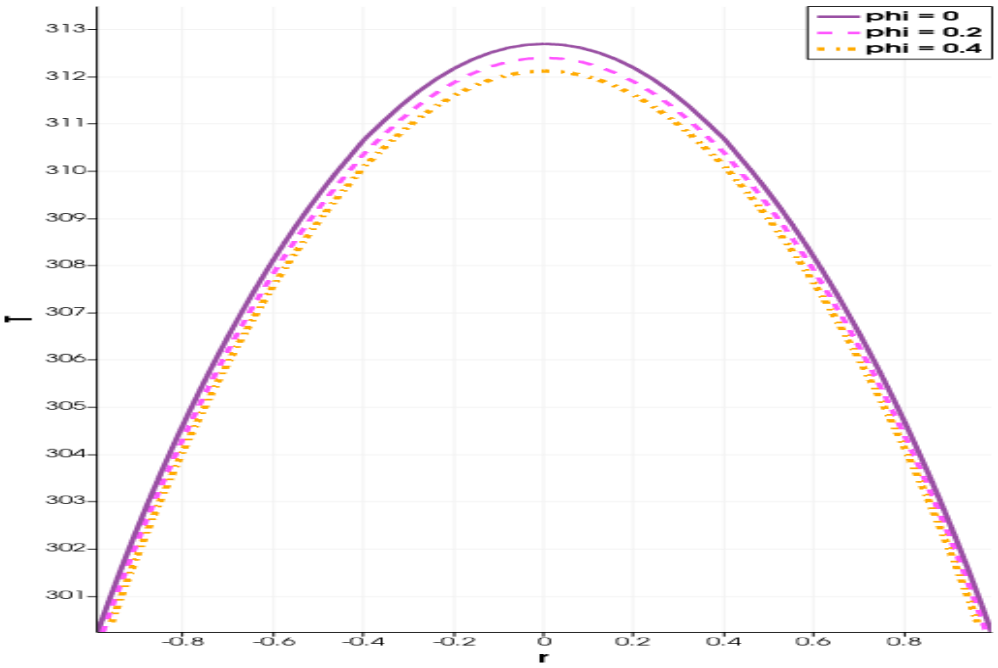


**Figure 3.6:** Effects of nano-particle volume-fraction, $\varphi$, on the core-fluid temperature.

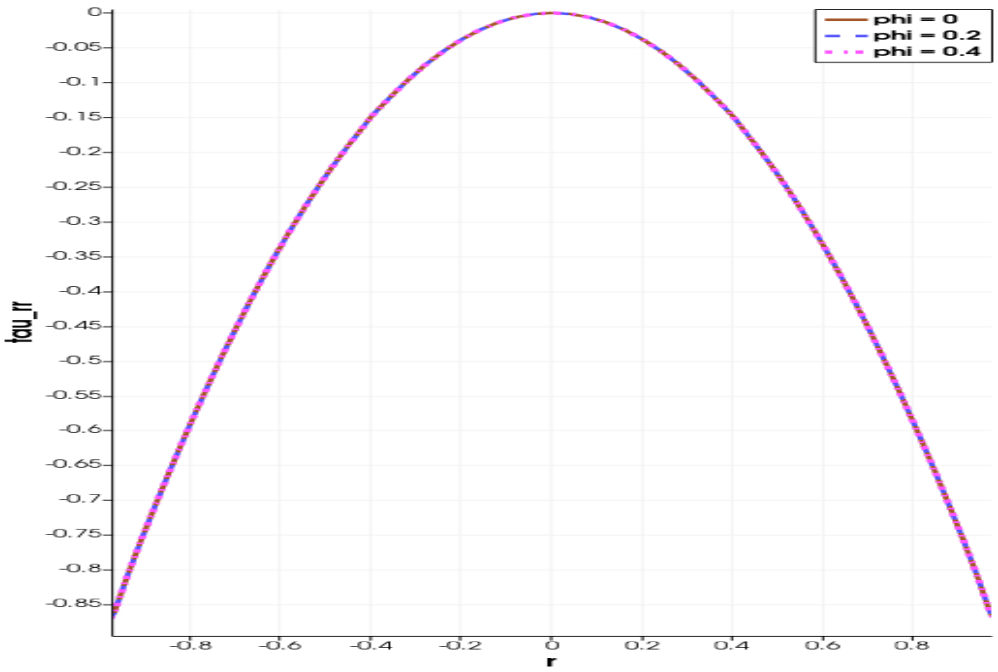


**Figure 3.7:** Effects of nano-particle volume-fraction, $\varphi$, on the diagonal stress component, $\tau_{rr}$.

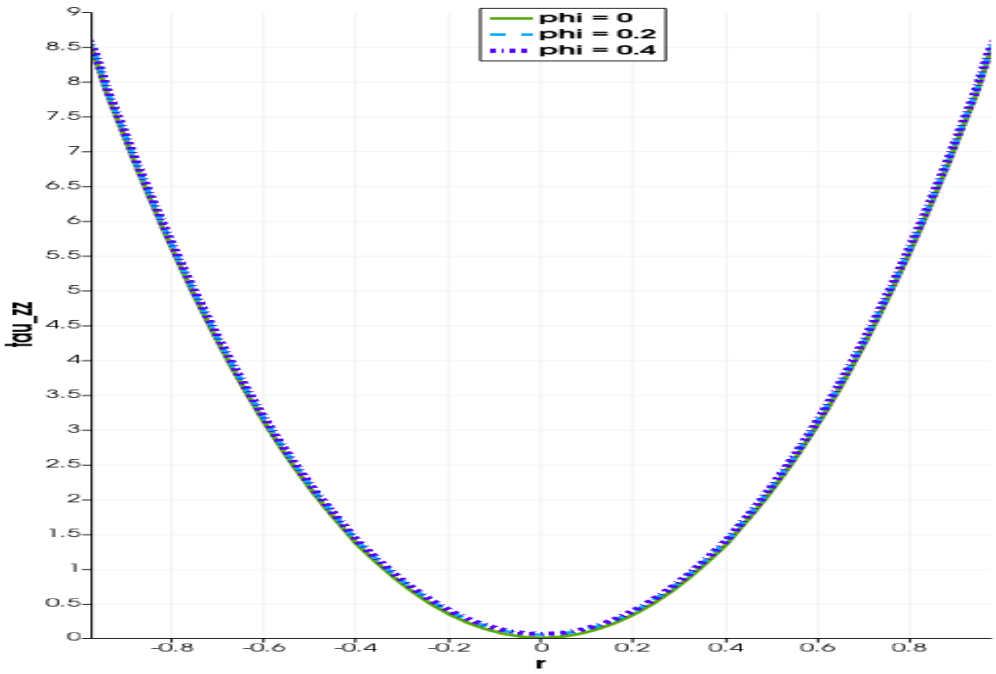


**Figure 3.8:** Effects of nano-particle volume-fraction, $\varphi$, on the diagonal stress component, $\tau_{zz}$.

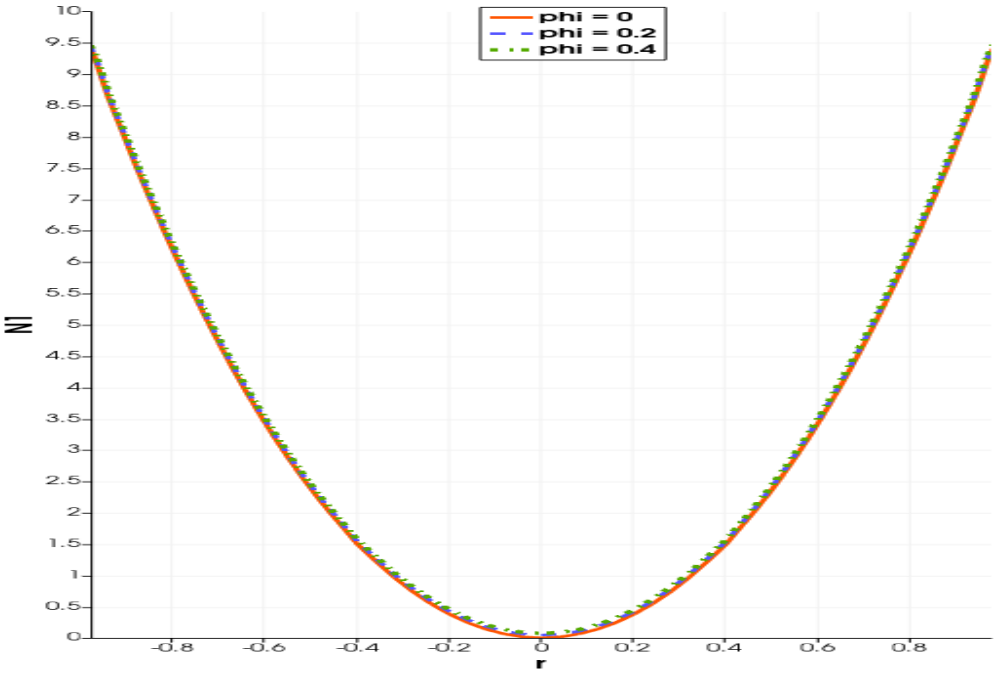


**Figure 3.9:** Effects of nano-particle volume-fraction, $\varphi$, on the first normal stress difference, $N_1$.

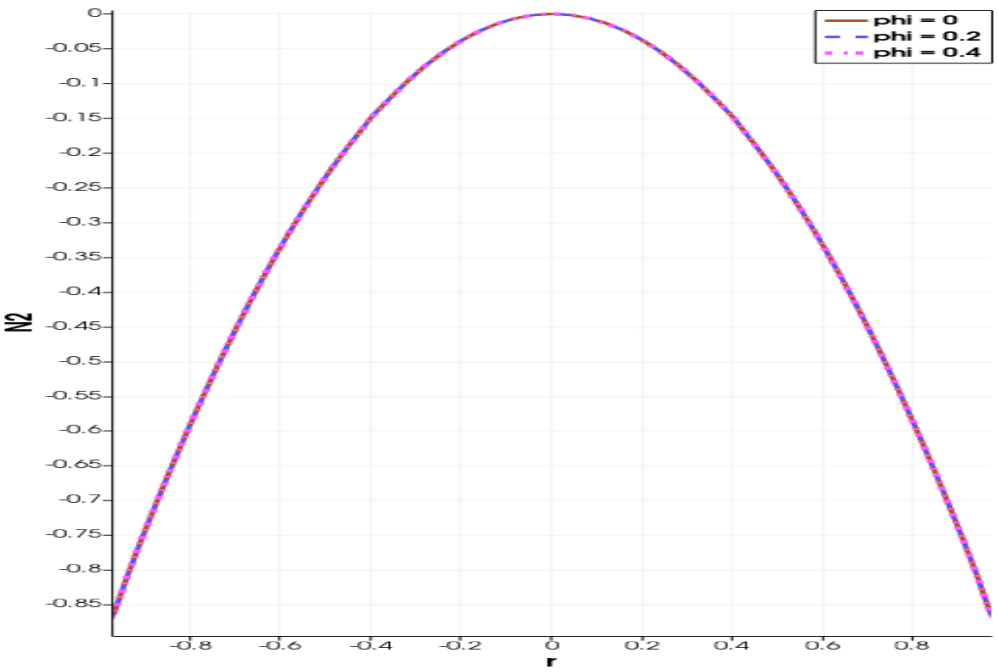


**Figure 3.10:** Effects of nano-particle volume-fraction, $\varphi$, on the second normal stress difference, $N_2$.

The results illustrated in Figures 3.4–3.10 give the expected parabolic profiles. Of particular note are the important effects of the nano-particles volume-fraction, $\varphi$, on the core-fluid temperature, as shown in Figure 3.6. The core-fluid temperature decreases as $\varphi$ increases. This clearly indicates that increases in the nano-particles volume-fraction, $\varphi$, increase the heat-transfer-rates from the hot core-fluid to the colder shell-nanofluid. Specifically, increases in the nano-particles volume-fraction, $\varphi$, increase the thermal conductivity of the shell-nanofluid, enhancing its coolant characteristics.

Figures 3.11–3.16 demonstrate the effects of varying the Prandtl number on the core-fluid flow field variables.

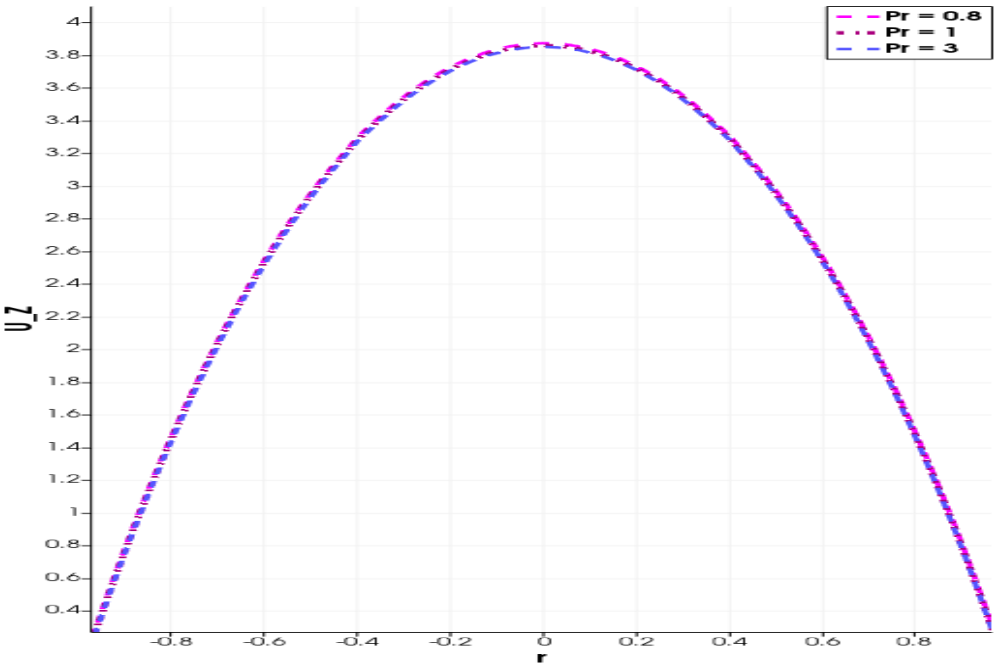


**Figure 3.11:** Effects of Prandtl number, $Pr$, on the core-fluid velocity.

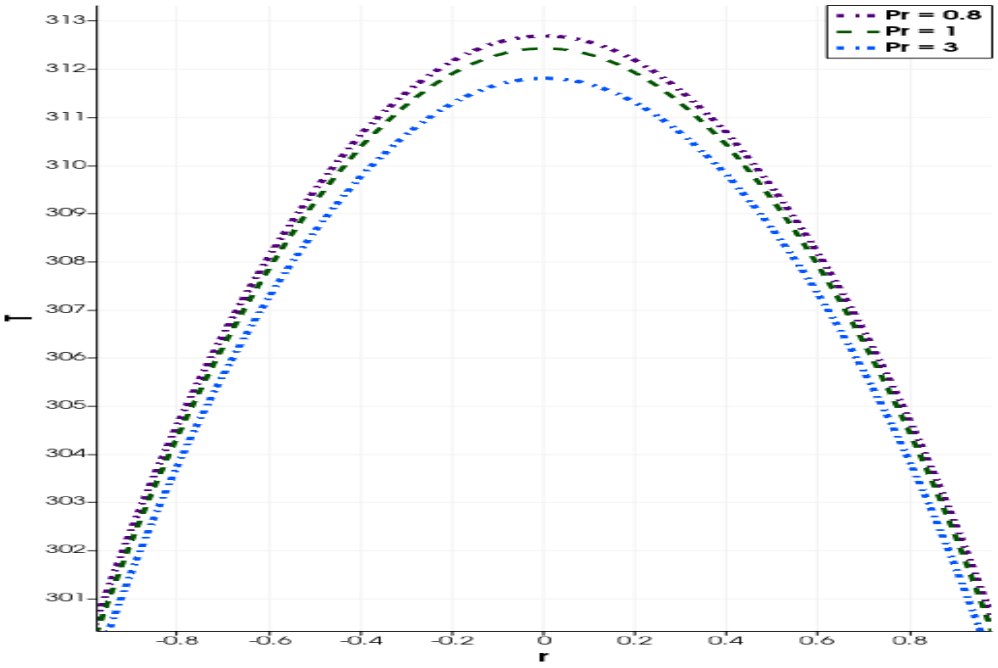


**Figure 3.12:** Effects of Prandtl number, $Pr$, on the core-fluid temperature.

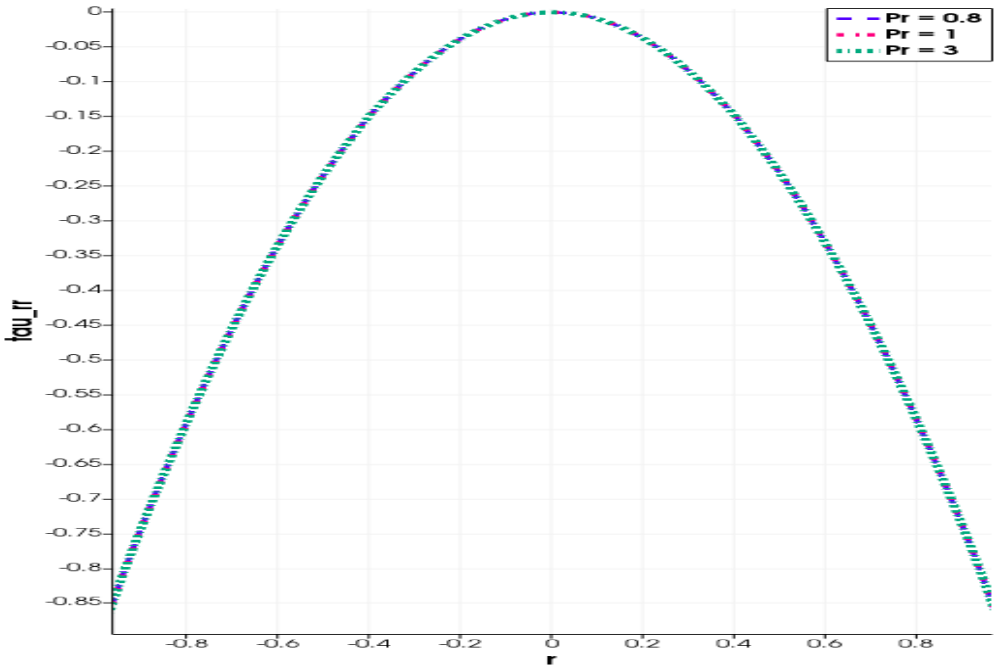


**Figure 3.13:** Effects of Prandtl number, $Pr$, on the diagonal stress component, $\tau_{rr}$.

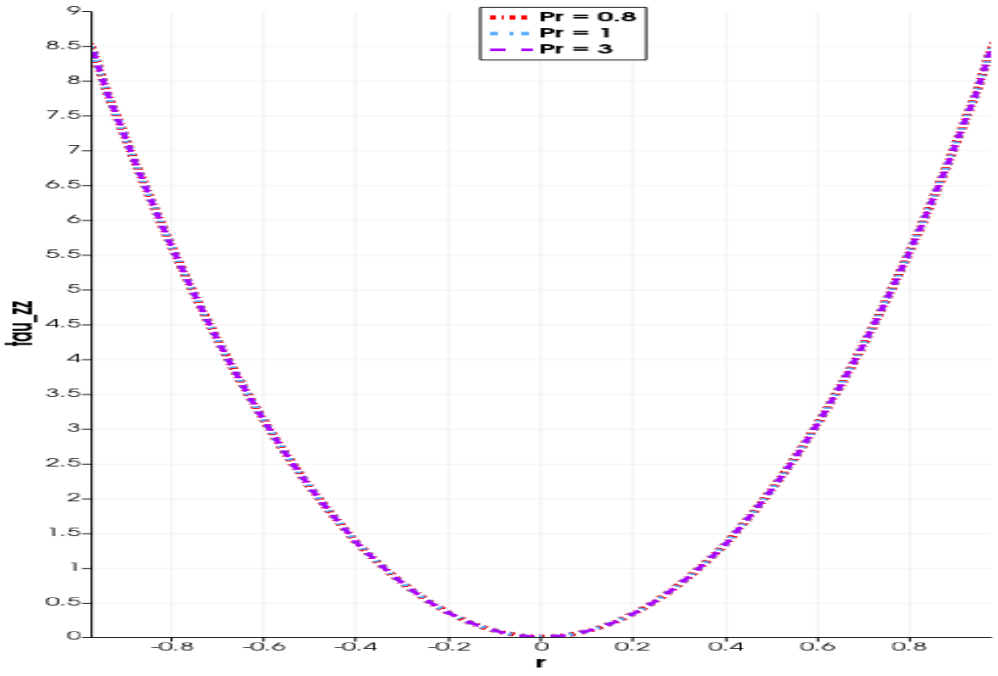


**Figure 3.14:** Effects of Prandtl number, $Pr$, on the diagonal stress component, $\tau_{zz}$.

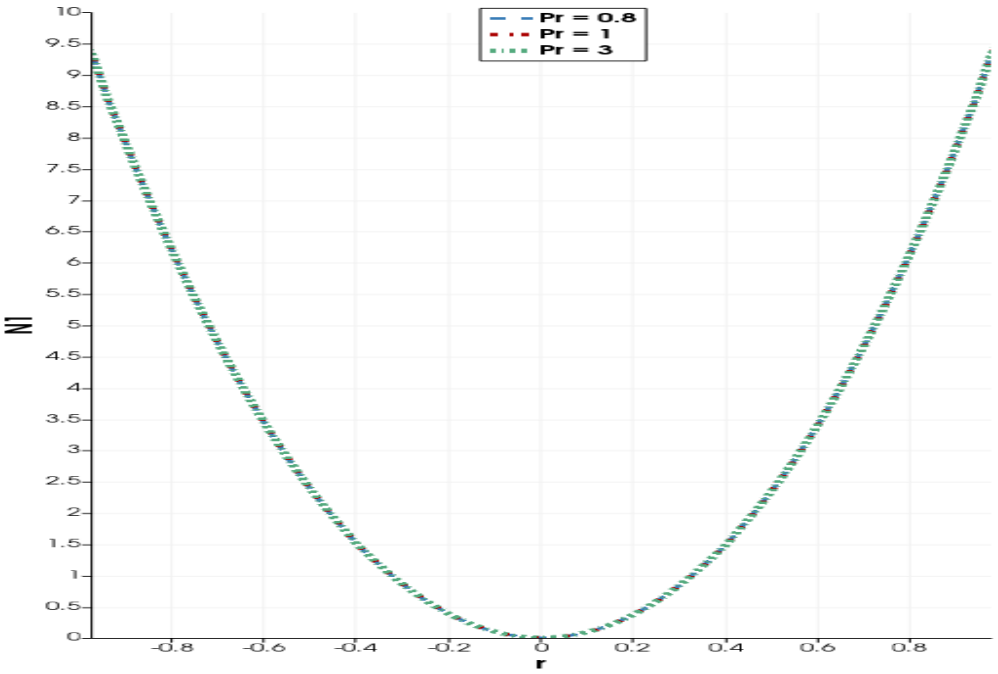


**Figure 3.15:** Effects of Prandtl number, $Pr$, on the first normal stress difference, $N_1$.

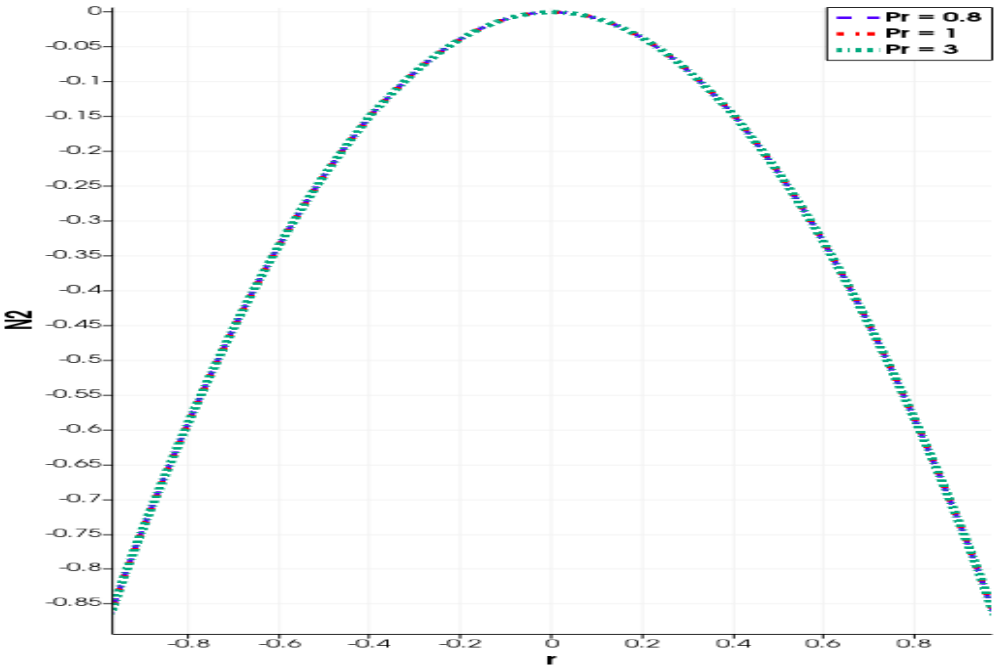


**Figure 3.16:** Effects of Prandtl number, $Pr$, on the second normal stress difference, $N_2$.

The results illustrated in Figures 3.11–3.16 similarly give the expected parabolic profiles. Of particular note are the expected effects of the Prandtl number on the core-fluid temperature, as shown in Figure 3.12. The core-fluid temperature decreases as the Prandtl number increases. This is a consequence of the fact that the Prandtl number acts to dampen the strengths of the heat conduction and the heat sources.

Figures 3.17–3.22 demonstrate the effects of varying the Reynolds number on the core-fluid flow field variables.

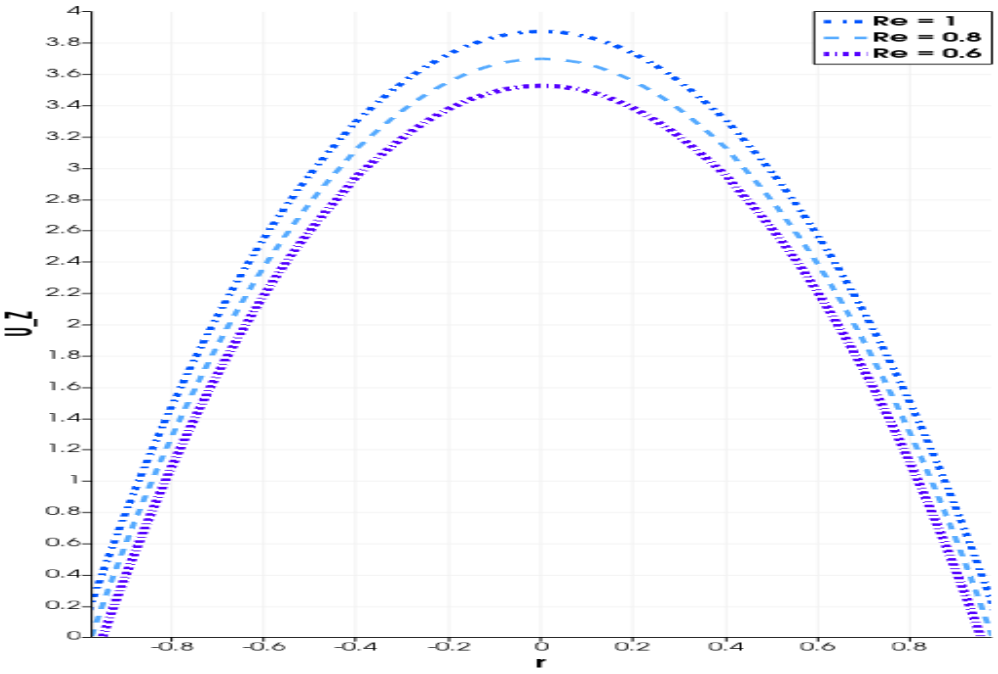


**Figure 3.17:** Effects of Reynolds number, $Re$, on the core-fluid velocity.

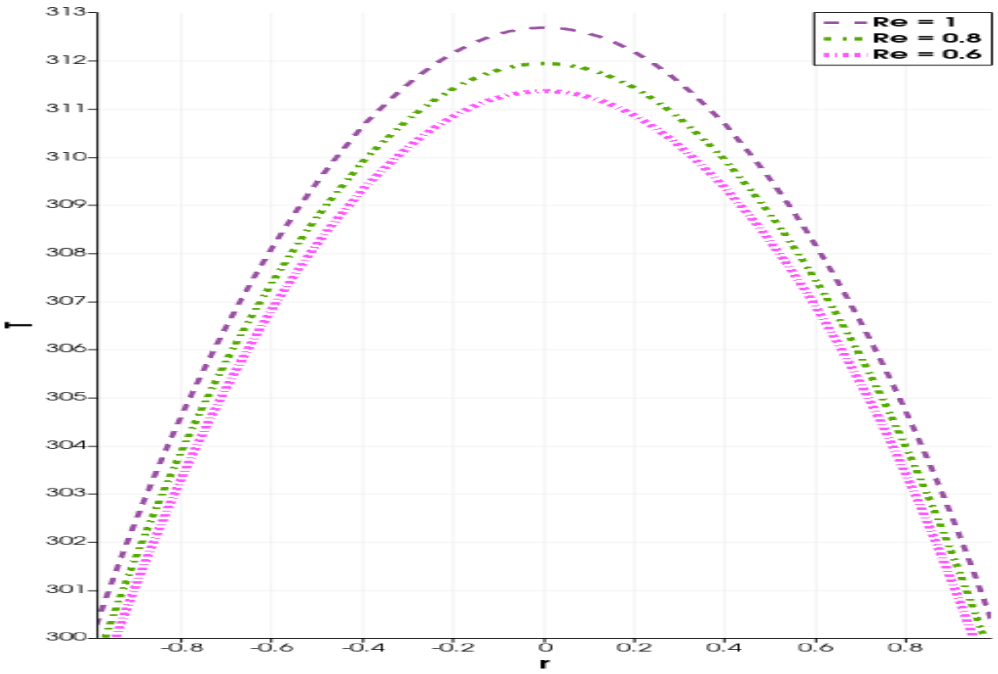


**Figure 3.18:** Effects of Reynolds number, $Re$, on the core-fluid temperature.

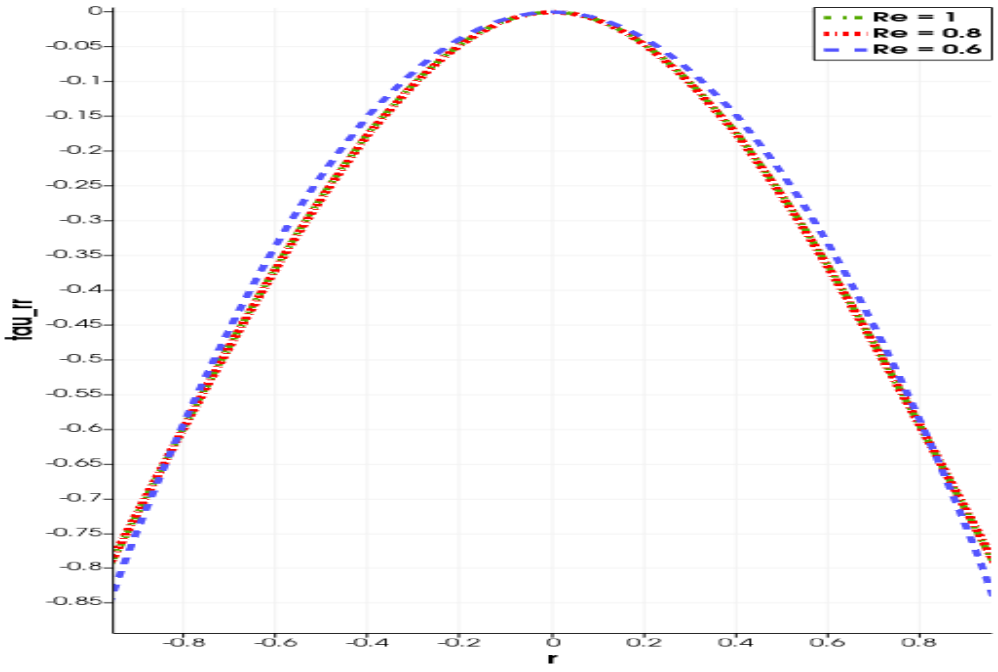


**Figure 3.19:** Effects of Reynolds number, $Re$, on the diagonal stress component, $\tau_{rr}$.

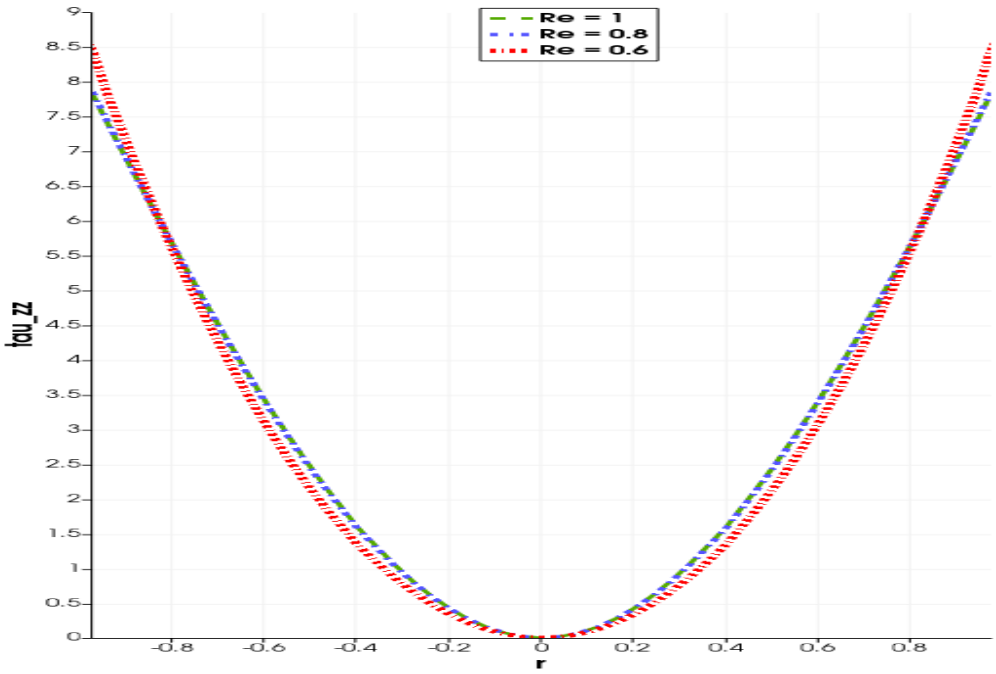


**Figure 3.20:** Effects of Reynolds number, $Re$, on the diagonal stress component, $\tau_{zz}$.

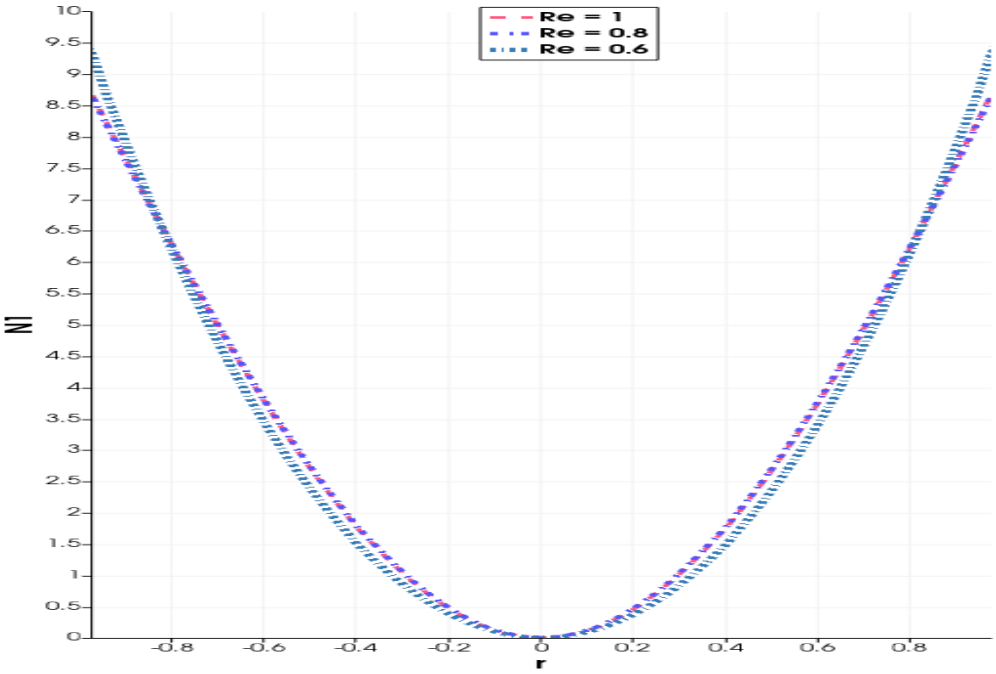


**Figure 3.21:** Effects of Reynolds number, $Re$, on the first normal stress difference, $N_1$.

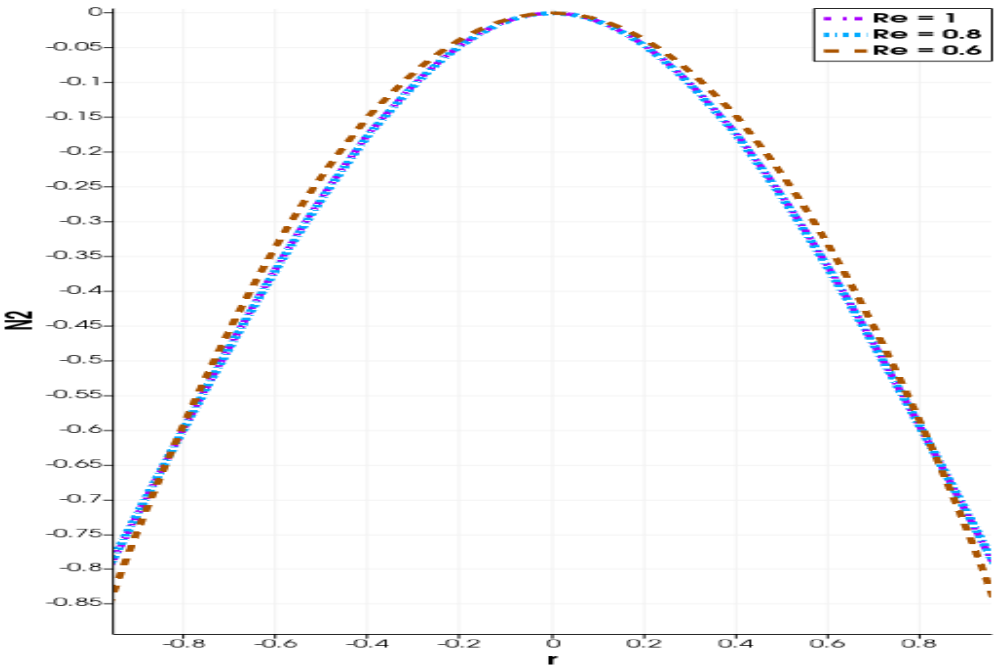


**Figure 3.22:** Effects of Reynolds number, $Re$, on the second normal stress difference, $N_2$.

The results illustrated in Figures 3.11–3.16 again give the expected parabolic profiles. Of particular note are the expected effects of the Reynolds number on the core-fluid velocity, as shown in Figure 3.17. The core-fluid velocity increases as the Reynolds number increases. This follows naturally from the observation that the Reynolds number is directly proportional to the inlet velocity and is also inversely proportional to the fluid viscosity. An increase in the inlet velocity and/or a decrease in the fluid viscosity would act to increase the core-fluid Reynolds number. We also notice from Figure 3.18 that the core-fluid temperature increases with an increasing Reynolds number.

Figures 3.23–3.28 demonstrate the effects of varying the Deborah number on the core-fluid flow field variables.

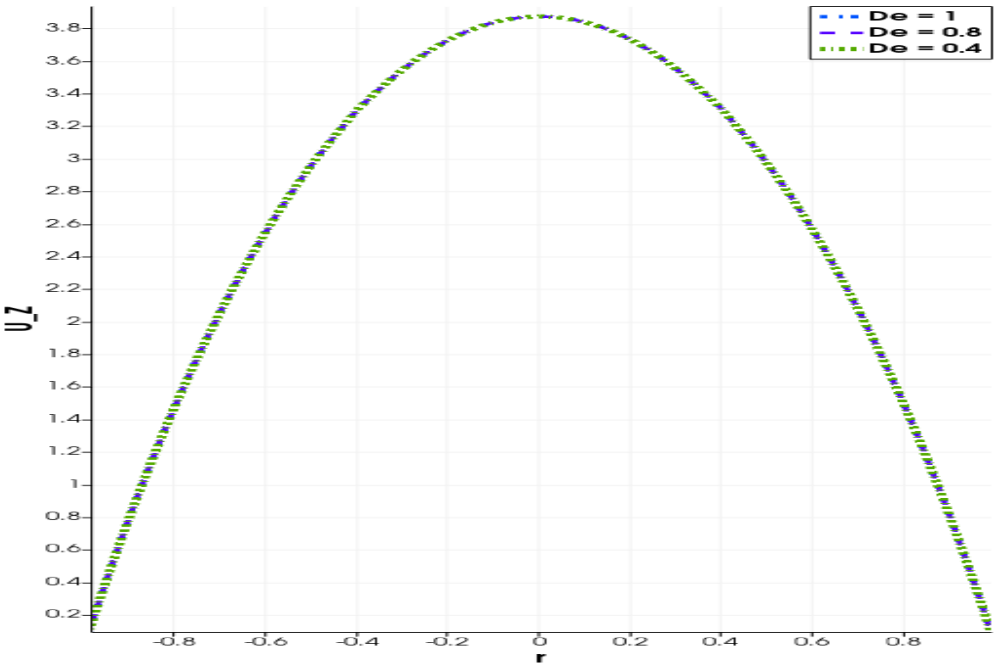


**Figure 3.23:** Effects of Deborah number, $De$, on the core-fluid velocity.

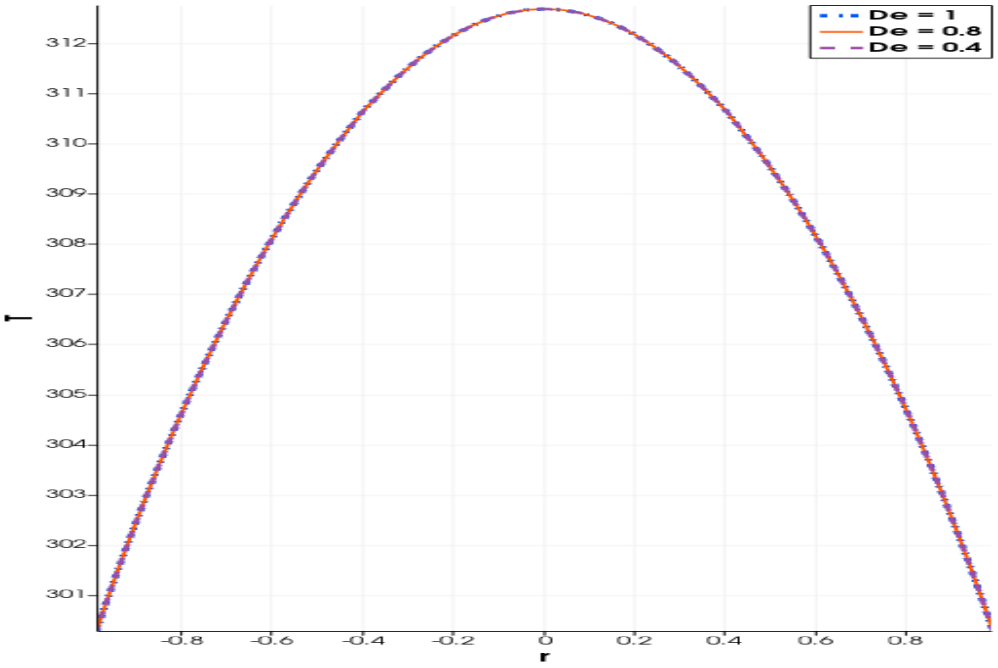


**Figure 3.24:** Effects of Deborah number, $De$, on the core-fluid temperature

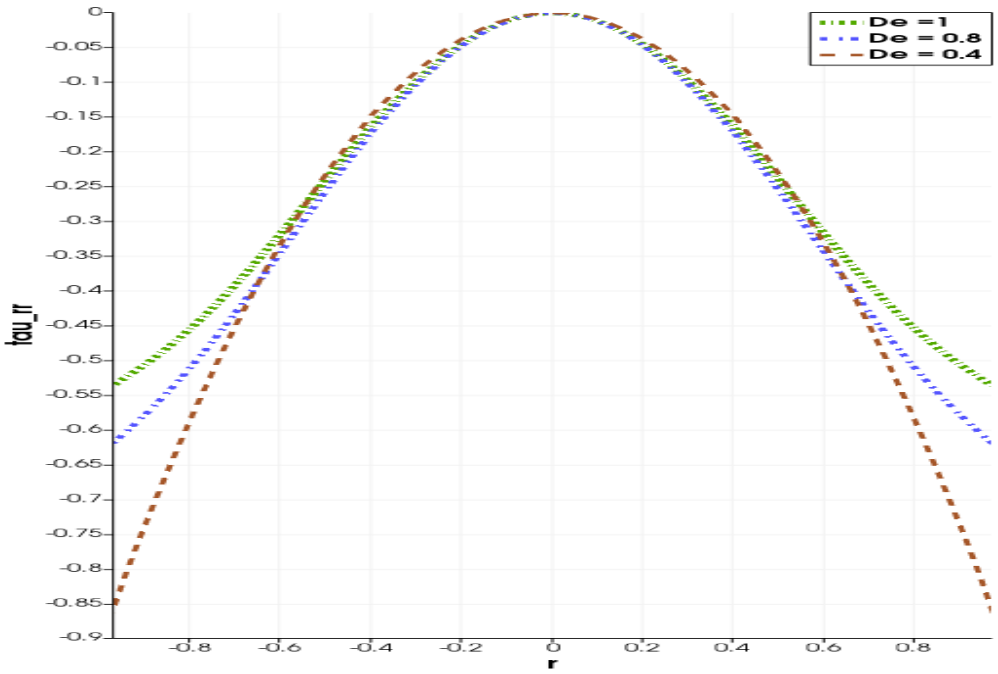


**Figure 3.25:** Effects of Deborah number, $De$, on the diagonal stress component, $\tau_{rr}$.

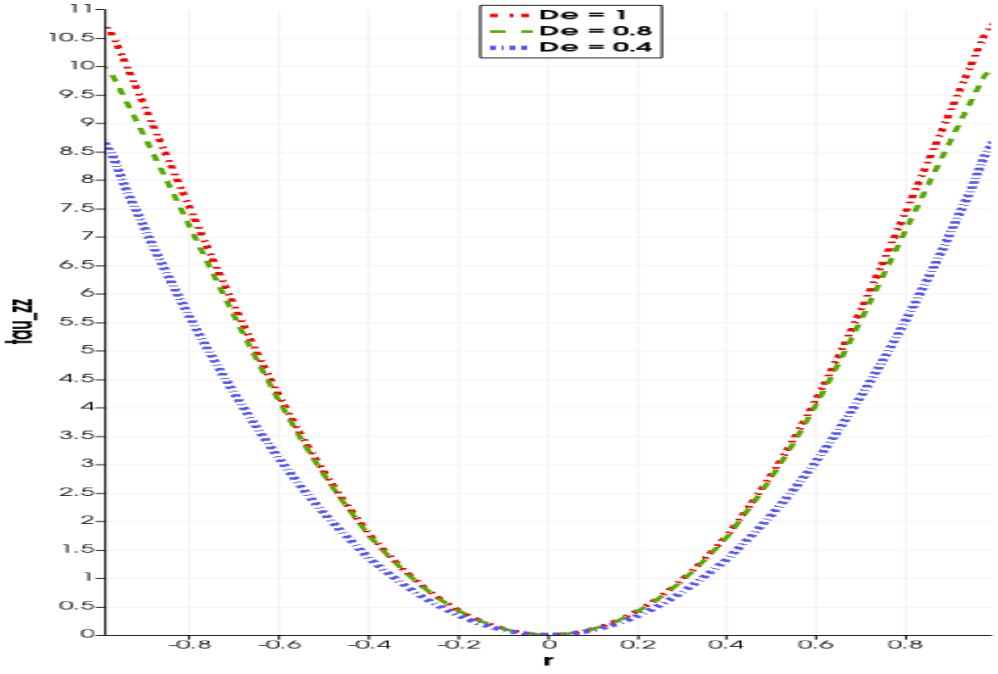


**Figure 3.26:** Effects of Deborah number, $De$, on the diagonal stress component, $\tau_{zz}$.

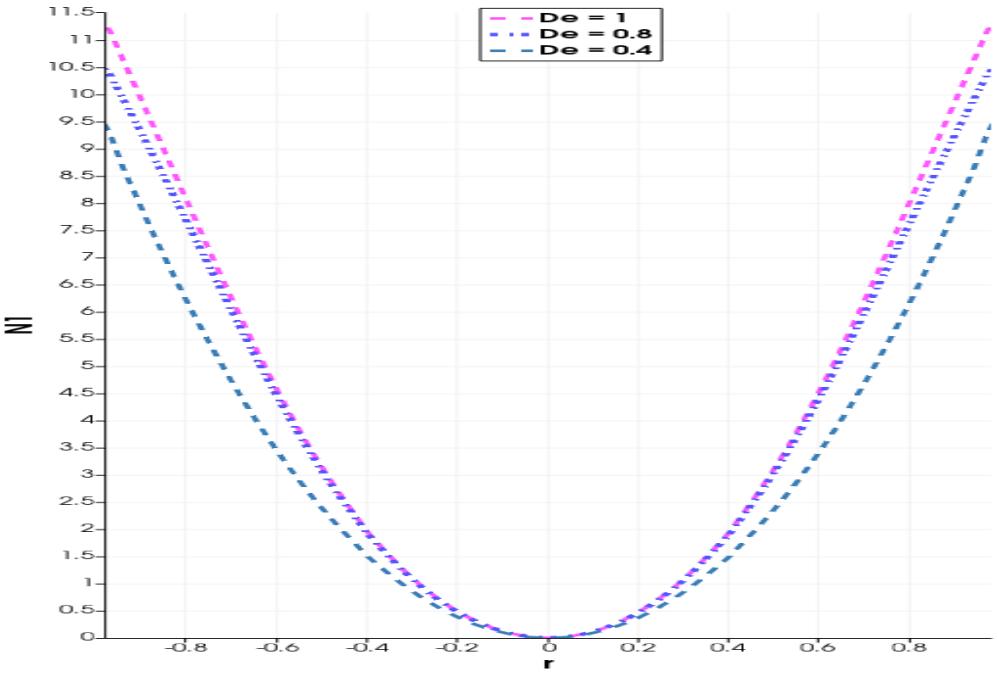


**Figure 3.27:** Effects of Deborah number, $De$, on the first normal stress difference, $N_1$.

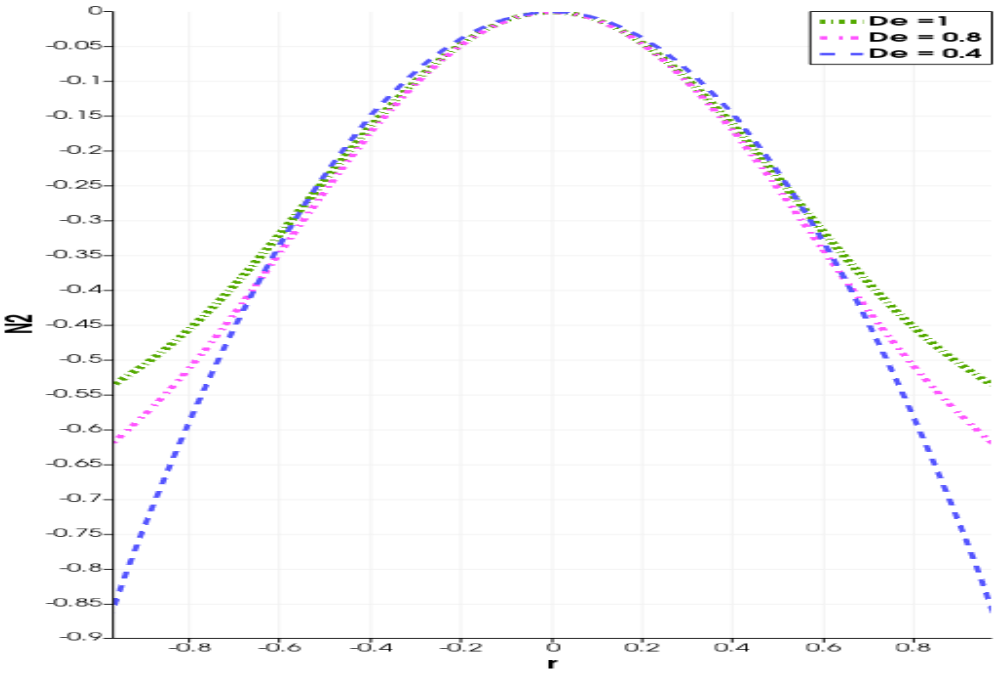


**Figure 3.28:** Effects of Deborah number, $De$, on the second normal stress difference, $N_2$.

As can be observed from Figures 3.25–3.28, an increase in the Deborah number increases the elastic effects in the core-fluid. The results illustrated in, say, Figures 3.25 and 3.27, demonstrate that the elastic effects are more pronounced closer to the inner pipe walls and away from the pipe centerline.

### 3.5.5 Response of Flow Variables in the Longitudinal Direction

All the graphical results thus far are presented in the radial direction, across the inner pipe diameter. For this reason, the results have been symmetric about the pipe centerline. It is important to also illustrate the development of the solutions in the longitudinal direction (i.e., the flow direction) in response to variations in flow parameters.

Figure 3.29 illustrates the behaviour of the core-fluid temperature in the longitudinal direction, in response to variations in the nano-particle volume-fraction, $\varphi$.

The results of Figure 3.29 show, as expected, that the core-fluid temperature decreases from the initial high values at the inlet to lower values at the outlet. This is the hallmark of a heat exchanger design and function—that a hot fluid is cooled as it flows and interacts with a colder fluid in a connected channel even when the two connected channels containing the hot and cold fluids, respectively, are separated by a solid wall.

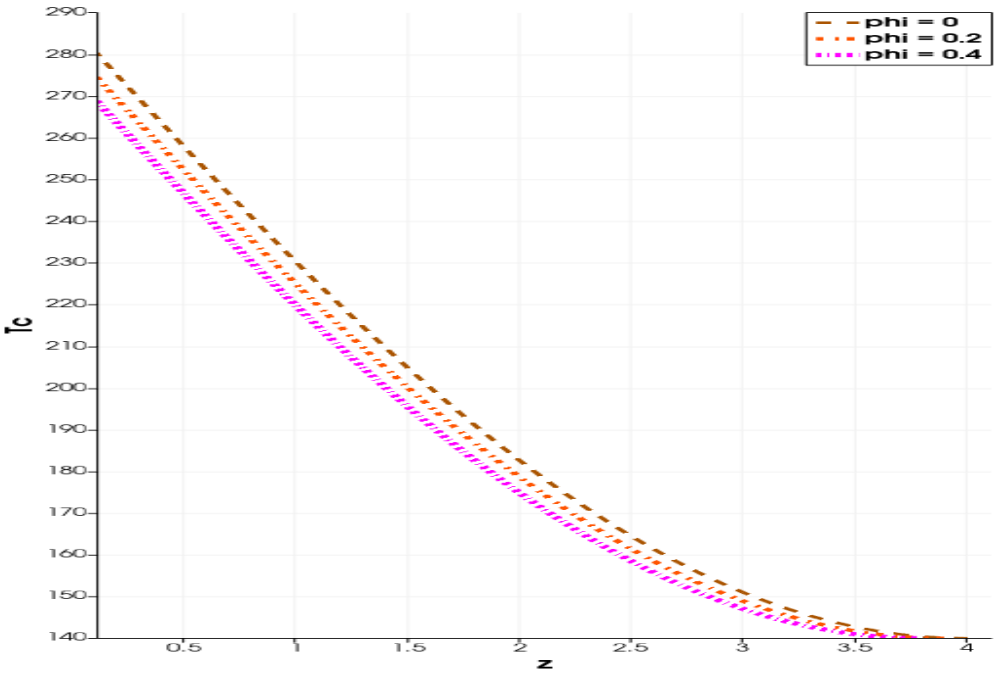


**Figure 3.29:** Effects of nano-particles volume-fraction $\varphi$ on the core-fluid temperature. Fluid moving from inlet at $z = 0$ to outlet at $z = 4$, i.e., flow direction is from left to right ($\longrightarrow$).

Additionally, Figure 3.29 illustrates, as also shown in the corresponding Figure 3.6, that the core fluid temperature decreases with increasing nano-particle volume-fraction, $\varphi$. As already explained under Figure 3.6, this clearly indicates that an increase in the nano-particles volume-fraction, $\varphi$, correspondingly increases the thermal conductivity of the shell-nanofluid, and hence, also increases the heat-exchange characteristics from the hot core-fluid to the colder shell-nanofluid.

Figure 3.30 illustrates the behaviour of the shell-fluid temperature in the longitudinal direction, in response to variations in the nano-particle volume-fraction, $\varphi$.

The results of Figure 3.30 show, as expected, that the shell-fluid temperature will increase from the initial low values at the inlet to higher values at the outlet. This is again the hallmark of a heat exchanger design and function—that a coolant fluid is heated as it flows and interacts with a hotter fluid in a connected channel even when

the two connected channels, respectively, containing the coolant and hot fluids, are separated by a solid wall.

Figure 3.31 illustrates the behaviour of the connecting wall temperature in the longitudinal direction, in response to variations in the nano-particle volume-fraction, $\varphi$. The connecting wall temperature would roughly average the core-fluid and shell-fluid temperatures, and hence, the behaviour of the connecting wall temperature largely mirrors the average behavior of the core-fluid and shell-fluid temperatures. Of specific note is that the connecting wall temperature decreases with increasing nano-particle volume-fraction, $\varphi$.

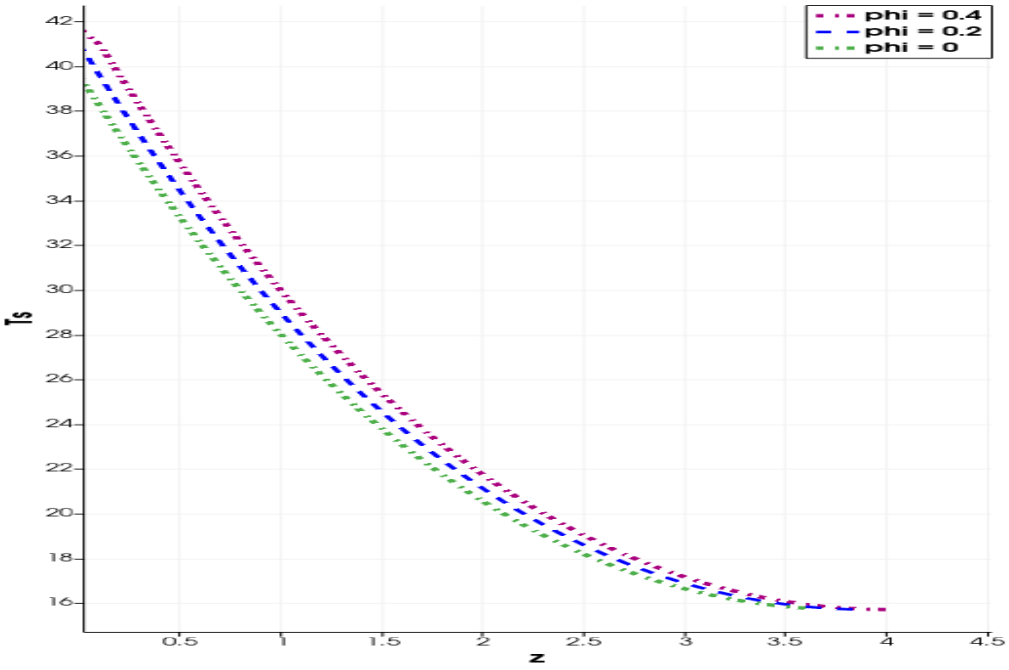


**Figure 3.30:** Effects of nano-particles volume-fraction $\varphi$ on shell-fluid temperature. Fluid moving from inlet at $z = 4$ to outlet at $z = 0$, i.e., flow direction is from right to left ($\longleftarrow$).

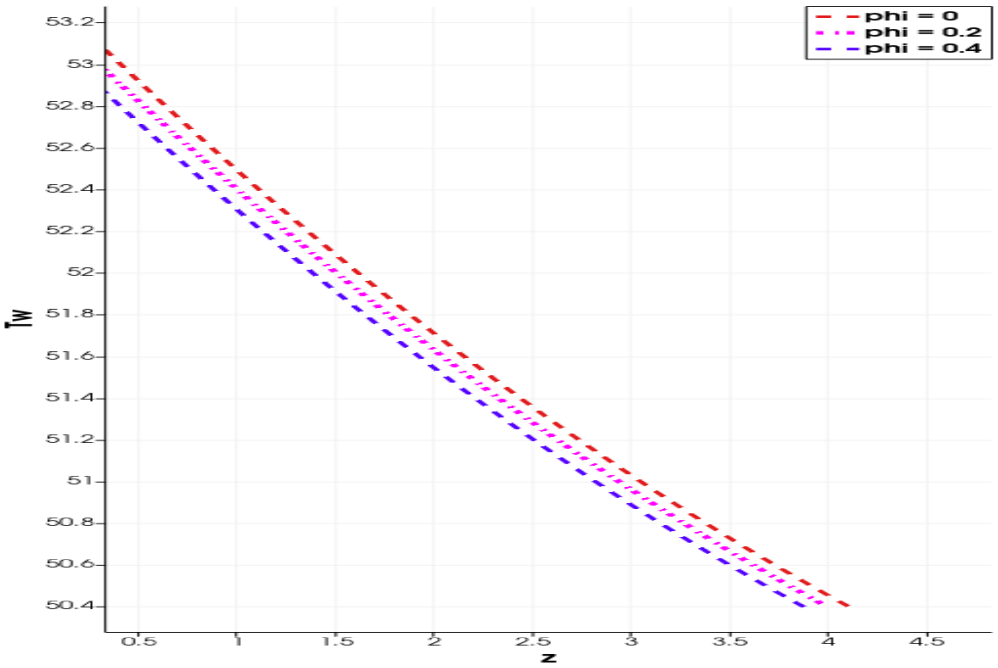


**Figure 3.31:** Effects of nano-particles volume-fraction, $\varphi$, on the connecting wall temperature.

Figures 3.32 and 3.33, respectively, illustrate the behaviour of the core-fluid temperature and the shell-fluid temperature, in the longitudinal direction, in response to variations in the Prandtl number, $Pr$. The results are similarly explained as those in Figure 3.12.

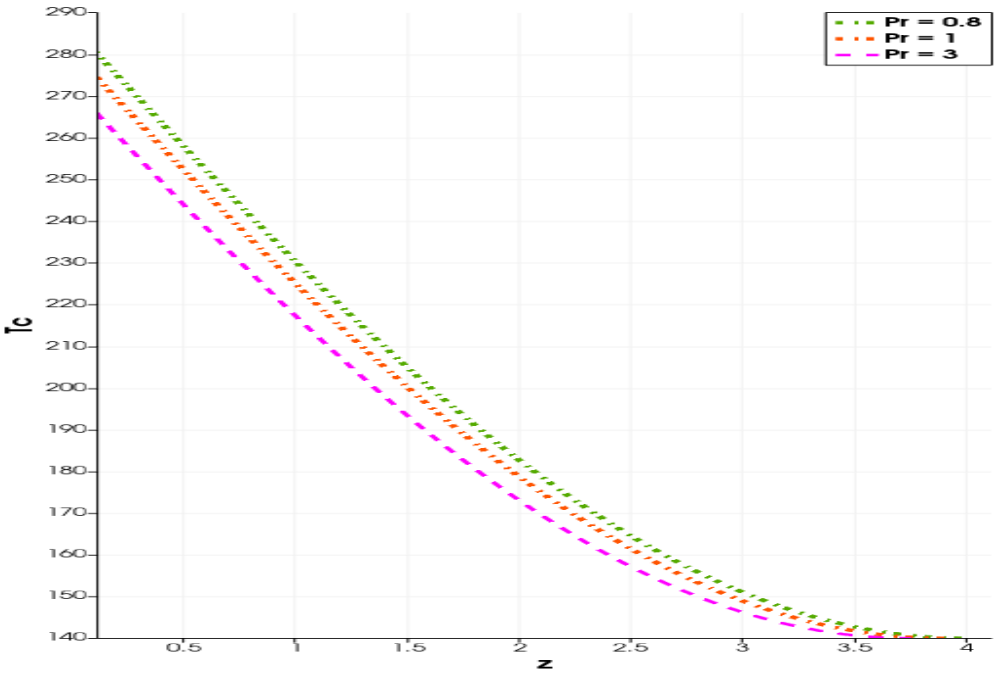


**Figure 3.32:** Effects of Prandtl number, $Pr$, on core-fluid temperature. Fluid moving from inlet at $z = 0$ to outlet at $z = 4$, i.e., flow direction is from left to right ($\longrightarrow$).

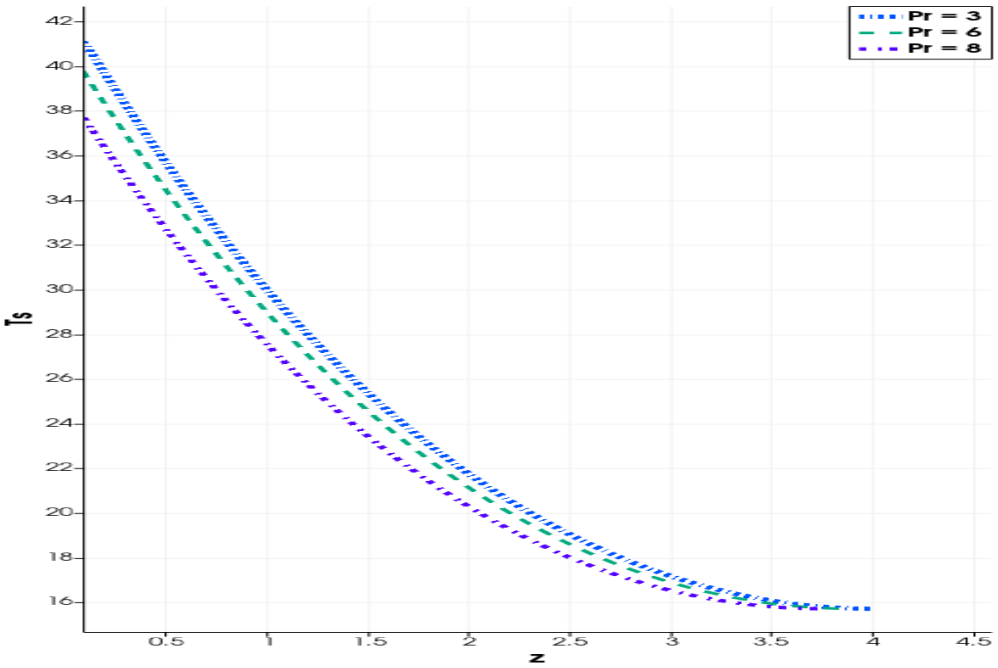


**Figure 3.33:** Effects of Prandtl number, $Pr$, on shell-fluid temperature. Fluid moving from inlet at $z = 4$ to outlet at $z = 0$, i.e., flow direction is from right to left ($\longleftarrow$).

Figures 3.34 and 3.35, respectively, illustrate the behaviour of the core-fluid temperature and the shell-fluid temperature, in the longitudinal direction, in response to variations in the Reynolds number, $Re$. The results are similarly explained as those in Figure 3.18.

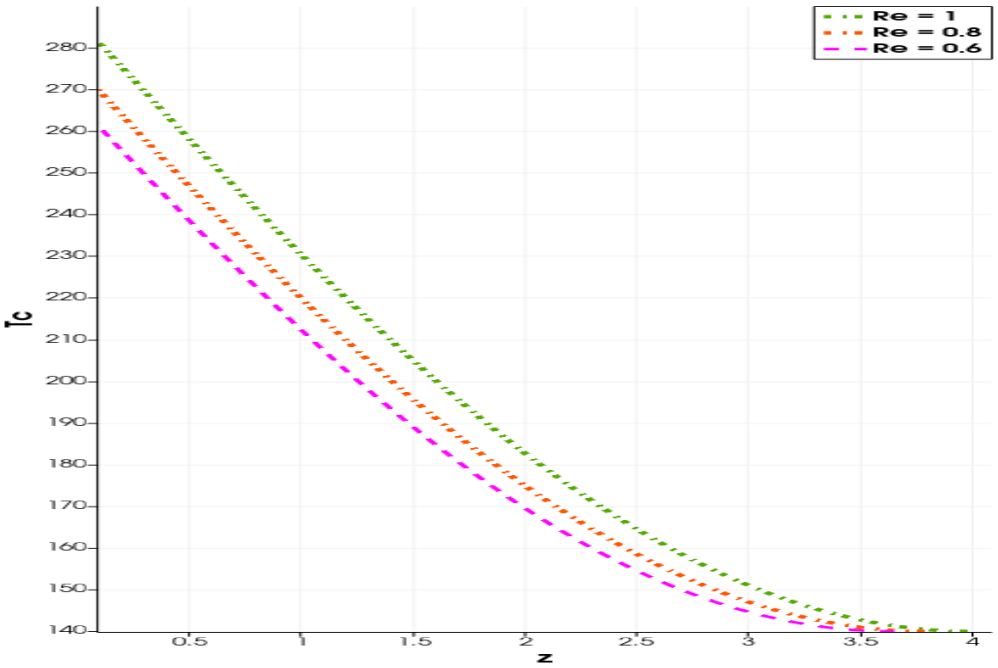


**Figure 3.34:** Effects of Reynolds number, $Re$, on core-fluid temperature. Fluid moving from inlet at $z = 0$ to outlet at $z = 4$, i.e., flow direction is from left to right ($\longrightarrow$).

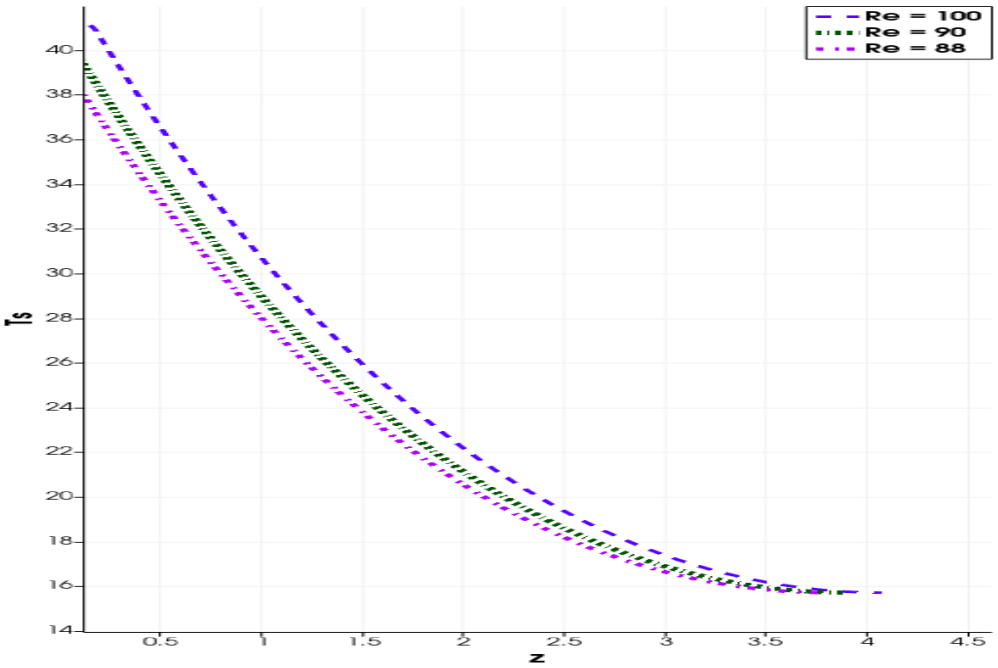


**Figure 3.35:** Effects of Reynolds number, $Re$, on the shell-fluid temperature. Fluid moving from inlet at $z = 4$ to outlet at $z = 0$, i.e., flow direction is from right to left ($\longleftarrow$).

Figure 3.36 illustrates the behaviour of the core-fluid temperature, in the longitudinal direction, in response to variations in the Reynolds number, $Re$. The results are similarly to those in Figure 3.24 for the radial direction.

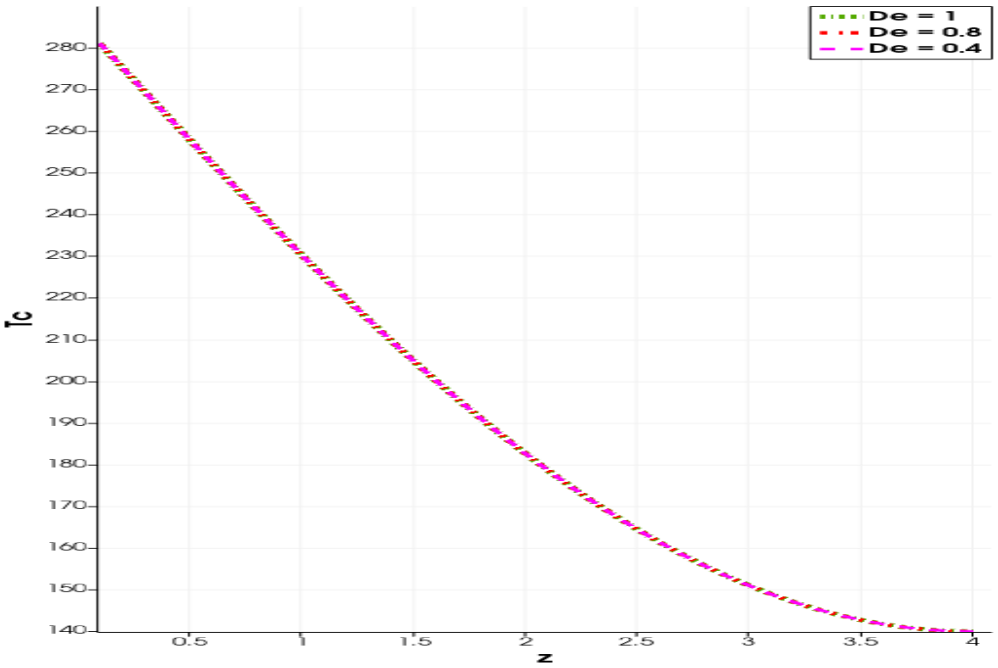


**Figure 3.36:** Effects of Deborah number, $De$, on the core-fluid temperature. Fluid moving from inlet at $z = 0$ to outlet at $z = 4$, i.e., flow direction is from left to right ($\longrightarrow$).

## 3.6 Concluding Remarks

The results of this Chapter illustrate that an increase in the nano-particle volume-fraction, in the coolant NFBN, leads to enhanced heat exchange characteristics from the hot core fluid to the coolant shell NFBN. Significantly, the results illustrate that the use of NFBN as the coolant fluid leads to better heat-transfer characteristics as compared to using an ordinary/conventional (particle-free) Newtonian coolant. The results also demonstrate that the efficacy of the NFBN as a coolant is enhanced with increasing nano-particle volume-fraction. The next Chapter expands on these concepts and investigates the effects of nano-particles and nanofluids in boiling flow problems, specifically the enhancement of boiling and vapour formation via nano-particles and nanofluids.

# Chapter 4

# Volume-of-fluid based finite-volume computational simulations of three-phase nanoparticle-liquid-gas boiling flow problems in vertical rectangular channels*

## 4.1 Abstract

This study develops robust numerical algorithms for the simulation of three-phase (solid-liquid-gas) boiling flow and bubble formation problems in rectangular channels. The numerical algorithms are based on the Finite Volume Methods (FVM) and implement both the volume-of-fluid (VOF) methods for liquid-gas interface tracking as well as the volume-fraction methods to account for the concentration of embedded

*The contents of this chapter are from [159]

solid nano-particles in the liquid phase. Water is used as the base-liquid and the solid phase is modelled via metallic nano-particles (both aluminium oxide and titanium oxide nano-particles are considered) that are homogeneously mixed within the liquid phase. The gas phase is considered as a vapour arising from the boiling processes of the liquid-phase. The finite volume methodology is implemented on the OpenFOAM software platform, specifically by careful modification and manipulation of existing OpenFOAM solvers. The governing fluid dynamical equations, for the three-phase boiling problem, take into account, the thermal conductivity effects of the solid (nano-particle), the momentum and energy equations for both the liquid-phase and the gas-phase, and finally the decoupled mass conservation equations for the liquid- and gas-phases. The decoupled mass conservation equations are specifically used to model the phase change between the liquid- and gas- phases. In addition to the FVM and VOF numerical methodologies for the discretization of the governing equations, the pressure-velocity coupling is resolved via the PIMPLE algorithm, a combination of the Pressure Implicit with Splitting of Operator (PISO) and the Semi-Implicit Method for Pressure-Linked Equations (SIMPLE) algorithms. The computational results are presented graphically with respect to variations in time as well as in the nano-particle volume fractions. The simulations and results accurately capture the formation of vapour bubbles in the two-phase (particle-free) liquid-gas flow and additionally the computational algorithms are similarly demonstrated to accurately illustrate and capture simulated boiling processes. The presence of the nano-particles is demonstrated to enhance the heat-transfer, boiling, and bubble formation processes.

## 4.2 Introduction

Three-phase, solid-liquid-gas flows are a subset of the broader category of multi-phase flows. The turbulent nature of multi-phase flow that contain the liquid-gas

phases make the mathematical models for such flows highly intractable to analytical solution or treatment. A recourse to computational-fluid-dynamics (CFD) techniques is therefore unavoidable in the mathematical solution and simulation of the multi-phase flow problems that contain the liquid-gas phase. Indeed, the coupled and non-linear nature of multi-phase in general make them intractable to analytical treatment. Great progress has been made over the years in developing computational tools that can complement experimental investigations of multi-phase flows. Investigation into multi-phase flow problems have largely therefore been conducted via experimental or CFD techniques. Important CFD techniques that have been developed to track the complex mixing and interactions in, say, liquid-gas phase change flows include the volume-of-fluid (VOF) method, see for example [160, 161, 82, 162]; Eulerian-Eulerian techniques, see for example [42, 163, 164]; and the Lagrangian tracking of individual particles, see for example [165, 166, 167]. The VOF method has proved to be an excellent tool specifically for interface tracking in liquid-gas phase change problems, see for example [168, 148, 149].

The work in [160] employed VOF methods to numerically investigate boiling flow using an R-141B refrigerant in a horizontal coiled pipe and their results were in good agreement with experimental data. The investigations in [171] numerically simulated the transient heat transfer process, during nucleate boiling, using an HFE-700 refrigerant via a VOF based OpenFOAM solver. In these simulations, the VOF method was coupled with the Level Set(LS) approach to more accurately capture the exact position of the interface. The research in [162] developed a VOF based OpenFOAM solver to simulate a broad range of boiling, condensation, and evaporation problems within a single environment. The work in [172] employed a Hart evaporation model, based on VOF, FVM, and PISO algorithms implemented in OpenFOAM, for interface tracking. The VOF interface tracking methods coupled

with the FVM numerical methodologies were also employed in [173] to model phase-change processes in two-phase fluid flow. Validation tests using the 1D Stefan-Problem and a 2D axi-symmetric film boiling were conducted, in [173], and simulation results were in excellent agreement with analytical results. The investigations in [174] used the color-function volume-of-fluid (CF-VOF) interface tracking methods in OpenFOAM to simulate boiling and condensation processes. Additionally, the surface tension was modelled via the continuous-surface-force (CSF) model and the pressure-velocity coupling was resolved by employing the PISO algorithm on a collocated grid. A comprehensive discussion on the VOF-linked color-functions and mollified color-functions as well as mathematical descriptions of the CSF, and related continuous-surface-stress (CSS) models can be found, say in [175] in which. The work in [175] investigated the deformation and break-up of liquid droplets in a two-phase, droplet-matrix mixture and the pressure correction was conducted via the SIMPLE algorithms.

Various phase-change models have been developed to characterize the phase-change phenomenon for liquid-gas flows, these include the Scharge model [176], Tanasawa model [177], Lee model [178], Sun model [181] and temperature recovery model [182]. The Scharge model is based on modelling the pressure difference on each side of the two-phase flow interface. Specifically, this pressure difference results in differential saturation temperatures across the interface and the phase change mass flux is calculated from the mass balance at the interface. The Tanasawa model simplifies the Scharge model by assuming a constant saturation temperature on both sides of the interface. The Lee model is a derivative of the Scharge model in which it is assumed that the boiling process occurs at a constant pressure across the interface. The Sun model, simplifies the sharp interface model (which assumes that the heat received by the interface is used in evaporation) by removing the thermal conductivity of the

gaseous phase. In the temperature recover model, it is assumed that the interface cells reach the thermal equilibrium condition immediately.

The present work incorporates a solid (nano-particle) phase to existing two-phase, liquid-gas, problems and, in turn, the Lee model, [178] which has indeed been widely used in two-phase, liquid-gas boiling flow simulations, see for example [183, 184, 185, 186, 187], is employed. The present study simulates the liquid-gas phase change (boiling) process using the VOF and FVM based OpenFOAM solver *interCondensatingEvaporatingFoam* and additionally incorporates a solid (nano-particle) phase via a volume-fraction parameter and relevant modifications to the thermal conductivity functions and hence also to the *interCondensatingEvaporatingFoam* solver. This solver supports evaporation and condensation between fluid and vapour for non-isothermal immiscible fluids using VOF interface capturing. The broader aims of the present research are to develop multi-domain and multi-phase flow solvers, modified from the solvers used in the present work, for the purposes of multi-domain heat-exchanger simulations with phase change. Specifically, such an solver would be capable of resolving the multi-domain heat-exchanger flow problems, such as those presented in [86, 120], with combined multi-phase flow effects such as in the present work.

## 4.3 Physical and Mathematical Model

The physical model geometry is represented by a vertical rectangular channel of vertical length 4m and horizontal width 1m, see illustration in Fig. 4.1. The fluid motion is induced only by natural-convection, a thermodynamic phenomenon referred to as pool-boiling.

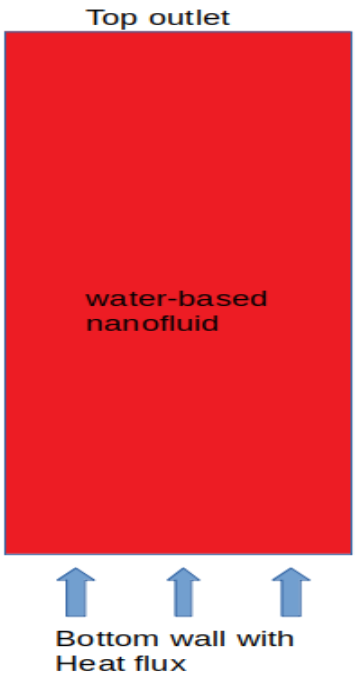


**Figure 4.1:** Schematic of model problem

The computational modelling in the present two-phase, liquid-gas flow study will require an efficient method to continuously track (in space and time) the liquid-vapour interface. The well developed volume-of-fluid (VOF) method will be employed for these purposes – to track the liquid-vapour interface. Specifically, the VOF method uses a volume-fraction indicator, say $\alpha$, to describe the volume-fraction of one phase (say the liquid phase) at any point and time in a computational cell within the flow field, [188]. The volume-fraction $\alpha$ in the present sense will therefore be taken to indicate the ratio of the liquid volume in a computational cell to the total cell volume. It therefore easily follows that if the cell is completely filled with liquid, then $\alpha = 1$, if the cell is completely filled with vapour, then $\alpha = 0$, if the cell is half filled with liquid, then $\alpha = 0.5$, if the cell is three quarter filled with liquid, then $\alpha = 0.75$, etc.

This leads to the following definition of the volume-fraction $\alpha$

$$\alpha(y,t) = \begin{cases} 0 & \text{vapour phase,} \\ 0 < \alpha < 1 & \text{mixing region,} \\ 1 & \text{liquid phase.} \end{cases}$$

The flow quantities; i.e. the density ($\rho$), heat capacity ($c_p$), viscosity ($\mu$), and thermal conductivity ($K$), of the three-phase mixture may therefore be computed, in each computational cell, as the linear combinations of the respective contributions from the nanofluid phase, $()_{nf}$, and the vapour phase, $()_v$,

$$\rho = \alpha\rho_{nf} + (1-\alpha)\rho_v, \tag{4.1}$$

$$\rho\, c_p = \alpha(\rho\, c_p)_{nf} + (1-\alpha)(\rho\, c_p)_v, \tag{4.2}$$

$$\mu = \alpha\mu_{nf} + (1-\alpha)\mu_v, \tag{4.3}$$

$$K = \alpha K_{nf} + (1-\alpha)K_v, \tag{4.4}$$

where, $()_{nf}$, represents the homogeneous nanofluid mixture formed from the combination of solid nano-particles, $()_s$, that are homogeneously embedded in the base-liquid, $()_{bl}$, phase. What we have so far referred to as the liquid-phase, should therefore more correctly now be referred to as the base-liquid phase. Specifically, the three-phase mixture is composed of nano-particles, a base-liquid, and a vapour. The nano-particles and base-liquid are homogeneously mixed to form the nanofluid.

The nanofluid density, heat capacity, and viscosity are calculated from a combination of the solid (nano-particle) contribution, $()_s$, and the base-liquid contribution, $()_{bl}$,

see for example [120, 152, 153, 189, 190],

$$\rho_{nf} = \varphi\rho_s + (1-\varphi)\rho_{bl}, \tag{4.5}$$

$$(\rho\, c_p)_{nf} = \varphi\,(\rho\, c_p)_s + (1-\varphi)\,(\rho\, c_p)_{bl}, \tag{4.6}$$

$$\mu_{nf} = \frac{\mu_{bl}}{(\sqrt{1-\varphi})^5}. \tag{4.7}$$

where $\varphi \in [0,1]$ is the volume-fraction of the nano-particles,

$$\varphi = \begin{cases} 0, & 0\% \text{ of nano-particles by volume in nanofluid,} \\ 0 < \varphi < 1, & 100\varphi\% \text{ nano-particles by volume in nanofluid,} \\ 1, & 100\% \text{ nano-particles by volume in nanofluid.} \end{cases}$$

The thermal conductivity for the nanofluid is empirically determined, see for example [120, 152, 153, 189, 190], the following empirical formula is adopted,

$$K_{nf} = \frac{K_s + (1-\aleph)K_{bl} + (1-\aleph)\varphi(K_{bl} - K_s)}{K_s + (1-\aleph)K_{bl} + \varphi(K_{bl} - K_s)}\,(1 + \varepsilon\, A_2\, T), \tag{4.8}$$

where $\varepsilon$ and $A_2$ are thermal-conductivity parameters and $\aleph$ is an empirically determined nano-particle shape-factor. For spherical-shaped nano-particles, $\aleph = 3$, [120, 152, 153, 189, 190].

### 4.3.1 Conservation equations

The dynamical governing equations for the nanofluid and vapour phases are obtained from the conservation laws, namely the conservation of mass, momentum, and energy, respectively given as,

$$\frac{\partial \rho}{\partial t} + \nabla \cdot (\rho \boldsymbol{U}) = 0, \tag{4.9}$$

$$\frac{\partial}{\partial t}(\rho \boldsymbol{U}) + \nabla \cdot (\rho \boldsymbol{U}\,\boldsymbol{U}) = -\nabla p + \nabla \cdot \left[\mu(\nabla \boldsymbol{U} + \nabla \boldsymbol{U}^T) - \frac{2}{3}(\nabla \cdot \boldsymbol{U})\boldsymbol{I}\right] + \rho(\boldsymbol{F}_g + \boldsymbol{F}_\sigma), \tag{4.10}$$

$$\frac{\partial}{\partial t}(\rho c_p T) + \boldsymbol{U} \cdot \nabla(\rho c_p T) = \nabla \cdot (K \nabla T) + Q, \tag{4.11}$$

where $\boldsymbol{U}$ the velocity field, $p$ the pressure field, $\boldsymbol{F}_g$ is the gravitational force field, $\boldsymbol{F_\sigma}$ is the force due to surface-tension, $T$ the temperature field, $c_p$ the specific heat capacity at constant pressure, and $Q$ represents heat sources. The surface-tension, $\boldsymbol{F}_\sigma$, is calculated using the continuum-surface-force (CSF) model for the cells containing the nanofluid-vapour interface [175, 191],

$$\boldsymbol{F}_\sigma = \sigma \frac{\rho_{nf}\,\alpha_{nf}\,\kappa_v \boldsymbol{N}_v + \rho_v\,\alpha_v\,\kappa_{nf}\boldsymbol{N}_{nf}}{0.5\,(\rho_{nf} + \rho_v)},$$

where $\sigma$ is the surface tension of the nanofluid, $\alpha_v$ is the vapour volume fraction, $\alpha_{nf}$ is the nanofluid volume fraction, $\rho_v$ is the vapour density, $\rho_{nf}$ is the nanofluid density, $\kappa_v$ is the curvature of the vapour phase, $\kappa_{nf}$ is curvature of the nanofluid phase. In our notation, we assume $\alpha_{nf} = \alpha$ and $\alpha_v = 1 - \alpha_{nf} = 1 - \alpha$. The unit normal vectors are defined as,

$$\boldsymbol{N}_{nf} = \frac{\nabla \alpha_{nf}}{|\nabla \alpha_{nf}|}, \quad \boldsymbol{N}_v = \frac{\nabla \alpha_v}{|\nabla \alpha_v|}.$$

In the Lee model, [178], which is adopted in the present work, the continuity (mass conservation) equation, Eq. (4.9) is not solved directly for the combined phases, as with the momentum and energy equations, Eqs. (4.10) and (4.11). The mass conservation equation will therefore be solved, for each phase, via Lee's phase change model.

### 4.3.2 Phase change model

The phase change is model is described via Lee's model [178]. This model is based on the assumption that mass is transferred at a quasi-thermo-equilibrium and at constant pressure. The mass transfer depends mainly on the shared and saturated temperatures. Accordingly, the mass conservation equations for the volume fractions of the nanofluid and vapour phases are respectively,

$$\frac{\partial \alpha_{nf}}{\partial t} + \nabla \cdot (\boldsymbol{U} \alpha_{nf}) = \frac{S_{nf}}{\rho_{nf}}, \tag{4.12}$$

$$\frac{\partial \alpha_{v}}{\partial t} + \nabla \cdot (\boldsymbol{U} \alpha_{v}) = \frac{S_{v}}{\rho_{v}}. \tag{4.13}$$

The source terms due to phase change, $S_{nf}$ and $S_v$ are adopted from Lee's phase change model, [178],

$$S_{nf} = C_{nf}\, \rho_{nf}\, \alpha_{nf}\, \rho_{nf}\, \frac{T - T_{\text{sat}}}{T_{\text{sat}}} \quad T \geq T_{sat}, \tag{4.14}$$

$$S_{v} = C_{v}\, \rho_{v}\, \alpha_{v}\, \rho_{v}\, \frac{T_{\text{sat}} - T}{T_{\text{sat}}} \quad T < T_{sat}, \tag{4.15}$$

where $T_{\text{sat}}$ is the saturation temperature of the nanofluid, $T$ is the temperature of the three-phase mixture, $C_{nf}$ and $C_e$ are empirically determined phase change coefficients, [183, 192, 160, 193]. The values of $C$ must be chosen such that they maintain the interfacial temperature reasonably close to the saturation temperature and also prevent divergence problems. We adopt the value $C = C_{nf} = C_v = 1500\text{s}^{-1}$ used in [178].

### 4.3.3 Turbulence modelling

The turbulence modelling is achieved via the Shear Stress Transport (SST) model, see [179, 180], which essentially combines the best aspects of the $k$-$\omega$ and the $k$-$\varepsilon$ formulations,

$$\frac{D}{Dt}(\rho k) = \boldsymbol{\Sigma} - \beta^* \rho k \omega + \nabla \cdot [(\mu + \sigma_k \mu_t) \nabla k] \tag{4.16}$$

$$\frac{D}{Dt}(\rho \omega) = \frac{\gamma}{\hat{\nu}_t} \hat{\boldsymbol{\Sigma}} - \beta \rho \omega^2 + \nabla \cdot [(\mu + \sigma_\omega \mu_t) \nabla \omega] + 2(1 - F1) \rho \sigma_{\omega 2} \frac{1}{\omega} \nabla k \cdot \nabla \omega. \tag{4.17}$$

The production terms, $\boldsymbol{\Sigma}$ and $\hat{\boldsymbol{\Sigma}}$, are,

$$\hat{\boldsymbol{\Sigma}} = \left[ \mu_t \left( \nabla \boldsymbol{U} + \nabla \boldsymbol{U}^T - \frac{2}{3} (\nabla \cdot \boldsymbol{U}) \boldsymbol{I} \right) - \frac{2}{3} \rho k \boldsymbol{I} \right] \nabla \boldsymbol{U},$$

$$\boldsymbol{\Sigma} = \min\{\hat{\boldsymbol{\Sigma}}, 10 \beta^* \rho k \omega\},$$

where $\boldsymbol{I}$ is the unit tensor. The kinematic eddy viscosities are,

$$\nu_t = \frac{\mu_t}{\rho} = \frac{a_1 k}{\max\{a_1 \omega, \dot{\gamma} F_2\}},$$

$$\hat{\nu}_t = \max\{\nu_t, 10^{-8}\},$$

where $\dot{\gamma}$ is the invariant measure of the rate-of-strain, i.e. the absolute value of the strain rate,

$$\dot{\gamma} = |\boldsymbol{S}| = \sqrt{2\, \boldsymbol{S} : \boldsymbol{S}^T}, \quad \text{where} \quad \boldsymbol{S} = \frac{1}{2} \left[ \nabla \boldsymbol{U} + (\nabla \boldsymbol{U})^T \right].$$

The material derivative $D/Dt$ is,

$$\frac{D}{Dt}(\#) = \frac{\partial \#}{\partial t} + \boldsymbol{U} \cdot \nabla(\#),$$

For ease of comparison with the notation of [179, 180], Eqs. (4.16) and (4.17) may also be cast in tensorial index notation, for example, Eq. (4.16) can be recast as,

$$\frac{\partial}{\partial t}(\rho k) + \frac{\partial}{\partial x_i}(\rho U_i k) = \Sigma_k - \beta^* \rho k \omega + \frac{\partial}{\partial x_i}\left[(\mu + \sigma_k \mu_t)\frac{\partial k}{\partial x_i}\right],$$

with,

$$\hat{\Sigma}_k = \left[\mu_t \left(U_{i,j} + U_{j,i} - \frac{2}{3}\nabla \cdot U_{k,k}\delta_{ij}\right) - \frac{2}{3}\rho k \delta_{ij}\right] U_{i,j},$$

$$\Sigma_k = \min\{\hat{\Sigma}_k, 10\beta^* \rho k \omega\},$$

The blending functions, $F_1$ and $F_2$, are similarly defined as in [179, 180],

$$F_1 = \tanh\left\{\left\{\min\left[\max\left(\frac{\sqrt{k}}{\beta^* \omega Y}, \frac{500\nu}{Y^2 \omega}\right), \frac{4\rho\sigma_{\omega 2} k}{\mathrm{CD}_{k\omega} Y^2}\right]\right\}^4\right\},$$

$$F_2 = \tanh\left[\left[\max\left(\frac{2\sqrt{k}}{\beta^* \omega Y}, \frac{500\nu}{Y^2 \omega}\right)\right]^2\right],$$

where the closure coefficient, $\mathrm{CD}_{k\omega}$, is defined as,

$$\mathrm{CD}_{k\omega} = \max\left(2\rho\sigma_{\omega 2}\frac{1}{\omega}\nabla k \cdot \nabla \omega, 10^{-10}\right).$$

In index tensor notation, we can write,

$$\nabla k \cdot \nabla \omega = \frac{\partial k}{\partial x_i}\frac{\partial \omega}{\partial x_i}.$$

The coefficients embedded in the SST model are calculated from the blending function, $F_1$, using the formulas such as,

$$\beta = F_1\beta_1 + (1 - F_1)\beta_2, \quad \gamma = F_1\gamma_1 + (1 - F_1)\gamma_2, \quad \text{etc.}$$

where $()_1$ and $()_2$ represent the coefficients of the $k$-$\omega$ and the $k$-$\varepsilon$ model respectively. The values of these coefficients are given in [179, 180],

$$k\text{-}\omega: \quad \sigma_{k_1} = 1.176, \sigma_{\omega_1} = 2.000, \kappa = 0.41, \gamma_1 = 0.5532, \beta_1 = 0.0750, \beta^* = 0.09, c_l = 10,$$

$$k\text{-}\varepsilon: \quad \sigma_{k_2} = 1.000, \sigma_{\omega_2} = 1.168, \kappa = 0.41, \gamma_2 = 0.4403, \beta_2 = 0.0828, \beta^* = 0.09.$$

## 4.4 Numerical and Computational Methodologies

A uniform 2D mesh, as shown in Fig. 4.2, is used in the simulations. The computational mesh grid is created using the OpenFOAM mesh generation tool, *blockMesh*.

The OpenFOAM software implements finite volume methods (FVM) as the standard numerical methodology for the solution of governing equations. The *interCondensatingEvaporatingFoam* solver which already exists on the OpenFOAM platform is designed for two-phase, liquid-gas, boiling flow simulations. This solver is adopted and modified as necessary to fit the simulations in the present work, specifically,

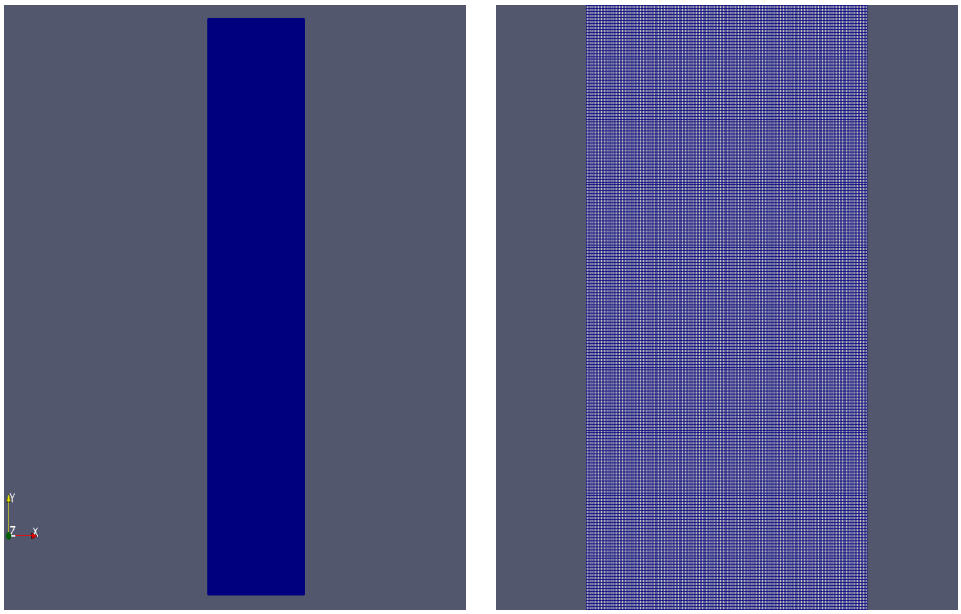

**Figure 4.2:** Mesh grid

the inclusion of the solid (nano-particle) phase and hence also incorporating relevant modifications to the embedded parameters such as the base-liquid density, viscosity, specific heat capacity, and thermal conductivity.

The multi-phase mixture is initially at rest with an initial temperature of 373 K and pressure at $10^5\,\mathrm{kg/m^3}$. The turbulence parameters, $k, \varepsilon, \nu_t$, and $\omega$ are all set to 1. At the bottom wall, the inlet temperature is set at 390 K and the inlet velocity is set to 2 m/s. Standard no-slip boundary conditions are imposed on the velocity at the vertical (solid) walls. The wall function boundary condition is implemented for the turbulence parameters. The inlet-outlet boundary condition is also implemented for turbulence parameters except for $\nu_t$ for which a calculated boundary condition is used. At the outlet, zero-gradient boundary conditions are considered for temperature and velocity while a calculated boundary condition is used for the pressure.

The pressure-velocity coupling is resolved via the PIMPLE algorithm, a combination of the Pressure Implicit with Splitting of Operator (PISO) and the Semi-Implicit

Method for Pressure-Linked Equations (SIMPLE) algorithms. A combination of Gauss linear, Gauss upwind, and Gauss interface compression are used for the discretization of spatial derivatives. The first order implicit Euler method is used for the discretization of time derivatives. The discrete systems of algebraic equations are solved via robust linear algebraic techniques with appropriate smoothers. A symmetric Gauss-Seidel smoother is employed for the temperature, velocity, and pressure equations. The pressure equation is otherwise solved via the Preconditioned-Conjugate-Gradient (PCG) technique in conjunction with Geometric-Algebra-Multi-Grid (GAMG) and Diagonal-Incomplete-Cholesky (DIC) pre-conditioners. Turbulence equations are solved using the Preconditioned Bi-Conjugate Gradient Stabilized (PBiCGStab) solver with a Diagonal-Incomplete-LU (DILU) pre-conditioner.

## 4.5 Results and discussion

Unless otherwise indicated, the following default values for the embedded flow quantities will be assumed in the subsequent analysis.

**General quantities:**

| | |
|---|---|
| Number of computational cells ($M_1$) | 100,000 cells |
| Final computational time | 10 s |
| Volume fraction ($\varphi$) | 0.2 |
| Initial fluid temperature | 373 K |
| Inlet fluid temperature | 390 K |
| Inlet fluid velocity | 2 m/s |
| Initial fluid pressure | $10^5$ kg/m$^3$ |

**Water, $H_2O$:**

| | |
|---|---|
| Viscosity of water | 0.001 kg/m/s |
| Density of water | 997.10 kg/m$^3$ |
| Specific heat for water | 4180 J/K/kg |
| Thermal conductivity for water | 0.6071 W/m/K |

**Aluminium Oxide $Al_2O_3$ nano-particles:**

| | |
|---|---|
| Density of $Al_2O_3$ nano-particles | 3970 kg/m$^3$ |
| Specific heat for $Al_2O_3$ nano-particles | 765 J/K/kg |
| Thermal conductivity for $Al_2O_3$ nano-particles | 40 W/m/K |

**Titanium Oxide $TiO_3$ nano-particles:**

| | |
|---|---|
| Density of $TiO_3$ nano-particles | 4250 kg/m$^3$ |
| Specific heat for $TiO_3$ nano-particles | 686.2 J/K/kg |
| Thermal conductivity for $TiO_3$ nano-particles | 8.9538 W/m/K |

### 4.5.1 Mesh dependence

Unlike laminar flows for which reproducible steady-state solutions would be expected after a certain time, turbulent flows are not expected to settle to reproducible steady states. In other words, time convergence to reproducible (identical) steady-state solutions would not be expected for turbulent flow. Even though the quantitative solutions would be expected to differ as indicated, the qualitative behaviour of the turbulent flow solutions would still be expected to be similar. Fig. 4.3 gives the results obtained from using three different mesh sizes; $M_1, M_2, M_3$; and as expected, the quantitative solutions are different but the qualitative behaviour is similar.

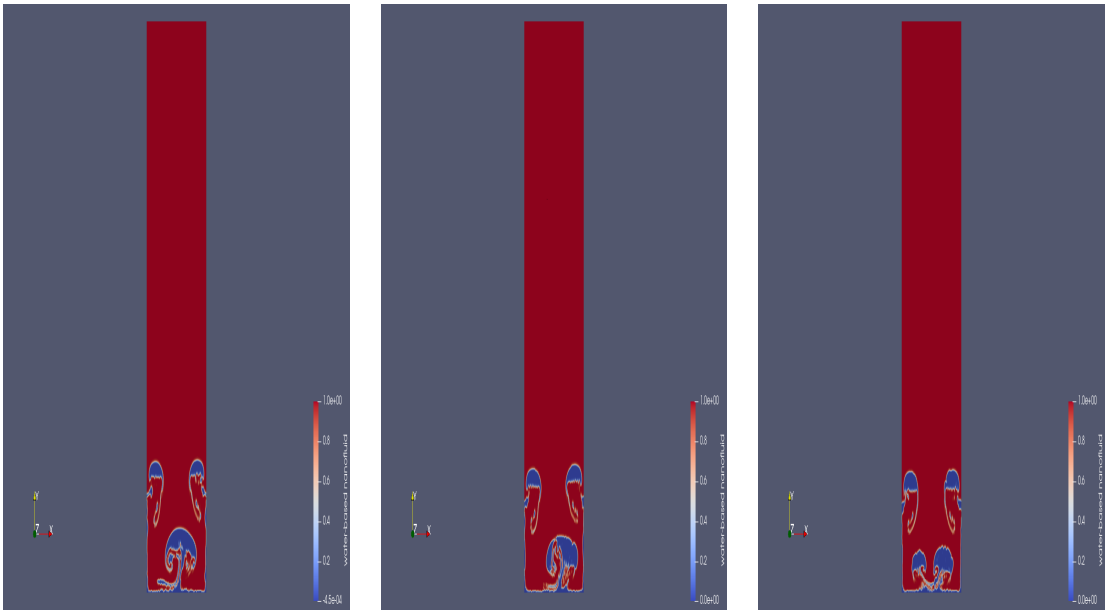

(a) $M_1 = 100,000$ cells (b) $M_2 = 114,400$ cells (c) $M_3 = 121,900$ cells

**Figure 4.3:** Mesh dependence of solutions for a water-$Al_2O_3$ nanofluid.

### 4.5.2 Numerical validation - two-phase flow

To validate the efficacy of the numerical and computational methodologies employed in this investigation, the well documented two-phase, water-air, boiling flow problem in a horizontal channel is considered. The various flow patterns for such two-phase, water-air, boiling flow in a rectangular horizontal channel are illustrated in Fig. 4.4 which is adapted from [38].

The 2D horizontal channel mesh used in the validation tests is shown in Fig. 4.5, generated via the OpenFOAM mesh generation tool, *blockMesh*.

The computational results obtained using the numerical approaches of the present investigation, as displayed in Figs. 4.6, 4.7, 4.8, and 4.9 respectively replicate the expected flow patterns, shown in Fig. 4.4 which is adapted from [38], corresponding to stratified flow, way flow, plug flow, and bubbly flow.

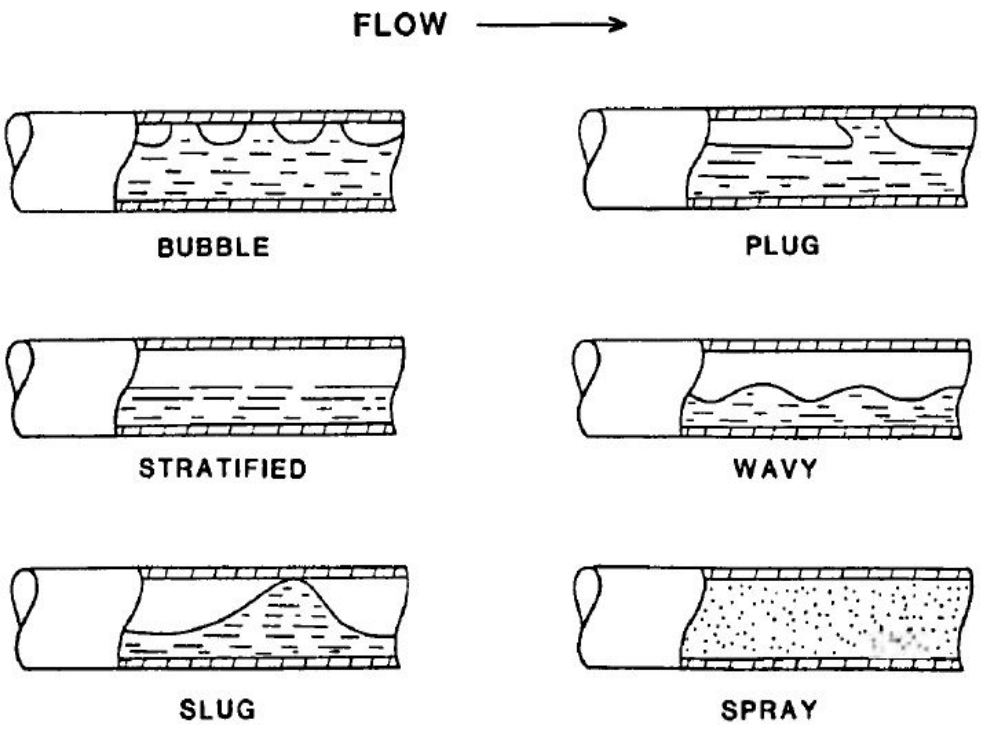


**Figure 4.4:** Two-phase flow pattern, adapted from [38]

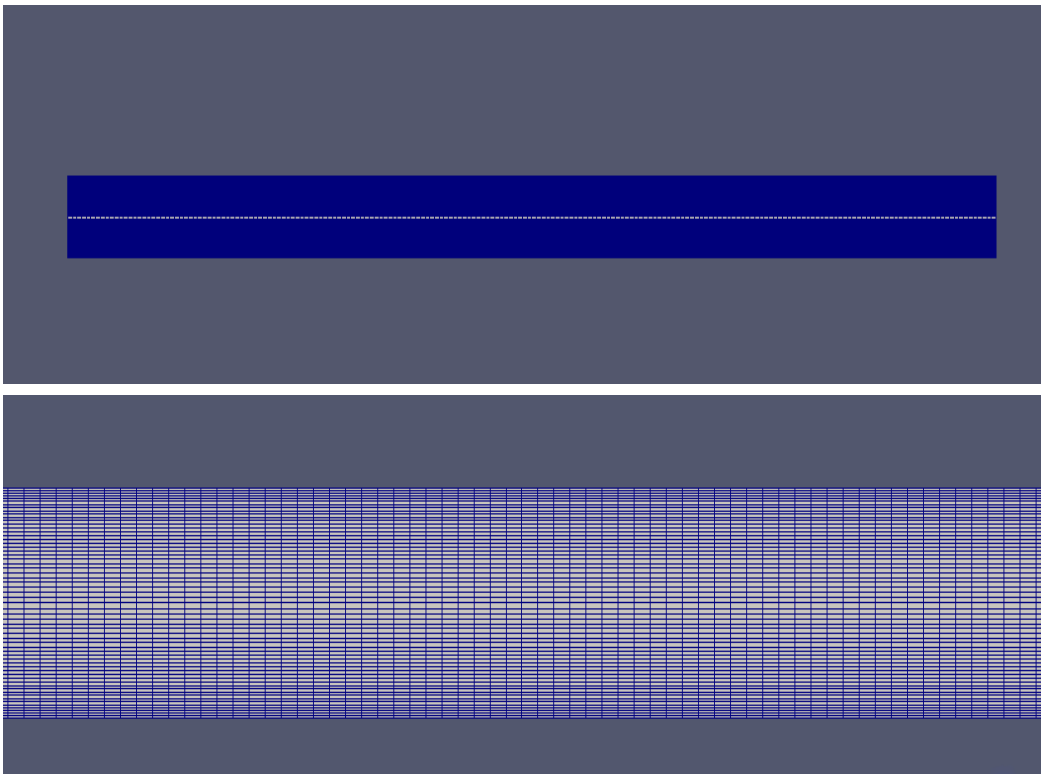

**Figure 4.5:** Mesh generation for two-phase flow pattern computations.

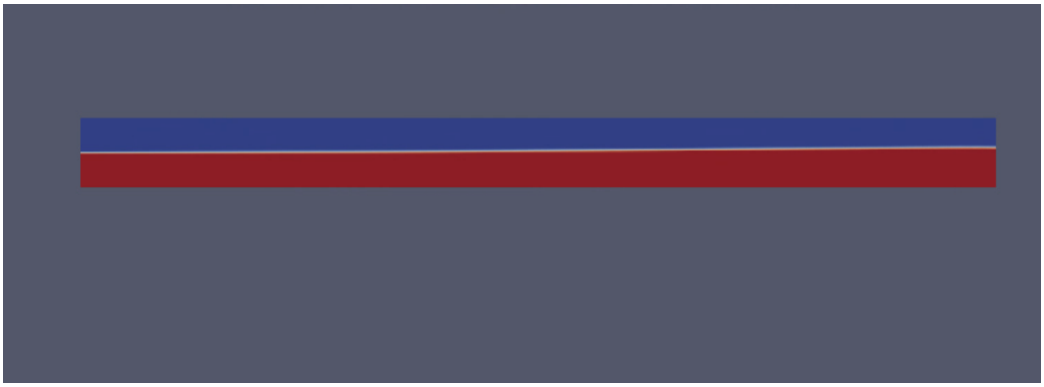

**Figure 4.6:** Stratified flow pattern

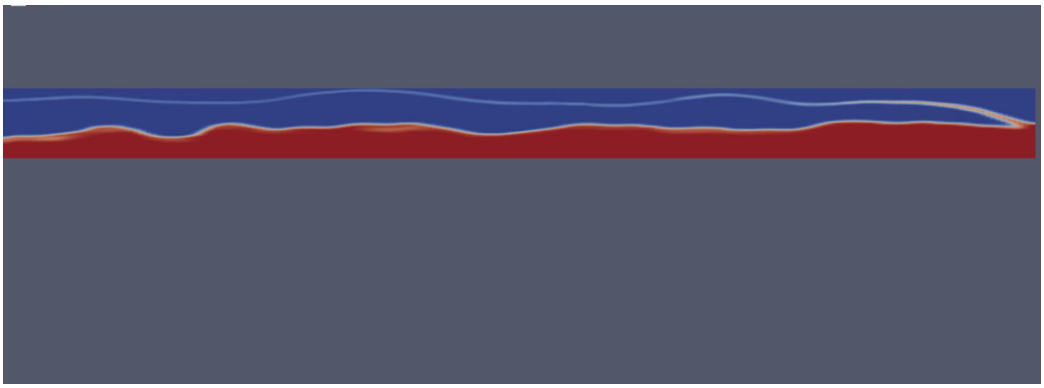

**Figure 4.7:** Wavy flow pattern

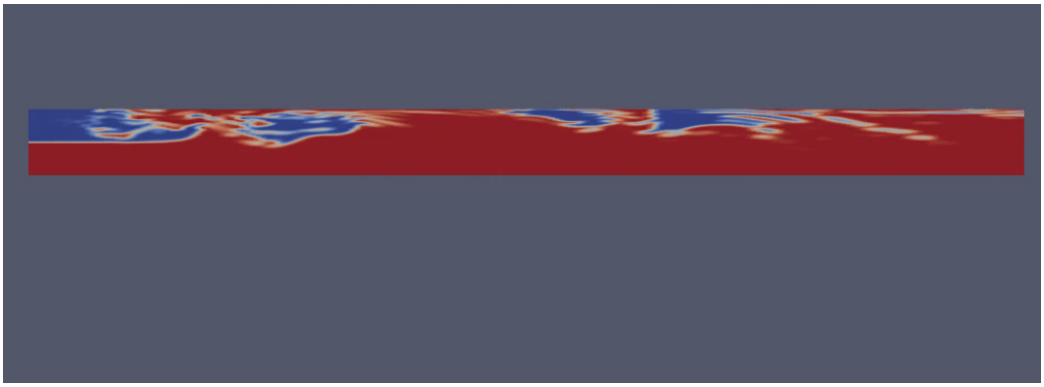

**Figure 4.8:** Plug flow pattern

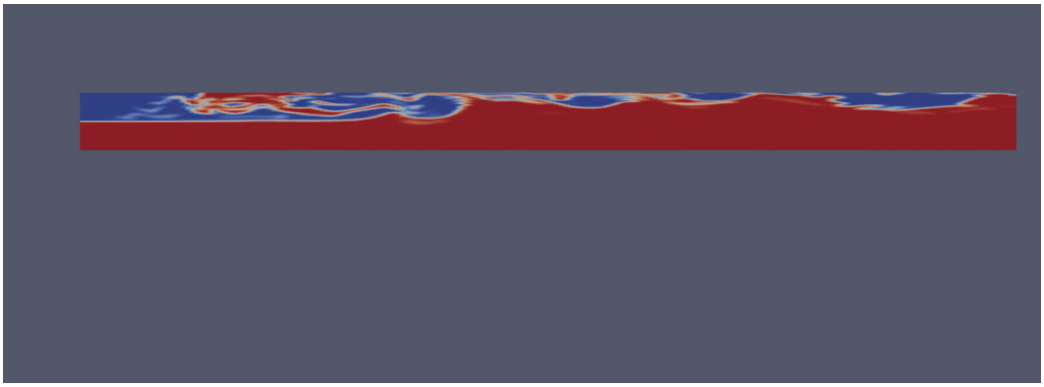

**Figure 4.9:** Bubbly flow pattern

### 4.5.3 Nanofluid results

The transient results, illustrating the evolution in time of the flow patterns for the three types of multi-phase fluid-mixtures, namely; a two-phase water-vapour mixture; a water-vapour-$Al_2O_3$ nanofluid mixture; and a water-vapour-$TiO_2$ are shown in Figs. Figs. 4.10, 4.11, 4.12, and 4.13.

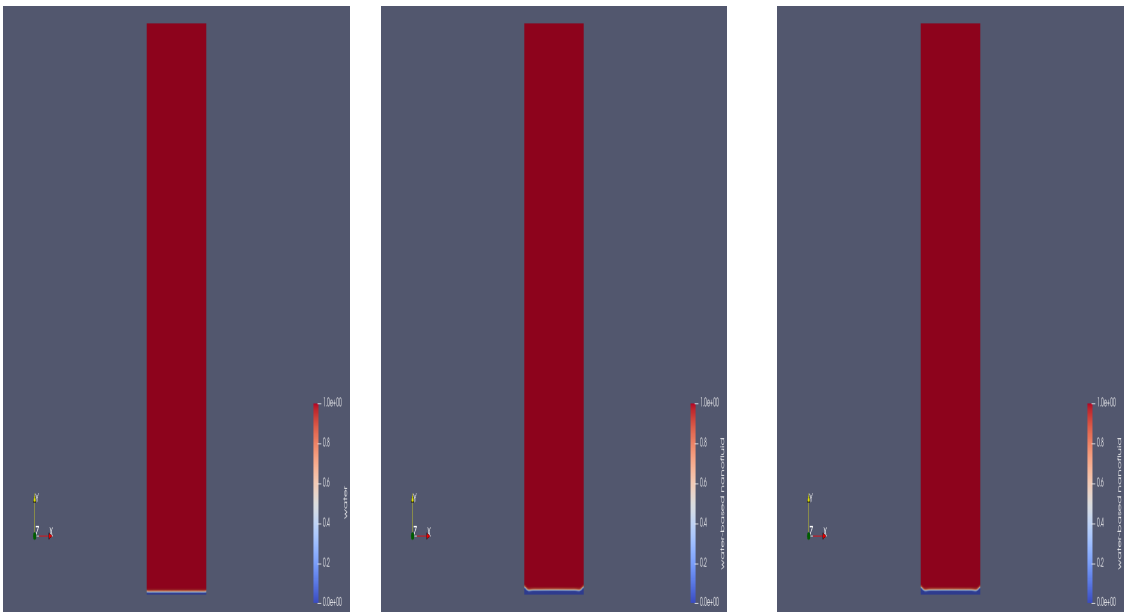

(a) Water (b) Water-$Al_2O_3$ nanofluid (c) Water-$TiO_2$ nanofluid

**Figure 4.10:** Snapshot of solutions for multi-phase mixtures at time $t = 2.5$s.

The computational results shown in Figs. 4.10, 4.11, 4.12, and 4.13 are able to accurately simulate the boiling process and to subsequently also capture the formation of vapour bubbles as time progresses. As time progresses, the hotter fluid progressively becomes dominant leading to boiling and the formation of vapour bubbles. The results demonstrate that the boiling process and hence also formation of vapour bubbles (denoted by the blue areas in the graphs) is significantly enhanced for the nanofluid cases than for the ordinary water case. The bubbly regions are identified by the regions of low temperature, i.e. the blue areas on the graphs. The explanation

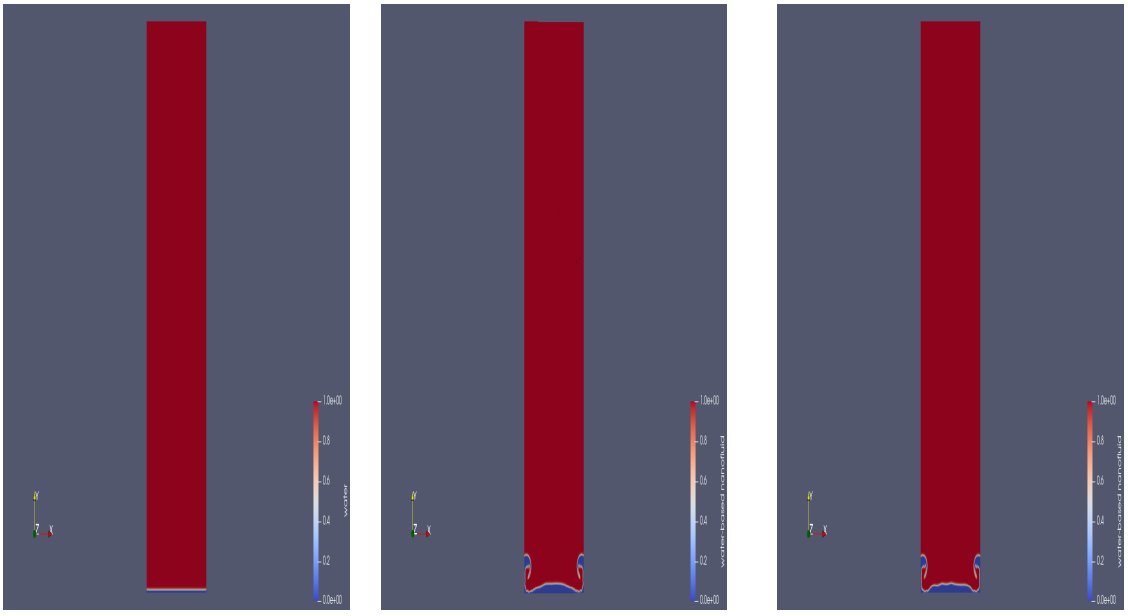

(a) Water (b) Water-$Al_2O_3$ nanofluid (c) Water-$TiO_2$ nanofluid

**Figure 4.11:** Snapshot of solutions for multi-phase mixtures at time $t = 5$s.

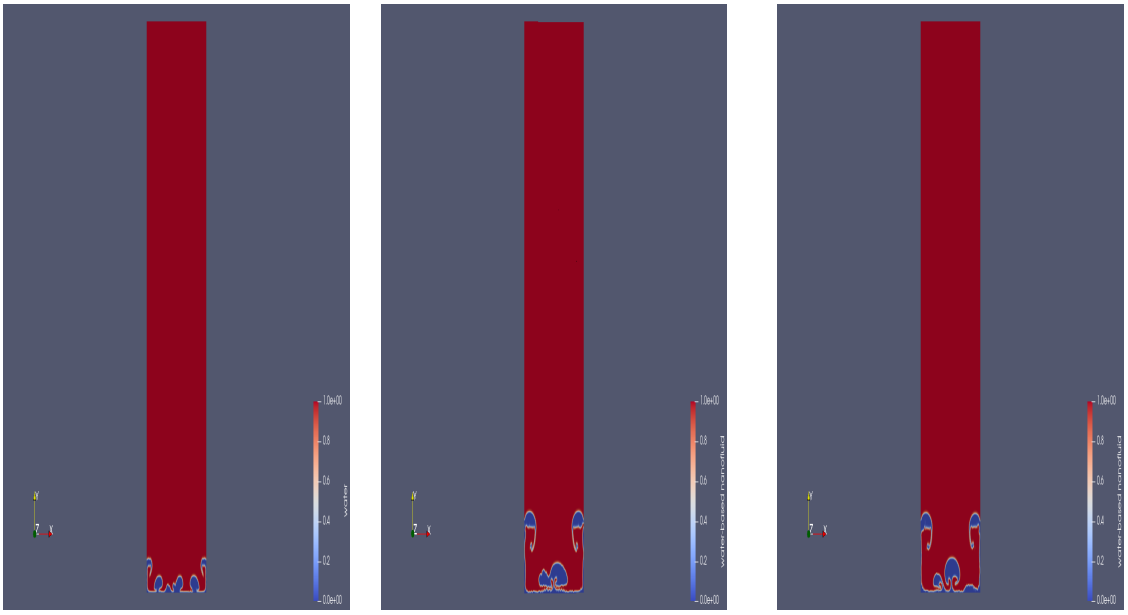

(a) Water (b) Water-$Al_2O_3$ nanofluid (c) Water-$TiO_2$ nanofluid

**Figure 4.12:** Snapshot of solutions for multi-phase mixtures at time $t = 7.5$s.

for this is straightforward. The region inside the air/vapour bubbles will always be significantly cooler than that in the surrounding continuum liquid (water in this

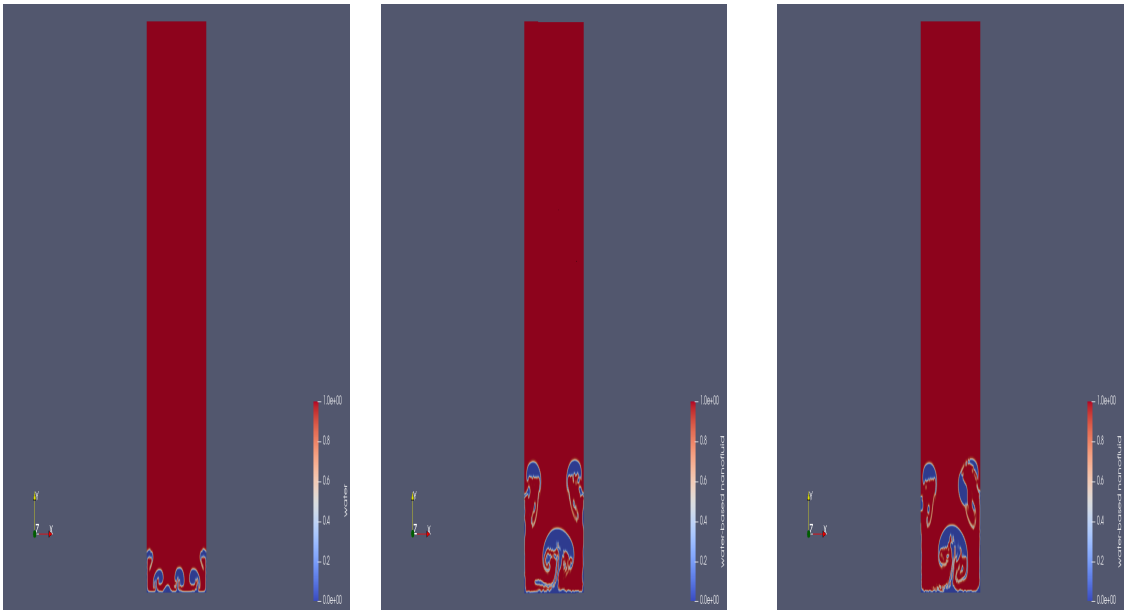

(a) Water (b) Water-$Al_2O_3$ nanofluid (c) Water-$TiO_2$ nanofluid

**Figure 4.13:** Snapshot of solutions for multi-phase mixtures at time $t = 10$s.

case). Plumbers generally use this simple test in domestic and industrial applications to check the flow properties and heating efficiencies of domestic or industrial geysers. By placing your hand under a tap of running hot water, if there is a significant presence of bubbles, then the water would not be as hot as expected from (or recorded on) the source-geyser thermostat settings.

The qualitative results for both types of nanofluids, $H_2O$-$Al_2O_3$ nanofluid and $H_2O$-$TiO_2$, are similar despite the distinctly different properties of the constituent nano-particles. The reason reduces to the realization that the properties of the resultant nanofluids at the operating temperatures and volume fractions are in fact similar. This is illustrated in Table 4.1 using the temperature, $T = 390$K, and the volume fraction, $\varphi = 0.2$.

Specifically, Table 4.1 shows that even though, say, the thermal conductivities of $Al_2O_3$ and $TiO_2$ nano-particles are quite different – respectively 40 W/m/K and 8.9538 W/m/K; the respective thermal conductivities of the corresponding

**Table 4.1:** Comparative properties of water, nano-particles, and nanofluids at $T = 390\text{K}$ and $\varphi = 0.2$

| | $Al_2O_3$ | $TiO_2$ | $H_2O$ | $H_2O$-$Al_2O_3$ | $H_2O$-$TiO_2$ |
|---|---|---|---|---|---|
| Density, kg/m$^3$ | 3970 | 4250 | 997.10 | 1591.68 | 1647.68 |
| Specific heat, J/K/kg | 765 | 686.2 | 4180 | 3497 | 3481.24 |
| Thermal conductivity, W/m/K | 40 | 8.9538 | 0.6071 | 29.294551 | 30.295152 |

nanofluids, water-$Al_2O_3$ and water-$TiO_2$, are practically similar – 29.294551 W/m/K and 30.295152 W/m/K. These nanofluid thermal conductivities are significantly (nearly 50 times) higher than the corresponding thermal conductivity of water, 0.6071 W/m/K which explains the results in Figs. 4.10, 4.11, 4.12, and 4.13.

The results therefore clearly imply that the heat conduction properties, and hence also the boiling and bubble formation processes, may be enhanced by employing nanofluids of increasing nano-particle concentration. The results of Figs. 4.14, 4.15, and 4.16; which are respectively for $\varphi = 0.05$, $\varphi = 0.1$, and $\varphi = 0.2$; provide the relevant confirmation.

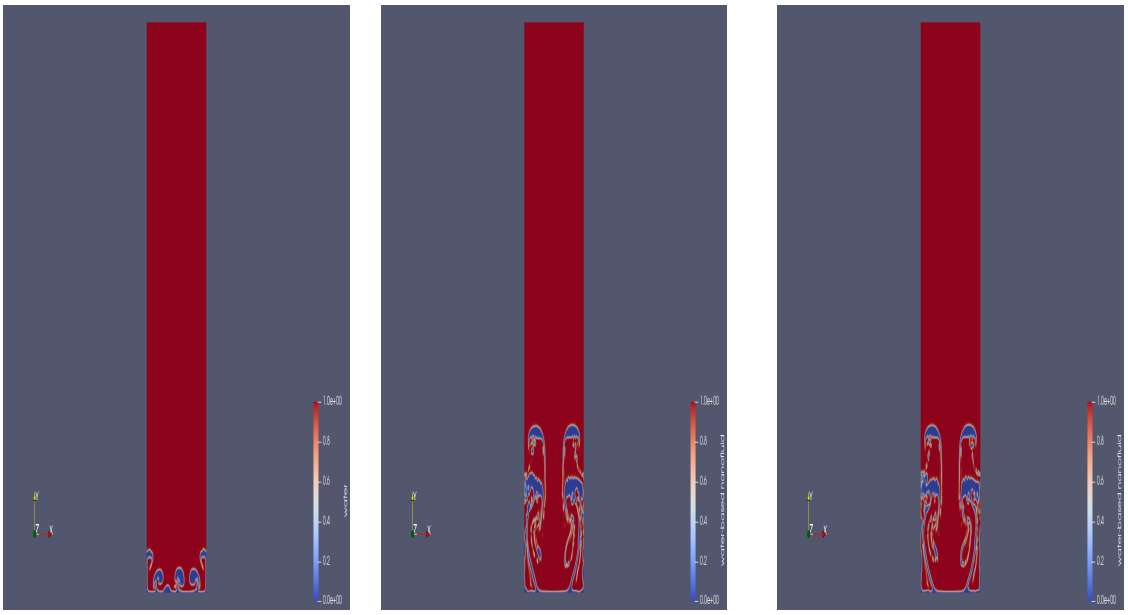

(a) Water (b) Water-$Al_2O_3$ nanofluid (c) Water-$TiO_2$ nanofluid

**Figure 4.14:** Solutions for multi-phase mixtures at time $t = 10\text{s}$ and $\varphi = 0.05$.

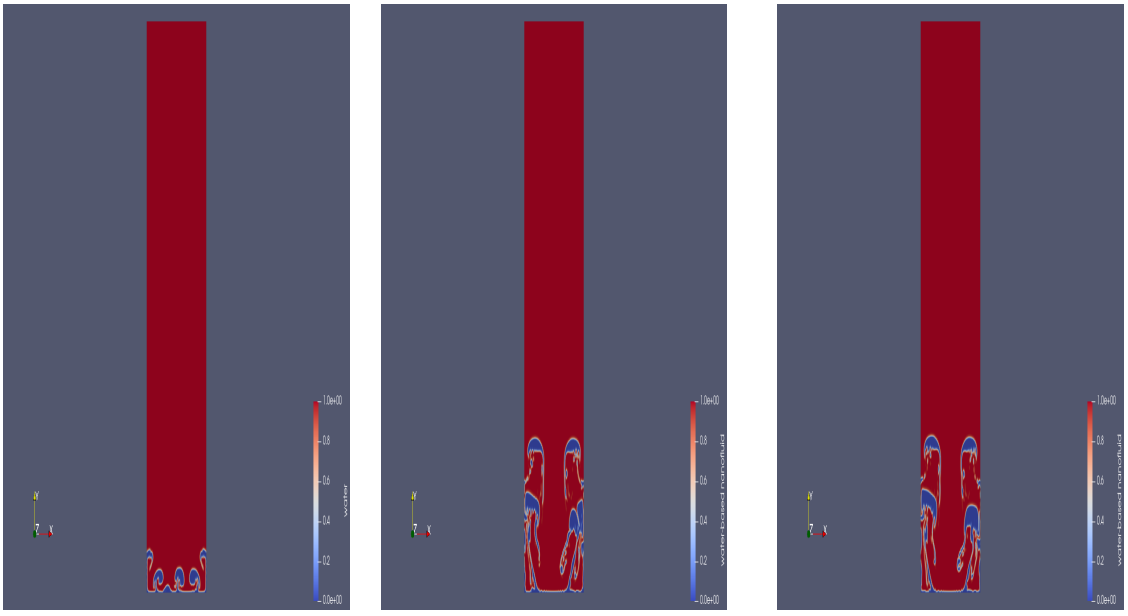

(a) Water (b) Water-$Al_2O_3$ nanofluid (c) Water-$TiO_2$ nanofluid

**Figure 4.15:** Solutions for multi-phase mixtures at time $t = 10$s and $\varphi = 0.1$.

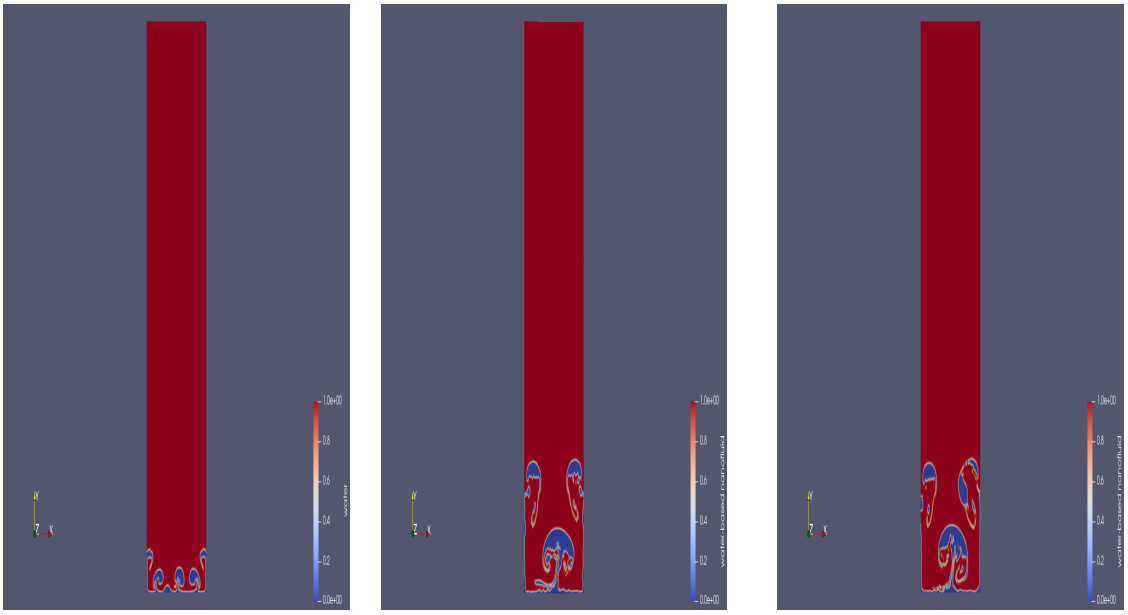

(a) Water (b) Water-$Al_2O_3$ nanofluid (c) Water-$TiO_2$ nanofluid

**Figure 4.16:** Solutions for multi-phase mixtures at time $t = 10$s and $\varphi = 0.2$.

As before, the qualitative results for both types of nanofluids, $H_2O$-$Al_2O_3$ nanofluid and $H_2O$-$TiO_2$, are similar despite the distinctly different properties of the constituent

nano-particles. As before, the reason reduces to the realization that the properties of the resultant nanofluids at the operating temperatures and volume fractions are in fact similar. This is illustrated in Table 4.2 using the temperature, $T = 390$K, and the volume fraction, $\varphi = 0.2$.

**Table 4.2:** Comparative thermal-conductivities of water, nano-particles, and nanofluids at $T = 390$K.

| | $Al_2O_3$ | $TiO_2$ | $H_2O$ | $H_2O$-$Al_2O_3$ | $H_2O$-$TiO_2$ |
|---|---|---|---|---|---|
| Thermal conductivity, $\varphi = 0.05$ | 40 | 8.9538 | 0.6071 | 19.264274 | 19.438368 |
| Thermal conductivity, $\varphi = 0.1$ | 40 | 8.9538 | 0.6071 | 22.229736 | 22.619839 |
| Thermal conductivity, $\varphi = 0.2$ | 40 | 8.9538 | 0.6071 | 29.294551 | 30.295152 |

The results therefore clearly indicate that the thermal conductivities of the nanofluids, and hence also their corresponding heat conduction properties and hence also the boiling and bubble formation processes would be enhanced by increasing the concentration (volume fraction) of the embedded nano-particles. The results of Figs. 4.14, 4.15, and 4.16; which are respectively for $\varphi = 0.05$, $\varphi = 0.1$, and $\varphi = 0.2$; provide the relevant confirmation.

## 4.6 Concluding Remarks

The results of this Chapter accurately capture the formation of vapour bubbles in the two-phase (particle-free) liquid-gas flow and additionally the computational algorithms are similarly demonstrated to accurately illustrate and capture simulated boiling processes. The presence of the nano-particles is demonstrated to enhance the heat-transfer, boiling, and bubble formation processes. The investigation lays the important groundwork to develop computational algorithms for the simulation of heat-transfer problems in coupled geometries, such as heat-exchangers problems of

Chapters 1 and 2 – under conditions of phase-change, boiling, condensation, variable nano-particle concentration, etc.

# Chapter 5

# Concluding Remarks

The thesis develops and computationally analyzes mathematical models for multi-geometry heat-exchanger design and for multi-phase flow problems involving boiling and bubble formation. Newtonian fluids, Newtonian-Fluid-Based- Nanofluids, and non-Newtonian fluids are all considered in the thesis. The Newtonian-Fluid-Based-Nanofluids (NFBN) are designed from the homogeneous mixing of a Newtonian base-fluid with solid nano-particles. Water will be used as the Newtonian base-liquid and two types of nano-particles will be considered, aluminium oxide ($Al_2O_3$) and titanium oxide ($TiO_2$) nano-particles. The non-Newtonian fluids in this thesis are modelled via the Giesekus viscoelastic constitutive equations. The main results of the thesis are given in Chapters 2, 3, and 4.

In Chapter 2, coupled fluid-dynamical and thermodynamical characteristics are investigated in the context of a double-cylinder, counter-flow, heat-exchanger with a heated viscoelastic core fluid and a coolant Newtonian shell fluid. A robust and stabilized finite volume numerical methodology is employed to simulate the combined heat-exchange characteristics and fluid dynamical responses. The finite volume numerical methodology is implemented on the OpenFOAM software platform,

onto which the energy equation for viscoelastic fluid flow is also incorporated. The computational results for the fluid quantities, namely the velocity, temperature, pressure, and polymer-stress components are illustrated graphically and discussed qualitatively. The results show the required heat-exchange behaviour, the coolant fluid flowing in the outer shell acts to cool down the heated core fluid and the connecting-wall temperature averages out the temperature of the two fluids which are separated by the wall. The results obtained set the groundwork for important applications, say to food processing, in which viscoelastic behaviour would be a significant factor. Indeed, the results obtained in this study, and the view to potential applications, lay the groundwork for follow-up work that would involve optimization investigation regarding the optimal design of the coolant composition and rheology. For example, contemporary research has demonstrated the heat transfer enhancement of nanofluids as compared to the corresponding base fluids. Our follow-up investigations will therefore focus on coolant fluids that are composed of nano-particles of varying volume fractions. Such fluids, i.e. base fluids containing nano-particles, are the so-called nanofluids.

Chapter 3 computationally investigates the heat transfer characteristics in a double-pipe counter-flow heat exchanger, with a heated/hot viscoelastic fluid occupying the inner core region and a colder Newtonian-Fluid-Based Nanofluid (NFBN) flowing in the outer shell region. The NFBN is modelled as a single-phase homogenous nanofluid in which the fluid-dynamical and thermodynamical contributions of the embedded nanoparticles are tracked via an appropriate nanoparticle volume-fraction function. A robust numerical methodology based on the finite volume methods (FVM) is employed to solve the complex coupled system of nonlinear PDEs. The FVM algorithms are computationally implemented on the OpenFOAM software platform. The dependence of the field variables on the embedded flow parameters, namely the velocity, temperature, pressure, and polymeric stresses, is explored qualitatively and

quantitatively. Specifically, the results illustrate that an increase in the nanoparticle volume-fraction, in the NFBN, leads to enhanced heat exchange characteristics from the hot core fluid to the colder shell NFBN. Significantly, the results illustrate that the use of NFBN as the coolant fluid leads to better heat-transfer characteristics as compared to using an ordinary/conventional (particle-free) Newtonian coolant. The results also demonstrate that the efficacy of the NFBN as a coolant is enhanced with increasing nanoparticle volume-fraction. The effects of the volume fraction parameter and Prandtl number were observed to be insignificant on the velocity field, pressure field, and polymer-stress components. Similarly, the effects of the Deborah number were observed to be insignificant on the velocity and temperature fields.

The investigations in Chapter 4 develop robust numerical algorithms for the simulation of three-phase, solid-liquid-gas, boiling flow problems in rectangular channels. The numerical algorithms are based on the finite-volume-methods (FVM) and implement both the volume-of-fluid (VOF) methods for liquid-gas interface tracking as well as the volume-fraction methods to account for the concentration of embedded solid nano-particles in the liquid phase. Water is used as the base-liquid and the solid phase is modelled via metallic nano-particles (both aluminium oxide and titanium oxide nano-particles are considered) that are homogeneously mixed within the liquid phase. The gas phase is considered as a vapour arising from the bolling processes of the liquid-phase. The finite volume methodology is implemented on the OpenFOAM software platform, specifically by careful modification and manipulation of existing OpenFOAM solvers. The computational results are presented graphically with respect to variations in time as well as in the nano-particle volume fractions. The simulations and results accurately capture the formation of vapour bubbles in the two-phase (particle-free) liquid-gas flow and additionally the computational algorithms are similarly demonstrated to accurately illustrate and capture simulated boiling processes. The presence of the nano-particles is demonstrated to enhance

the heat-transfer, boiling, and bubble formation processes. The investigation lays the important groundwork to develop computational algorithms for the simulation of heat-transfer problems in coupled geometries, such as heat-exchangers, and under conditions of phase-change, boiling, condensation, variable nano-particle concentration, etc.

# Bibliography

[1] R.B. Bird, R.C. Armstrong, O. Hassager, Dynamics of polymeric liquids, Wiley, New York, 1987.

[2] R.G. Larson, Constitutive equations for polymer melts and solutions, Butterworths, Boston, 1988.

[3] C. W. Macosko, Rheology: Principles, measurements and applications, VCH Publishers, New York, 1994.

[4] J.G. Abuga, T. Chinyoka, Benchmark solutions of the stabilized computations of flows of fluids governed by the Rolie-Poly constitutive model, J. Phys. Commun., 4(1), 2020, 015024.

[5] J.G. Abuga, T. Chinyoka, Numerical Study of Shear Banding in Flows of Fluids Governed by the Rolie-Poly Two-Fluid Model via Stabilized Finite Volume Methods, Processes 8(7), 2020, 810.

[6] F. Habla, A. Woitalka, S. Neuner, O. Hinrichsen, Development of a methodology for numerical simulation of non-isothermal viscoelastic fluid flows with application to axisymmetric 4: 1 contraction flows, Chem. Eng. J., 207, 2012, 772-784.

[7] S. Meburger, M. Niethammer, D. Bothe, M. Schäfer, Validation of Viscoelastic, non-isothermal fluid flow simulations, Annual Transactions of the Nordic Rheology Society, 27, 2019, 109-113.

[8] S. Meburger, M. Niethammer, D. Bothe, M. Schäfer, Numerical simulation of non-isothermal viscoelastic flows at high Weissenberg numbers using a finite volume method on general unstructured meshes, J. Non-Newton Fluid Mech., 287, 2021, 104-451.

[9] T. Chinyoka, Viscoelastic effects in double-pipe single-pass counterflow heat ex-changers, Int. J. Numer. Methods Fluids, 59(6), 2008, 667-690.

[10] T. Chinyoka, Modeling of cross-flow heat exchangers with viscoelastic fluids, Nonlinear Anal. Real World Appl., 10(6), 2009, 3353-3359.

[11] T. Chinyoka, Poiseuille flow of reactive phan–thien–tanner liquids in 1D channel flow, J. Heat Transf, 132(11), 2010, 111701-7.

[12] M. Hütter, C. Luap, H.C. Öttinger, Energy Elastic Effects and the Concept of Temperature in Flowing Polymeric Liquids, Rheol. Acta, 48, 2009, 301-316.

[13] A.M. Khatibi, M. Mirzazadeh, F. Rashidi, Forced convection heat transfer of Giesekus viscoelastic fluid in pipes and channels, Int. J. Heat Mass Transf., 46, 2010, 405–412.

[14] S.N. AlMelhi, L. Khezzar, M.S. AlShehhi, A. Filali, Numerical simulation of heat transfer of non-Newtonian elastic fluid, Proceedings of ASME International Mechanical Engineering Congress & Exposition IMECE, 2015.

[15] F. Pimenta, M.A. Alves, Conjugate heat transfer in the unbounded flow of a viscoelastic fluid past a sphere, Int. J. Heat Fluid Flow, 89, 2021, 108784.

[16] S.U.S. Choi, Enhancing Thermal Conductivity of Fluids with Nanoparticles, In Developments and Applications of Non-Newtonian Flows, Siginer, D.A., Wang, H.P., Eds. FED-Vol. 231/MD-Vol. 66, ASME: New York, NY, USA, 1995, 99–105.

[17] C.T. Nguyen, G. Roy, C.Gauthier, N. Galanis, Heat transfer enhancement using Al2O3–water nanofluid for an electronic liquid cooling system, Appl. Therm. Eng., 27(8-9), 2007, 1501-1506.

[18] M.S. Liu, M.C.C. Lin, I.T. Huang, C.C. Wang, Enhancement of thermal conductivity with CuO for nanofluids, Chem. Eng. Technol., 29(1), (2006).

[19] H. Masuda, A. Ebata, K. Teramea, N. Hishinuma, Alteration of thermal conductivity and viscosity of liquid by dispersing ultra-fine particles, Netsu Bussei, 4, 1993, 227–233.

[20] S.Z. Guo, Y. Li, J.S. Jiang, H.Q. Xie,Nanofluids Containing $\gamma - Fe_2O_3$ Nanoparticles and Their Heat Transfer Enhancements, Nanoscale Res Lett, 5, 2010, 1222–1227.

[21] M. Kalteh, A. Abbassi, M. Saffar-Avval, J. Harting, Eulerian–Eulerian two-phase numerical simulation of nanofluid laminar forced convection in a microchannel, Int. J. Heat Fluid Flow, 32(1), 2011, 170-116.

[22] V. Bianco, F. Chiacchio, O. Manca, S. Nardini, Numerical investigation of nanofluids forced convection in circular tubes, Appl. Therm. Eng., 29, 2009, 3632–3642.

[23] M. Sheikholeslami, S. Abelman, D.D. Ganji, Numerical simulation of MHD nanofluid flow and heat transfer considering viscous dissipation, Int. J. Heat Fluid Flow, 79, 2014, 212-222.

[24] X.H Sun, H. Yan, M. Massoudi, Z.H. Chen, W.T. Wu, Numerical simulation of nanofluid suspensions in a geothermal heat exchanger, Energies, 11(4), 2018, 919.

[25] A. Borah, M.P. Boruah, S. Pati, Conjugate heat transfer in a duct using nanofluid by two-phase Eulerian–Lagrangian method: Effect of non-uniform heating, Innov. Food Sci. Emerg. Technol, 42, 2017, 173-179.

[26] T. Perrotin, D. Clodic, Thermal-hydraulic cfd study in louvered fin-and-flat-tube heat exchangers, J. Int. Acad. Refrig., 27(4), 2004, 422-432.

[27] J.M. Nóbrega, I.M. Afonso, L.F. Melo, C.S. Fernandes, R.P. Dias, J.M. Maia, Thermal behaviour of stirred yoghurt during cooling in plate heat exchangers, J. Food Eng., 76(3), 2005, 433-439.

[28] G. Gan, S.B. Riffat, L. Shao, CFD modelling of pressure loss across tube bundles of a heat exchanger for closed-wet cooling towers, Int. J. Ambient Energy, 21, 2000, 77-84.

[29] J.S. Jayakumar, S.M. Mahajani, J.C. Mandal, P.K. Vijayan, R. Bhoi, Experimental and CFD estimation of heat transfer in helically coiled heat exchangers, Chem. Eng. Res. Des, 86, 2008, 221-232.

[30] M. Akhtari, M. Haghshenasfard, M. R. Talaie, Numerical and Experimental Investigation of Heat Transfer of $\alpha - Al_2O_3$/Water Nanofluid in Double Pipe and Shell and Tube Heat, Numer. Heat Transf.; A: Appl., 63(12), 2013, 941-958.

[31] B.A.K. Naik, A.V. Vinod, Heat transfer enhancement using non-Newtonian nanofluids in a shell and helical coil heat exchanger, Exp. Therm. Fluid Sci, 90, 2018, 132-142.

[32] S. Nukiyama, The maximum and minimum values of the heat Q transmitted from metal to boiling water under atmospheric pressure, Journal of Japanese Society of Mechanical Engineers, 37, 1934, 367–374.

[33] H. Hu, C. Xu, Y. Zhao, K.J. Ziegler, J.N. Chung, Boiling and quenching heat transfer advancement by nanoscale surface modification, Scientific reports 7(1), 2017, 1-16.

[34] V.K. Dhir, Boiling heat transfer, Annual Review of Fluid Mechanics, 30, 1998, 365–401.

[35] R.M. Manglik, On the advancements in boiling, two-phase flow heat transfer, and interfacial phenomena, J. Heat Transfer, 128, 2006, 1237–1241.

[36] S. van Stralen, R. Cole. Boiling phenomena, volume 1. McGraw-Hill, 1979.

[37] O. Baker, Design of pipe lines for simultaneous flow of oil and gas, Oil Gas J., 53, 1954, 185-190.

[38] J.M. Mandhane, G.A. Gregory, K. Aziz, A flow pattern map for gas-liquid flow in horizontal pipes, Int. J. Multiph. Flow, 1(4), 1974, 537-553.

[39] Y. Taitel, A. Dukler, A model for predicting flow regime transitions in horizontal and near horizontal gas-liquid flow, AIChE Journal, 22(1), 1976, 47-55.

[40] M. Darzi, C. Park, Experimental visualization and numerical simulation of liquid-gas two-phase flows in a horizontal pipe, ASME International Mechanical Engineering Congress and Exposition, American Society of Mechanical Engineers, 58424, 2017.

[41] R.G. Tripathi, V.V. Buwa, Numerical simulations of gas-liquid boiling flows using OpenFOAM, Procedia IUTAM, 15, 2015, 178-185.

[42] M. Shademan, R. Balachandar, R. Barron, CFD Simulation of boiling heat transfer using OpenFOAM, ASME International Mechanical Engineering Congress and Exposition, American Society of Mechanical Engineers, 46545, 2014.

[43] R. Zhuan, W. Wang, Flow pattern of boiling in micro-channel by numerical simulation, Int. J. Heat Mass Transf, 55, 2012, 1747-1753.

[44] F. Krause, S. Schüttenberg, U. Fritsching, Modelling and simulation of flow boiling heat transfer, Int. J. Numer. Methods Heat Fluid Flow, 20(3), 2010, 312-331.

[45] T.J. Barth, Aspects of unstructured grids and finite volume solvers for the Euler and Navier–Stokes equations, Lecture Series in Computational Fluid Dynamics, von Karman Institute for Fluid Dynamics, 1994, 1994-04.

[46] D.J. Mavriplis, Unstructured-mesh discretizations and solvers for computational aerodynamics, AIAA journal, 46(6), 1998, 1281-1298.

[47] J.A. Mackenzie, K.W. Morton, Finite volume solutions of convection-diffusion test problems, Math. Comput., 60(201), 1992, 189-220.

[48] M. Shashkov, Conservative Finite-difference Methods on general grids, CRC Press, New York, 1996.

[49] E. Süli, The accuracy of cell vertex finite volume methods on quadrilateral meshes, Math. Comp., 59(200), 1992, 359-382.

[50] A.A. Samarskii, R.D. Lazarov, V.L. Makarov, Difference Schemes for differential equations having generalized solutions, Vysshaya Shkola Publishers, Moscow (Russian), 1987.

[51] Z. Cai, J. Mandel, S. Mc Cormick, The finite volume element method for diffusion equations on general triangulations, SIAM J. Numer. Anal., 28(2), 1991, 392-402.

[52] R. Herbin, O. Labergerie, Finite volume schemes for elliptic and elliptic-hyperbolic problems on triangular meshes, Comp. Meth. Appl. Mech. Engin., 147, 1997, 85-103.

[53] Z. Cai, On the finite volume element method, Numer. Math., 58, 1990, 713-735.

[54] P.A. Forsyth, P.H. Sammon, Quadratic Convergence for Cell-Centered Grids, Appl.Num. Math., 4, 1998, 377-394.

[55] R.D. Lazarov, I.D. Mishev, P.S Vassilevski, Finite volume methods for convection-diffusion problems, SIAM J. Numer. Anal., 33, 1996, 31-55.

[56] R. Herbin, An error estimate for a finite volume scheme for a diffusion-convection problem on a triangular mesh, Num. Meth. P.D.E., 11, 1995, 165-173.

[57] I.D. Mishev, Finite volume methods on Voronoï meshes, Num. Meth. P.D.E., 14(2), 1998, 193-212.

[58] S.V. Patankar, Numerical Heat Transfer and Fluid Flow, Hemisphere Publishing Corporation, 1980.

[59] B.E. Launder, D.B. Spalding, The mathematical modelling of turbulent flows, Appl. Math. Mech, 53(6), 1972, 424-424.

[60] A.K. Runchal, D.B. Spalding, A.D. Gosman, W.M. Pun, M. Wolfshtein, Heat and mass transfer in recirculating flows, Int. J. Heat Mass Transf, 13(9), 1970, 1509-1510.

[61] S. Zou, X.F. Yuan, X. Yang, W. Yi, X. Xu, An integrated lattice Boltzmann and finite volume method for the simulation of viscoelastic fluid flows, J. Non-Newton. Fluid Mech, 211, 2014, 99-113.

[62] M.A. Alves, F.T. Pinho, P.J. Oliveira, The flow of viscoelastic fluids past a cylinder: finite-volume high-resolution methods, J. Non-Newton. Fluid Mech., 97, 2001, 207-232.

[63] N. Phan-Thien, S.C. Xue, R.I. Tanner, Numerical study of secondary flows of viscoelastic fluid in straight pipes by an implicit finite volume method, J. Non-Newton. Fluid Mech, 59, 1995, 191-213.

[64] M.S. Darwish, J.R. Whiteman, Numerical modelling of viscoelastic liquids using a finite-volume method, J. Non-Newton. Fluid Mech, 45, 1992, 311-337.

[65] J.A.M. Kuipers, E.A.J.F. Peters, S. De, S. Das, J.T. Padding, A coupled finite volume immersed boundary method for simulating 3d viscoelastic flows in complex geometries, J. Non-Newton. Fluid Mech, 232, 2016 67-76.

[66] B. Behdani, M. Senter, L. Mason, M. Leu, J. Park,Numerical Study on the Temperature-Dependent Viscosity Effect on the Strand Shape in Extrusion-Based Additive Manufacturing, J. manuf. mater, 4(2), 2020, 46.

[67] G. Raush, J. Rigola, S. Morales, C.D. Pérez-Segarra, Analysis of two-phase flow in double-pipe condensers and evaporators with special emphasis on transition zones: Numerical model and experimental comparison, International Refrigeration and Air Conditioning Conference, http://docs.lib.purdue.edu/iracc/658, 2004.

[68] Y. Ma, A. Shahsavar, I. Moradi, S. Rostami, A. Moradikazerouni, H. Yarmand, N. W. B. M. Zulkifli, Using finite volume method for simulating the natural

convective heat transfer of nano-fluid flow inside an inclined enclosure with conductive walls in the presence of a constant temperature heat source, Phys. A: Stat. Mech. Appl., 580, 2021, 123035.

[69] F. Mebarek-Oudina, R. Bessaïh, Numerical simulation of natural convection heat transfer of copper-water nanofluid in a vertical cylindrical annulus with heat sources, Thermophys. Aeromechanics, 26, 2019, 325-334.

[70] OpenFOAM, http://www.openfoam.org (accessed on 12 January 2019).

[71] H. Jasak, OpenFOAM: open source CFD in research and industry, Int. J. Nav. Archit. Ocean Eng, 1(2), 2009, 89-94.

[72] F. Pimenta, M.A. Alves, rheoTool, 2016, https://github.com/fppimenta/rheoTool (accessed on 8 February 2022).

[73] J.L. Favero, A.R. Secchi, N.S.M. Cardozo, H. Jasak, Viscoelastic flow analysis using the software OpenFOAM and differential constitutive equations, J. Non-Newton Fluid Mech., 165, 2010, 1625–1636.

[74] F. Habla, M.W. Tan, J. Haßlberger, O. Hinrichsen, Numerical simulation of the viscoelastic flow in a three-dimensional lid-driven cavity using the log-conformation reformulation in OpenFOAM, J. Non-Newton. Fluid Mech, 212, 2014, 47-62.

[75] J.L. Favero, A.R. Secchi, N.S.M. Cardozo, H. Jasak, Simulation of Free Surface Viscoelastic Fluid Flow Using the viscoelasticInterFoam Solver, Comput. Aided Chem. Eng., 28, 2010, 31-36.

[76] J.L. Favero, 2009, Viscoelastic flow simulation in openfoam: presentation of the viscoelasticfluidfoam solver Technical Report, Universidade Federal do Rio Grande do Sul-Department of Chemical Engineering http://powerlab.fsb.

hr/ped/kturbo/OpenFOAM/slides/viscoelasticFluidFoam.pdf(accessed on 8 February 2022).

[77] H.H. Najafabadi, M.K. Moraveji, CFD investigation of local properties of $Al_2O_3$/water nanofluid in a converging microchannel under imposed pressure difference, Adv. Powder Technol, 28(3), 2017, 63-774.

[78] A.J. Chamkha, G. Jomardiani, M.A. Ismael, R. Ghasemiasl, T. Armaghani, Thermal and entropy analysis in L-shaped non-Darcian porous cavity saturated with nanofluids using Buongiorno model: Comparative study, Math. Methods Appl. Sci, 2020.

[79] N. Hazeri-Mahmel, Y. Shekari, A. Tayebi, Three-dimensional analysis of forced convection of Newtonian and non-Newtonian nanofluids through a horizontal pipe using single- and two-phase models, Int. Commun. Heat Mass Transf., 121, 2021, 105119.

[80] X. Meng, X. Zhang, Q. Li, Numerical investigation of nanofluid natural convection coupling with nanoparticles sedimentation, Appl. Therm. Eng., 95(25), 2016, 411-420.

[81] M.G. Li, C. Zheng, Q. Zhao, X. Chen, W.T. Wu, Anisotropic heat transfer of ferro-nanofluid in partially heated rectangular enclosures under magnetic field, Case Stud. Therm. Eng., 26, 2021, 101145.

[82] C. Kunkelmann, P. Stephan, CFD simulation of boiling flows using the volume-of-fluid method within OpenFOAM, Numer. Heat Transf.; A: Appl., 56(8), 2009, 631-646.

[83] A. Ghione, Development and validation of a two-phase CFD model using OpenFOAM, Master of Science Thesis, Royal Institute of Technology, 2012.

[84] K. Fu, Implementation and validation of two-phase boiling flow models in openfoam, Technical report, KTH, August 2012.

[85] Q. Zeng, J. Cai, H. Yin, X. Yang, T. Watanabe, Numerical simulation of single bubble condensation in subcooled flow using OpenFOAM, Prog. Nucl. Energy, 83, 2015, 336-346.

[86] A. Mavi, T. Chinyoka, Finite volume computational analysis of the heat transfer characteristic in a double-cylinder counter-flow heat exchanger with viscoelastic fluids, Defects and Diffusion Forum., 2022, In Press.

[87] T. Chinyoka, O.D. Makinde, Viscoelastic modeling of the diffusion of polymeric pollutants injected into a pipe flow, Acta Mechanica Sinica, 29(2), 2013, 166-178.

[88] R. Nahme, Beitrage zur hydrodynamischenTheorie der Laggerreibung, Ing.-Arch., 11, 1940, 191-1940.

[89] K.J. Laidler, The development of the Arrhenuis equation, J. Chem. Educ., 4, 1984, 494-498.

[90] T. Chinyoka, Effects of Fluid Viscoelasticity in Non-Isothermal Flows. In: A. Ahsan (Editor); Evaporation, Condensation and Heat transfer, London: IntechOpen; 2011, https://www.intechopen.com/chapters/19424doi:10.5772/21299

[91] N. Phan-Thien, R.I. Tanner, A new constitutive equation derived from network theory, J. Non-Newton Fluid Mech., 2, 1977, 353-365.

[92] R. Fattal, R. Kupferman, Constitutive laws for the matrix-logarithm of the con-formation tensor, J. Non-Newtonian Fluid Mech., 123, 2004, 281–285.

[93] R. Fattal, R. Kupferman, Finite element methods for calculation of steafy viscoealstic flow using constitutive equation with a Newtonian viscosity, J. Non-Newtonian Fluid Mech., 36, 1990, 159-192.

[94] D. Rajagopalan , R.C. Armstrong, R.A. Brown, Constitutive laws for the matrix-logarithm of the con-formation tensor, J. Non-Newtonian Fluid Mech., 123, 2004, 281–285.

[95] M.A. Alves, P.J. Oliveira, F.T. Pinho, A convergent and universally bounded inter-polation scheme for the treatment of advection, Int. J. Numer. Meth. Fluids, 41, 2003, 47–75.

[96] A.R. Muniz, A.R. Secchi, N.S.M. Cardozo, High-order finite volume method for solving viscoelastic fluid lows, Braz. J. Chem. Eng., 25, 2008, 53–58.

[97] M.G.N. Perera, K. Walters, Long-range memory effects in flows involving abrupt changes in geometry, J. Non-Newtonian Fluid Mech., 2, 1977, 49–81.

[98] D. Rajagopalan, R.C. Armstrong, R.A. Brown, Finite element methods for calculation of steady, viscoelastic flow using constitutive equations with Newtownian viscosity, J. Non-Newtonian Fluid Mech., 36, 1990, 159–192.

[99] R. Guénette, M. Fortin, A new mixed finite element method for computing viscoelastic flows, J. Non-Newtonian Fluid Mech., 60, 1995, 27–52.

[100] J. Sun, N. Phan-Thien, R.I. Tanner, An adaptive viscoelastic stress splitting scheme and its applications: $AVSS/SIandAVSS/SUPG$, J. Non-Newtonian Fluid Mech., 65, 1996, 75–91.

[101] H.G. Weller, G. Tabor, H. Jasak, C. Fureby, A Tensorial Approach to Computational Continuum Mechanics Using Object Orientated Techniques, Comput. Phys., 12, 1998, 620-631.

[102] N. Afgan, M. Carvalho, A. Bar–Cohen, D. Butterworth, W. Roetzel, editors, Butterworth D. Developments in shell-and-tube heat exchangers. In New Developments in Heat Exchangers, Gordon and Breach, New York, 4, 1996, 437–47.

[103] E.A.D. Saunders, Heat Exchangers: Selection, Design and Construction, Wiley, New York, 1988.

[104] G. Walker, Industrial Heat Exchangers: A Basic Guide (2nd edn), Hemisphere Publishing, Washington, DC, 1990.

[105] T. Chinyoka, O.D. Makinde, On transient flow of a reactive variable viscosity third-grade fluid through a cylindrical pipe with convective cooling, Meccanica 47, 2012, 667–685.

[106] T. Chinyoka, O.D. Makinde, A.S. Eegunjobi, Numerical investigation of entropy generation in an unsteady flow through a porous pipe with suction, International Journal of Exergy, 12(3), 2013, 279-297.

[107] Z. Nyandeni, T. Chinyoka, Computational aeroacoustic modeling using hybrid Reynolds averaged Navier–Stokes/large-eddy simulations methods with modified acoustic analogies, International Journal for Numerical Methods in Fluids, 93, 2021, 2611-2636.

[108] A. Mavi, Computational analysis of viscoelastic fluid dynamics with applications to heat exchangers, Master's thesis, University of Cape Town, 2019.

[109] W. Roetzel, X. Luo, D. Chen, Dynamic analysis of heat exchangers and their networks, in: Design and Operation of Heat Exchangers and their Networks, Academic Press, Editor(s): W. Roetzel, X. Luo, D. Chen, 2020, 319-390.

[110] W. Roetzel, X. Luo, D. Chen, Optimal design of heat exchanger networks, in: Design and Operation of Heat Exchangers and their Networks, Academic Press, Editor(s): W. Roetzel, X. Luo, D. Chen, 2020, 231-317.

[111] W. Roetzel, X. Luo, D. Chen, Basic thermal design theory for heat exchangers, in: Design and Operation of Heat Exchangers and their Networks, Academic Press, Editor(s): W. Roetzel, X. Luo, D. Chen, 2020, 13-69.

[112] C. Balaji, Balaji Srinivasan, Sateesh Gedupudi, Heat exchangers, in: Heat Transfer Engineering, Academic Press, Editor(s): C. Balaji, Balaji Srinivasan, Sateesh Gedupudi, 2021, 199-231.

[113] S. Chand, M. Subhani, P. Sravani, The Systematic Comparision on Analysis of Parallel Flow and Counter Flow Heat Exchanger by using CFD and Practicle Methods, International Journal for Modern Trends in Science and Technology, 7, 2021, 153-161.

[114] M. Faizan, A. Almerbati, Evolutionary Design of Compact Counterflow Heat Exchanger, SSRN Electronic Journal, 2022, doi: 10.2139/ssrn.4085355

[115] S. Alaqel, N.S. Saleh, R. Saeed, E. Djajadiwinata, M. Sarfraz, A. Alswaiyd, H. Al-Ansary, O. Zeitoun, S. Danish, Z. Al-Suhaibani, A. El-Leathy, S. Jeter, A. Khayyat, Particle-to-fluid direct-contact counter-flow heat exchanger: Simple-models validation and integration with a particle-based central tower system, Case Studies in Thermal Engineering, 33, 2022, 101994.

[116] J.R. Clermont, A. Wachs, A. Khalifeh, Computations of nonisothermal viscous and viscoelastic flows in abrupt contractions using a finite volume method, Eng. Comput., 19, 2002, 874-901.

[117] R.I. Issa, Solution of the implicitly discretised fluid flow equations by operator-splitting, J Comp Phys, 62, 1986, 40-65.

[118] X. Chen, H. Marschall, M. Schäfer, and D. Bothe, A comparison of stabilisation approaches for finite-volume simulation of viscoelastic fluid flow, Int. J. Comput. Fluid Dyn., 27, 2013, 229–250.

[119] L.J. Amoreira, P.J. Oliveira, Comparison of Different Formulations for the Numerical Calculation of Unsteady Incompressible Viscoelastic Fluid Flow, adv. appl. math. mech., 27, 2010, 483–502.

[120] A. Mavi, T. Chinyoka, A. Gill, Modelling and Analysis of Viscoelastic and Nanofluid Effects on the Heat Transfer Characteristics in a Double-Pipe Counter-Flow Heat Exchanger, Applied Sciences, 12(11), 2022, 5475.

[121] J.A. Eastman, U.S. Choi, L.J. Thompson, S. Lee, Enhanced thermal conductivity through the development of nanofluids, Mater Res. Soc. Symp. Proc., 457, 1996, 3–11.

[122] M.S. Liu, M.C.C. Lin, I.T. Huang, C.C. Wang, Enhancement of thermal conductivity with CuO for nanofluids, Chem. Eng. Technol., 29, 2006, 72–77.

[123] Y. Hwang, H.S.K. Par, J.K. Lee, W.H. Jung, Thermal conductivity and lubrication characteristics of nanofluids, Curr. Appl. Phys., 6 (Suppl. 1), 2006, 67–71.

[124] W. Yu, H. Xie, L. Chen, Y. Li, Investigation of thermal conductivity and viscosity of ethylene glycol based ZnO nanofluid, Thermochim. Acta, 491, 2009, 92–96.

[125] H.A. Mintsa, G. Roy, C.T. Nguyen, D. Doucet, New temperature dependent thermal conductivity data for water-based nanofluids, Int. J. Therm. Sci., 48, 2009, 363–371.

[126] S.M.S. Murshed, K.C. Leong, C. Yang, Enhanced thermal conductivity of $TiO_2$–water based nanofluids, Int. J. Therm. Sci., 44, 2005, 367–373.

[127] H.E. Patel, S.K. Das, T. Sundararajan, A.S. Nair, B. George, T. Pradeep, Thermal conductivities of naked and monolayer protected metal nanoparticle based nanofluids: Manifestation of anomalous enhancement and chemical effects, Appl. Phys. Lett., 83, 2003, 2931–2933.

[128] Y. Xuan, Q. Li, Heat transfer enhancement of nanofluids, Int. J. Heat Fluid Flow, 21, 2000, 58-64.

[129] M.J. Assael, I.N. Metaxa, K. Kakosimos, D. Constantinou, Thermal Conductivity of Nanofluids—Experimental and Theoretical, Int. J. Thermophys., 27, 2006, 999-1017.

[130] J. Philip, J.M. Laskar, B. Raj, Magnetic field induced extinction of light in a suspension of $Fe_3O_4$ nanoparticles, Appl. Phys. Lett., 92, 2008, 221911.

[131] E. Abu-Nada, H.F. Oztop, Numerical analysis of $Al_2O_3$/Water nanofluids natural convection in a wavy walled cavity, Numer. Heat Transf. A Appl., 59, 2011, 403-419.

[132] A. Yurddaş, Y. Çerçi, Numerical analysis of heat transfer in a flat-plate solar collector with nanofluids, Heat Transf. Res., 48, 2017, 681-714.

[133] A. Kamyar, R. Saidur, M. Hasanuzzaman, Application of Computational Fluid Dynamics (CFD) for nanofluids, Int. J. Heat Mass Transf., 55, 2012, 4104–4115.

[134] M.K. Moraveji, M. Darabi, S.M.H. Haddad, R. Davarnejad, Modeling of convective heat transfer of a nanofluid in the developing region of tube flow with computational fluid dynamics, Int. Commun. Heat Mass Transf., 38, 2011, 1291–1295.

[135] Y. Hwang, J.K. Lee, C.H. Lee, Y.M. Jung, S.I. Cheong, C.G. Lee, B.C. Ku, S.P. Jang, Stability and thermal conductivity characteristics of nanofluids, Thermochim. Acta, 455, 2007, 70–74.

[136] P. Sharma, I. Baek, T. Cho, S. Park, K. Bong, Enhancement of thermal conductivity of ethylene glycol based silver nanofluids, Powder Technol., 208, 2011, 7–19.

[137] S.K. Das, N. Putra, P. Thiesen, W. Roetzel, Temperature dependence of thermal conductivity enhancement for nanofluids, J. Heat Transf., ASME, 125, 2015, 567–574.

[138] S. Özerinç, S. Kalaç, A.G. Yazicioğlu, Enhanced thermal conductivity of nanofluids: A state-of-the-art review, Microfluid. Nanofluid., 8, 2010, 145-170.

[139] V.I. Terekhov, S.V. Kalinina, V.V. Lemanov, The mechanism of heat transfer in nanofluids: State of the art (review), Part 1, Synthesis and properties of nanofluids, Thermophys. Aeromech., 17, 2010, 1-14.

[140] P. Keblinski, S.R. Phillpot, S.U. Choi, J.A. Eastman, Mechanisms of heat flow in suspensions of nano-sized particles (nanofluids), Int. J. Heat Mass Transf., 45, 2002, 855-863.

[141] A.A. Mahyari, A. Karimipour, M. Afrand, Effects of dispersed added graphene oxide-silicon carbide nanoparticles to present a statistical formulation for the mixture thermal properties, Phys. A Stat. Mech. Appl., 521, 2019, 98-112.

[142] C. Pang, J.Y. Jung, Y.T. Kang, Aggregation based model for heat conduction mechanism in nanofluids, Int. J. Heat Mass Transf., 72, 2014, 392–399.

[143] S. Lee, S.U.S. Choi, S. Li, J.A. Eastman, Measuring thermal conductivity of fluids containing oxide nanoparticles, J. Heat Transf., 121, 1999, 280-289.

[144] X. Wang, X. Xu, S.U.S. Choi, Thermal conductivity of nanoparticle-fluid mixture, J. Thermophys. Heat Transf., 13, 1999, 474-480.

[145] H. Masuda, A. Ebata, K. Teramea, N. Hishinuma, Alteration of thermal conductivity and viscosity of liquid by dispersing ultra-fine particles, Netsu Bussei, 4, 1993, 227–233.

[146] A. Grimm, Powdered Aluminum-Containing Heat Transfer Fluids, German Patent DE 4131516A1, 8 April 1993.

[147] J.A. Eastman, S.U.S. Choi, S. Li, W. Yu, L.J. Thompson, Anomalously Increased Effective Thermal Conductivities Containing Copper Nanoparticles, Appl. Phys. Lett., 78, 2001, 718-720.

[148] Y. Ding, H. Alias, D. Wen, R.A. Williams, Heat transfer of aqueous suspensions of carbon nanotubes (CNT nanofluids), Int. J. Heat Mass Transf., 49, 2006, 240.

[149] S.Z. Heris, M.N. Esfahany, S.G. Etemad, Experimental investigation of convective heat transfer of $Al_2O_3$/water nanofluid in circular tube, Int. J. Heat Fluid Flow, 28, 2007, 203-210.

[150] Y. Xuan, Q. Li, Investigation on Convective Heat Transfer and Flow Features of Nanofluids, J. Heat Transf., 1, 2003, 151-155.

[151] Q. Li, Y. Xuan, Convective Heat Transfer and Flow Characteristics of Cu-Water Nanofluid, Sci. China (Ser. E), 45, 2002, 408–16.

[152] I. Khan, T. Chinyoka, A. Gill, Computational Analysis of the Dynamics of Generalized-Viscoelastic-Fluid-Based Nanofluids Subject to Exothermic-Reaction in Shear-Flow, Journal of Nanofluids, 11(4), 2022, 487–499.

[153] I. Khan, T. Chinyoka, A. Gill, Dynamics of Non-Isothermal Pressure-Driven Flow of Generalized Viscoelastic-Fluid-Based Nanofluids in a Channel, Mathematical Problems in Engineering, vol. 2022, Article ID 9080009, 2022, 17-pages.

[154] B. Kristiawan, A.I. Rifái, K. Enoki, A.T. Wijayanta, T. Miyazaki, Enhancing the thermal performance of TiO2/water nanofluids flowing in a helical microfin tube, Powder Technol., 376, 2020, 254-262.

[155] S. Kondaraju, E.K. Jin, J.S. Lee, Investigation of heat transfer in turbulent nanofluids using direct numerical simulation, Phys. Rev. E, 81, 2010, 016304.

[156] M. Kalteh, A. Abbassi, M. Saffar-Avval, J. Harting, Eulerian–Eulerian two-phase numerical simulation of nanofluid laminar forced convection in a microchannel, Int. J. Heat Fluid Flow, 32, 2010, 107-116.

[157] Pranowo, D.A. Makarim, A. Suami, A.T. Wijayanta, N. Kobayashi, Y. Itaya, Marangoni convection within thermosolute and absorptive aqueous LiBr solution, Int. J. Heat Mass Transf., 188, 2022, 122621.

[158] R.L. Hamilton, O.K. Crosser, Thermal conductivity of heterogeneous two-component systems. Ind. Eng. Chem., 1, 1962, 187-191.

[159] A. Mavi, T. Chinyoka, Volume-of-fluid based finite-volume computational simulations of three-phase nanoparticle-liquid-gas boiling flow problems in vertical rectangular channels, Energies, 15(15), 2022, 5746.

[160] Z. Yang, X.F. Peng, P. Ye, Numerical and experimental investigation of two phase flow during boiling in a coiled tube, Int J Heat Mass Transfer, 51(5–6), 2008, 1003–16.

[161] A. Mukherjee, S.G. Kandlikar, Numerical simulation of growth of a vapor bubble during flow boiling of water in a microchannel, Microfluid Nanofluid, 1, 2005, 137–45.

[162] M. Nabil, A.S. Rattner, interThermalPhaseChangeFoam—A framework for two-phase flow simulations with thermally driven phase change, Soft-wareX, 5, 2016, 216-226.

[163] J.M. Wilms, T.M. Harms, On the development of an OpenFOAM solver to model two-phase horizontal flow in a heated pipe, 2014.

[164] B. Koncar, E. Krepper, CFD simulation of convective flow boiling of refrigerant in a vertical annulus, Nucl Eng Des, 238, 2008, 693–706.

[165] A.A. Mostafa, H.C.Mongia, On the modeling of turbulent evaporating sprays: eulerian versus lagrangian approach, Int J Heat Mass Transfer, 30(12), 1987, 2583–93.

[166] D.I. Kolaitis, M.A. Founti, A comparative study of numerical models for Eulerian–Lagrangian simulations of turbulent evaporating sprays, Int J Heat Fluid Flow, 27(3), 2006, 424–35.

[167] M. Mei, B. Yu, M. Zou, L. Luo, A numerical study on growth mechanism of dropwise condensation, Int J Heat Mass Transfer, 54(9-10), 2011, 2004-2013.

[168] C.W. Hirt, B.D. Nichols, Volume of fluid (VOF) method for the dynamics of free boundary, J. Comput. Phys., 39(1), 1981, 201-225.

[169] S.W. Welch, J. Wilson, A volume of fluid based method for fluid flows with phase change, J. Comput. Phys., 160, 2000, 662-682.

[170] M.W. Akhtar, S.J. Kleis, Boiling flow simulations on adaptive octree grids, Int. J. Multiph. Flow, 53, 2013, 88-99.

[171] C. Kunkelmann, P. Stephan, Numerical simulation of the transient heat transfer during nucleate boiling of refrigerant HFE-7100, Int J Refrig, 33, 2010, 1221-1228.

[172] N. Samkhaniani, M. Ansari, A VOF Method to Phase Change Modeling, gas, 16(2), 2002, 2.

[173] B. Shu, F. Dammel, P. Stephan, Phase change model for two-phase fluid flow based on the volume of fluid method, Proceedings of CHT-08 ICHMT International Symposium on Advances in Computational Heat Transfer, Begel House Inc., 2008.

[174] M. Bahreini, A. Ramiar, A.A. Ranjbar, Boiling flow simulations on adaptive octree grids, Int. J. Heat Mass Transf., 2, 2016, 131-143.

[175] T. Chinyoka, Y.Y. Renardy, M. Renardy, D.B. Khismatullin, Two-dimensional study of drop deformation under simple shear for Oldroyd-B liquids, Journal of Non-Newtonian Fluid Mechanics, 130(1), 2005, 45-56.

[176] R.W. Schrage, A Theoretical Study of Interphase Mass Transfer, Columbia University Press, New York, 1953.

[177] I. Tanasawa, Advances in condensation heat transfer, J.P. Hartnett, T.F. Irvine (Eds.), Advances in Heat Transfer, Academic Press, San Diego, 1991.

[178] W.H. Lee, A pressure iteration scheme for two-phase flow modeling, T.N. Veziroglu (Ed.), Multiphase Transport Fundamentals, Reactor Safety, Applications, Hemisphere Publishing, Washington, DC, 1980.

[179] F.R. Menter, T. Esch, Elements of Industrial Heat Transfer Prediction, 16th Brazilian Congress of Mechanical Engineering, November 2001.

[180] F.R. Menter, M. Kuntz, R. Langtry, Ten Years of Industrial Experience with the SST Turbulence Model, Proceedings of the 4th International Symposium on Turbulence, Heat and Mass Transfer, Begell House Inc., West Redding, 2003, 625-632.

[181] D. Sun, J. Xu, Q. Chen, Modeling of the evaporation and condensation phase–change problems with FLUENT, Numer. Heat Transfer, Part B, 66, 2014, 326-342.

[182] I. Ohnaka, Introduction to Computer Analysis of Heat Transfer and Solidification, Maruzen, Tokyo, 1985.

[183] S.C.K. De Schepper, G.J. Heynderichx, G.B. Marin, Modeling the evaporation of a hydrocarbon feedstock in the convection section of a steam cracker, Comp. Chem. Eng., 33, 2009, 122-132.

[184] D.L. Sun, J.L. Xu, L. Wang, Development of a vapor–liquid phase change model for volume-of-fluid method in FLUENT, Int. Commun. Heat Mass Transf., 39, 2012, 1101–1106.

[185] M. Bahreini, A. Ramiar, A.A. Ranjbar, Numerical simulation of bubble behavior in subcooled flow boiling under velocity and temperature gradient, Nucl. Eng. Des., 293, 2015, 238-248.

[186] J.H. Son, S. Park, Numerical Simulation of Phase–change Heat Transfer Problems Using Heat Fluxes on Phase Interface Reconstructed by Contour-Based Reconstruction Algorithm, Int. J. Heat Mass Transf, 156, 2015, 119894.

[187] S.A. Hosseini, R. Kouhikamali, A numerical investigation of various phase change models on simulation of saturated film boiling heat transfer, Heat Transfer—Asian Research, 48(6), 2019, 2577-2595.

[188] B.D.N. Hirt, W. Cyril, Volume of fluid (VOF) method for the dynamics of free boundaries, Iran. J. Sci. Technol., 42(3), 2018, 357–366.

[189] I. Khan, T. Chinyoka, A. Gill, Computational Analysis of Shear Banding in Simple Shear Flow of Viscoelastic Fluid-Based Nanofluids Subject to Exothermic Reactions, Energies, 15(5), 2022, 1719.

[190] I. Khan, T. Chinyoka, A. Gill, Computational-analysis of the non-isothermal dynamics of gravity-driven flows of viscoelastic-fluid-based nanofluids down an inclined plane, FDMP-Fluid Dynamics & Materials Processing, In press, 2022.

[191] J.U. Brackbill, D.B. Kothe, C. Zemach, A Continuum Method for Modeling Surface Tension, Journal of Computational Physics, Vol. 100, 1992, 335-354.

[192] A. Alizadehdakhel, M. Rahimi, A.A. Alsairafi, CFD modeling of flow and heat transfer in a thermosyphon, Int. Commun. Heat Mass Transf., 37, 2010, 312-318.

[193] C. Fang, M. David, A. Rogacs, K. Goodson, Volume of fluid simulation of boiling two-phase flow in a vapor-venting microchannel, Front Heat Mass Transf, 1, 2010, 1-11.

[194] K. Aljundi, WeBBusterZ Engineering Software, https://www.webbusterz.org/classification-of-heat-exchangers/ (accessed on 9 May 2022).